The Influence of Alloying and Temperature on the Stacking-fault Energy of Iron-based Alloys

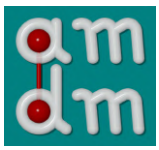

Hojjat Gholizadeh

Chair of Atomistic Modelling and Design on Materials

Montanuniversität Leoben

A thesis submitted for the degree of

PhilosophiæDoctor (PhD) in Solid State Physics

2013 March

1. Reviewer: Name

2. Reviewer:

Day of the defense:

Signature from head of PhD committee:

Abstract

To ...

Acknowledgements

Contents

List of Figures

LIST OF FIGURES

List of Tables

Glossary

DAPI 4',6-diamidino-2-phenylindole; a fluorescent stain that binds strongly to DNA and serves to marks the nucleus in fluorescence microscopy

DEPC diethyl-pyro-carbonate; used to remove RNA-degrading enzymes (RNAases) from water and laboratory utensils

DMSO dimethyl sulfoxide; organic solvent, readily passes through skin, cryoprotectant in cell culture

EDTA Ethylene-diamine-tetraacetic acid; a chelating (two-pronged) molecule used to sequester most divalent (or trivalent) metal ions, such as calcium (Ca^{2+}) and magnesium (Mg^{2+}), copper (Cu^{2+}), or iron (Fe^{2+} / Fe^{3+})

1

Introduction

The aim of this chapter is defining the required terms, introducing the topic and its importance, and explaining the motivations for this study. We start by explaining the geometry of close-packed lattices and then introduce a variety of faults and defects related to it. Later, a connection between these faults and plasticity of materials is explained, which shows the importance of the topic. The motivation of the work is also explained at the end.

1.1 Close-packed Stacking

In geometry, close-packing of equal spheres is a dense arrangement of congruent spheres in an infinite and regular lattice. The term can be used in crystallography by using the hard spherical ball representation for atoms, and considering the same radius for them. A close-packed structure is then constructed by stacking the close-packed atomic layers on top of one another. The close-packed layers in the stack define atomic positions which can be labeled by A, B and C (see Fig. 1.1(a)). Atomic positions which lie within the same layer have the same label. Labeling the atomic layers finds a meaning only when their stacking orders is considered. Although, in general, atomic positions of different labels may feel different environments, we will notice two structures where all atomic positions, disregarding their labels, are exactly equal.

The close-packing criteria requires that no two layers of the same label, such as AA, are stacked in juxtaposition to one another. This restriction, places the atomic spheres on the vertices of regular tetrahedrons, whose sides equal the interatomic distance a (see Fig. 1.1(b)). The distance between two consecutive atomic layers, the single-layer thickness, equals the height of the mentioned tetrahedron and found as $d = a\sqrt{2/3}$. Since every tetrahedron contains only 1/3 of an atom, the lattice volume per atom equals $V_{\text{p.atom}} = 3V_{\text{tetrahedron}} = \frac{\sqrt{2}}{4}a^3$. The packing fraction, the fraction of space occupied by atomic spheres, is calculated by dividing the actual volume of a sphere of diameter a, *i.e.*, $V_0 = \frac{4\pi}{3}(a/2)^3$, by the lattice volume per atom $V_{\text{p.atom}}$. It is quite straightforward to show that any stacking sequence where consecutive layers are of different labels forms a close-packed structure with packing fraction of $\pi/\sqrt{18} \approx$

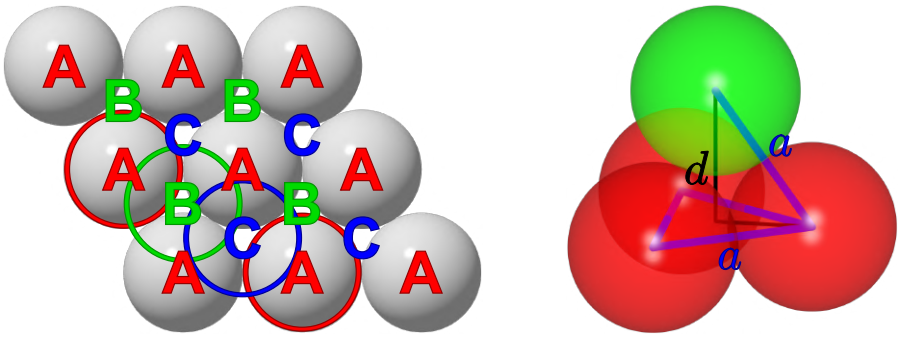

(a) (b)

Figure 1.1: (a) Top view of a close-packed layer where different stacking positions have been highlighted. Considering the given layer as A, atoms in the second layer would occupy either B or C positions. (b) The geometry of the stacking positions in a close-packed structure presented as a regular tetrahedron of sides a.

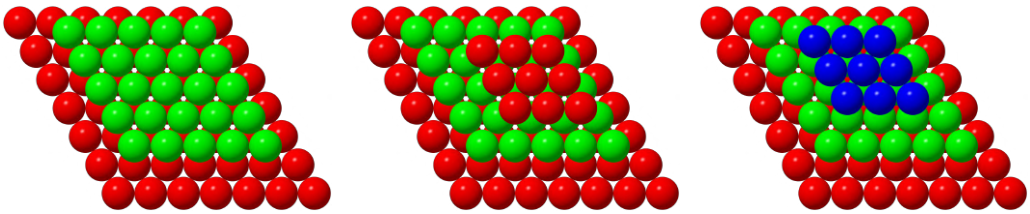

(a) (b) (c)

Figure 1.2: (a) Top view of a two-layer close-packed structure, where the first and the second layers occupy A and B positions, respectively; (b) Given two-layer stacking as AB, the third layer can occupy the same stacking positions as of the first layer, leading to an hcp structure with $ABABAB$ sequence. (c) Here the third layer occupies C positions. If the forth layer occupy the same stacking positions as of the first layer, the result would be an fcc structure with $\cdots ABCABC \cdots$ sequence.

0.74048, which is the maximum for a lattice of equal atoms.

Given a layer A, a hexagonal close-packed (hcp) structure is generated by stacking the atomic layers in $\cdots ABABAB \cdots$ (or equally $\cdots ACACAC \cdots$) order, where every second layer has the same label (see Figs. 1.2(a) and 1.2(b)). In an infinite hcp structure, all atomic positions are surrounded by the same environment; hence they are exactly equal. The periodicity of this structure along the stacking direction equals two atomic layers. The primitive cell of this structure is found as a rhombus-based prism of base sides a and hight c, where $c = 2d = a\sqrt{8/3}$, $\alpha = \beta = 90°$, and $\gamma = 120°$ (see Fig. 1.3). With volume of $a^3/\sqrt{2}$, the cell contains two atoms. The conventional unit cell, however, is a hexagonal-based prism which is simply three times as big as the primitive cell. According to the primitive lattice vectors, the close-packed layers lie within the {001} planes (or {0001}, using four-index scheme). In this lattice, both

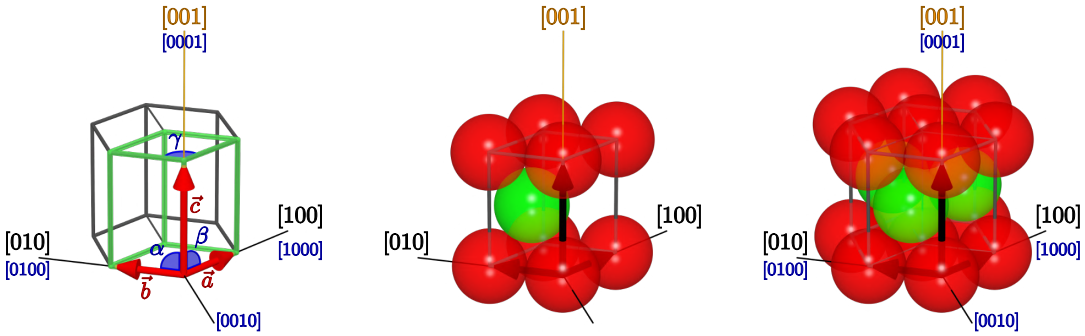

(a) (b) (c)

Figure 1.3: (a) Comparison of the conventional hexagonal cell (gray cage) and the primitive cell (highlighted by green color) of the hcp structure. In order to make permutation symmetries apparent, the Miller indices for this lattice are usually presented in $[hkil]$ scheme, where $i = -(h+k)$ (highlighted by blue color). (b) Atomic positions in the primitive cell colored regarding to their stacking positions. (c) Atomic positions in the conventional cell.

primitive and conventional cells have the same set of lattice vectors, where the stacking direction is indicated by [001] ([0001]).

The face-centered cubic (fcc) structure is, however, determined by $\cdots ABCABC \cdots$ sequence, which may equally be represented by $\cdots ACBACB \cdots$, where every third layer has the same label (see Fig. 1.2(c)). Although the periodicity of this structure along the stacking direction equals three atomic layers, by choosing a tilted axis for the third lattice vector, $\vec{c}$, it is possible to find a primitive cell so that its height would be equal to only one atomic layer (see Figs. 1.4(a) and 1.4(b)). This unit cell is a rhombohedron of sides a, angles $\alpha = \beta = \gamma = 60°$, and volume $a^3/\sqrt{8}$ which contains only one atom. The symmetry of the structure allows us to comprise the same unit cell using a different set of lattice vectors, where all three lattice vectors are equal along the stacking direction (see Figs. 1.4(c)). The conventional unit cell is a cube of sides $a_c = a\sqrt{2}$, where a is the side of the primitive cell and equals to the interatomic distance (see Figs. 1.4(d) and 1.4(e)). It is four times as big as the primitive cell and hence contains four atoms. Using the lattice vectors of the cubic cell, the close-packed layers and the stacking direction are defined by {111} and [111] indices, respectively.

When studying the {111} planes, the two mentioned cells for the fcc structure may not be the best possible choices. In such a case, a cell whose vectors are either parallel or normal to the plane is usually more favored. One possible cell with this feature is a rhombus-based prism, similar to the primitive cell of the hcp structure, whose base sides and height are a and $c = a\sqrt{6}$, respectively (see Figs. 1.4(g) and 1.4(h)). The cell is extended along the [111] direction up to three atomic layers, and hence it contains three atoms.

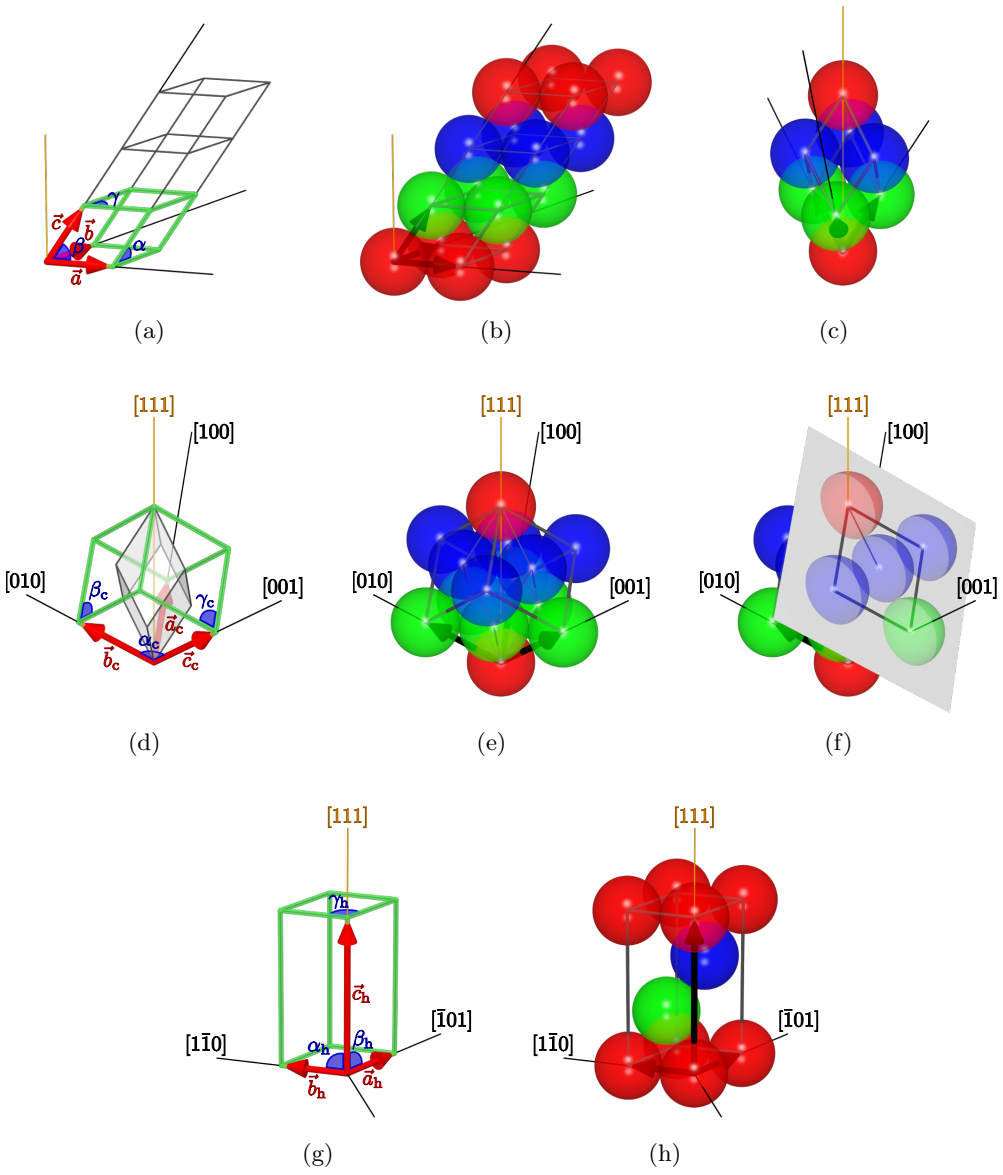

Figure 1.4: (a) The primitive cell of the fcc structure. (b) Atomic positions in the primitive cell. (c) The primitive cell is chosen so that all lattice vectors are equal along the stacking direction. (d) The conventional cubic cell of the fcc structure (highlighted by green) compared to the primitive cell (transparent rhombohedron). (e) Atomic positions in the cubic cell. The cell contains four atoms. (f) For better imagination of atomic positions in the cubic cell, the {001} plane of the cell has been highlighted. (g) Yet another unit cell for the fcc structure with emphasize on the stacking in the [111] direction. Note that the directions shown in this picture are based on the lattice vectors of the cubic cell. (h) Atomic positions in the hexagonal cell.

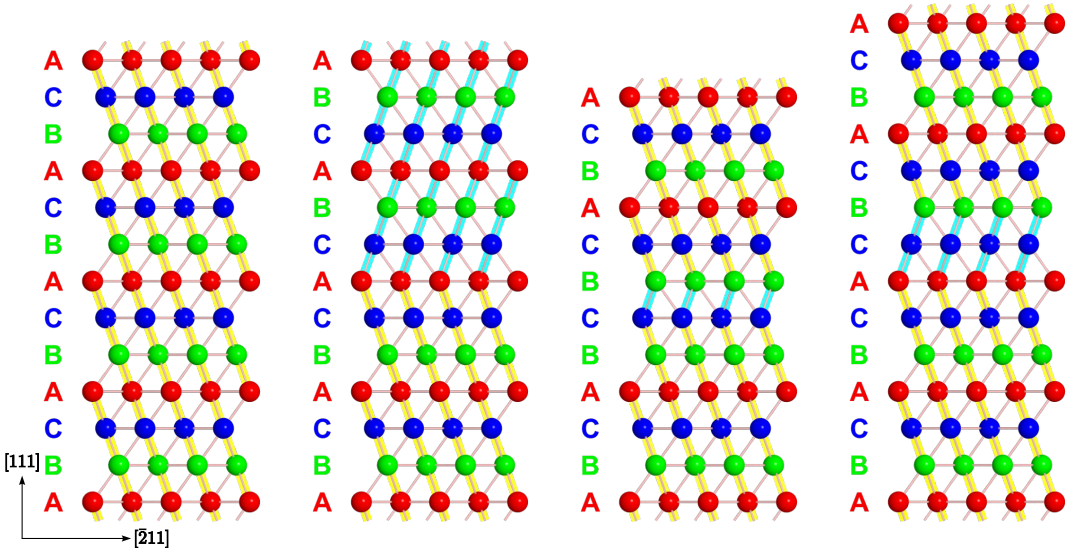

Figure 1.5: (a) The view of a perfect fcc structure when looking along the $[0\bar{1}1]$ direction. The stacking sequence for the perfect structure has been highlighted by yellow. (b) Twinning appears when the stacking order along the [111] direction is reversed. The reversed sequence has been highlighted by turquoise. (c) An *intrinsic* SF is generated by *removing* one atomic layer from the perfect sequence. (d) An *extrinsic* SF which is generated by *inserting* one atomic layer into the perfect sequence.

1.2 Geometry of the Stacking Faults in fcc Crystals

A stacking fault (SF) represents an interruption in the perfect stacking sequence of the close-packed layers. The exact explanation of lattice faults is dependent on the crystal structure. Here we discus a variety of faults in a lattice with the fcc structure.

Using the lattice vectors of the cubic cell of the fcc structure, the stacking direction is indicated by [111], and consequently, the close-packed layers lie within the {111} planes. These planes are also the *glide planes* and the coherent *twin planes*. A twinning might be considered as 180° rotation of one crystal half in the {111} plane, or equivalently, as a mirror plane reflection about the {111} plane (see Fig. 1.5(b)). Therefore, it would change the stacking of the close-packed layers to

$$\cdots ABCABC\overset{\dagger}{\underset{\ddagger}{A}}CBACBA\cdots, \tag{1.1}$$

where daggers denote the twin plane and also the center of the fault.

In the fcc structure, stacking faults are classified as *intrinsic* or *extrinsic*. Geometrically, an intrinsic stacking fault (ISF) simply corresponds to removing a layer from the perfect sequence (see Fig. 1.5(c)). However, the normal sequence remains unchanged on either sides of the faults right up to the fault plane. The corresponding stacking

sequence can be expressed as

$$\cdots ABCABC\,|\,BCABC\cdots, \tag{1.2}$$

where the vertical lines denote the center of the fault. On the other hand, the geometry of the extrinsic stacking fault (ESF) corresponds to inserting one additional layer into the perfect sequence (see Fig. 1.5(d)). It would generate a stacking sequence in the form of

$$\cdots ABCABC\,\|\,BABCABC\cdots, \tag{1.3}$$

where the vertical double-lines show the inserted layer.

One may consider other faults, containing two consecutive layers of the same label, like

$$\cdots ABCABC\,|\,CABCABC\cdots. \tag{1.4}$$

Such a configuration can simply be generated by removing two consecutive layers from the perfect sequence, *i.e.*, AB here. The configuration breaks the close packing at the place of the fault, so it is not energetically favored. To preserve the close packing, the fault can always be converted to the ESF by deforming one of the layers in the vicinity of the fault to another type, like

$$\cdots ABCABC\,|\,\underset{\downarrow}{C}ABCABC\cdots \;\Longrightarrow\; \cdots ABCABC\,\|\,BABCABC\cdots \qquad B \tag{1.5}$$

or

$$\cdots ABCABC\,|\,CABCABC\cdots \;\Longrightarrow\; \cdots ABCAB\,\|\,ACABCABC\cdots \qquad \underset{\downarrow}{A} \tag{1.6}$$

A SF can also be generated by a shearing operation on the {111} planes. This explanation is more close to nature, where the stacking faults are mainly produced in materials due to shear stresses. Focusing on one of the {111} planes in an fcc structure, an ISF can be produced by displacing all the layers above the plane by the lattice vector $\frac{1}{3}[\bar{2}11]$. Such a displacement causes the transitions $A \to B$, $B \to C$ and $C \to A$ for all layers above the mentioned plane (see Fig. 1.6(a)). This process is expressed as

$$\cdots ABCABC\underset{BCABCA}{\underset{\downarrow\downarrow\downarrow\downarrow\downarrow\downarrow}{ABCABC}}\cdots \;\Longrightarrow\; \cdots ABCABC\,|\,BCABCA\cdots. \tag{1.7}$$

Once more applying the same shearing operation on this structure would produce an ESF:

$$\cdots ABCABC\,|\,\underset{ABCABC}{\underset{\downarrow\downarrow\downarrow\downarrow\downarrow\downarrow}{BCABCAB}}\cdots \;\Longrightarrow\; \cdots ABCABC\,\|\,BABCABC\cdots. \tag{1.8}$$

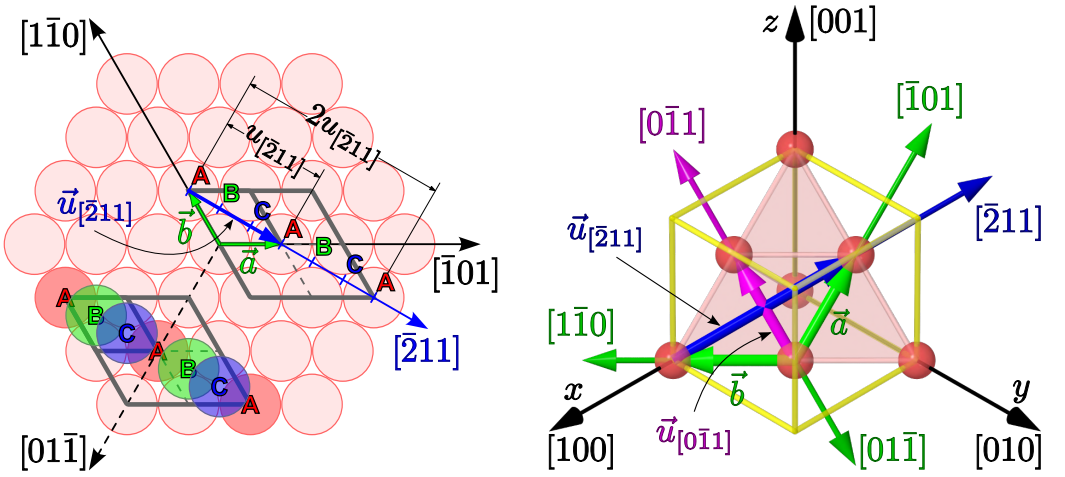

(a) (b)

Figure 1.6: (a) Projection of the atomic layers of types A, B, and C, and the displacement direction, $[\bar{2}11]$, for the $A \to B$, $B \to C$, and $C \to A$ transitions within the $\{111\}$ plane. The smaller rhombus depicts the base of the hexagonal unit cell of the fcc structure, while the larger rhombus shows the base of a 2×2 cell. (b) Definition of lattice and displacement vectors lying in the $\{111\}$ plane using the conventional unit cell.

For further convenience, the parameter u is defined as the displacement along the $[\bar{2}11]$ direction. The periodicity of the lattice along the $[\bar{2}11]$ direction is defined as the shortest non-zero displacement which leaves the structure unchanged. Here, this displacement is denoted by $u_{[\bar{2}11]}$. The required displacements corresponding to the transitions $A \to B$ and $A \to C$ are $u = \frac{1}{3}u_{[\bar{2}11]}$ and $u = \frac{2}{3}u_{[\bar{2}11]}$, respectively (see Fig. 1.6).

1.3 Stacking-Fault Energy

A SF rearranges the close-packed layers in a lattice and, thus, changes the total energy of the crystal. This energy change is defined as the stacking-fault energy (SFE), which is a material property on a very small scale, and usually denoted by γ_{SFE} (or γ_{ISFE}, to avoid confusion with the extrinsic stacking-fault energy) in units of milli-Joules per square meter ($\mathrm{mJ/m^2}$).

While the SFE corresponds to a displacement of $u = \frac{1}{3}u_{[\bar{2}11]}$, the generalized stacking-fault energy (GSFE), often called the γ-curve, is defined as a function expressing the energy dependence of the crystal on all variant displacements along the $[\bar{2}11]$ direction. A typical γ-curve is presented in Fig. 1.7. The SFE is the value of the γ-curve at $u = \frac{1}{3}u_{[\bar{2}11]}$, and is a local minimum for materials with stable fcc phase. In the figure, γ_{u} denotes the barrier which must be overcome to create the ISF. γ_{max} corresponds to a transition of $A \to C$, where two consecutive layers of the same type stack on top of each others. Thus, the curve shows a high maximum here.

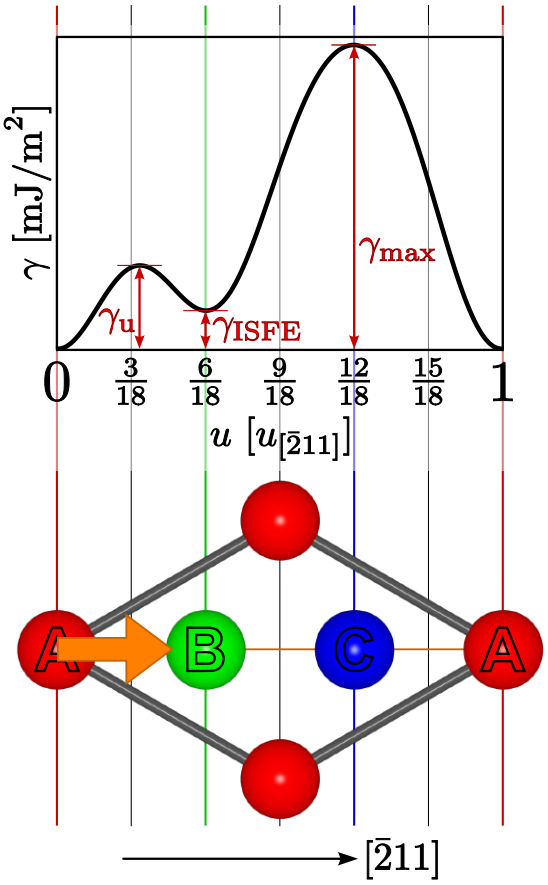

Figure 1.7: A typical γ-curve, corresponding to variant displacements along the $[\bar{2}11]$ direction in an fcc structure. For every point on the curve, the corresponding displacements can be found in the depicted unit cell at the bottom of the figure.

The γ-surface is even more general, and expresses the energy dependence of the crystal on all possible displacements within the $\{111\}$ plane, disregarding their directions. It is a function of two variables, $f(x, y)$, spanning the entire $\{111\}$ plane.

The SFE influences the preference of mechanisms through which the plastic deformation occurs in fcc metals. In order to explain it, we first discuss shortly about dislocations in fcc crystals. Dislocations are linear defects around which some of the atoms of the crystal lattice are misaligned. The direction of a dislocation is defined by *dislocation line*, whose unit vector is usually denoted by $\hat{t}$. There are two primary (basic) types of dislocations: *edge dislocation* and *screw dislocation*. For these primary dislocations, the dislocation line is a straight line resulting to a constant dislocation vector $\hat{t}$. However, in more general cases, *i.e.*, common mixed dislocations combining aspects of both types, the dislocation vector may vary with position: $\hat{t} = \hat{t}(\vec{r})$. For an infinite lattice with a single dislocation of primary types, moving along the dislocation line preserves the same surrounding environment. In the core on any dislocation,

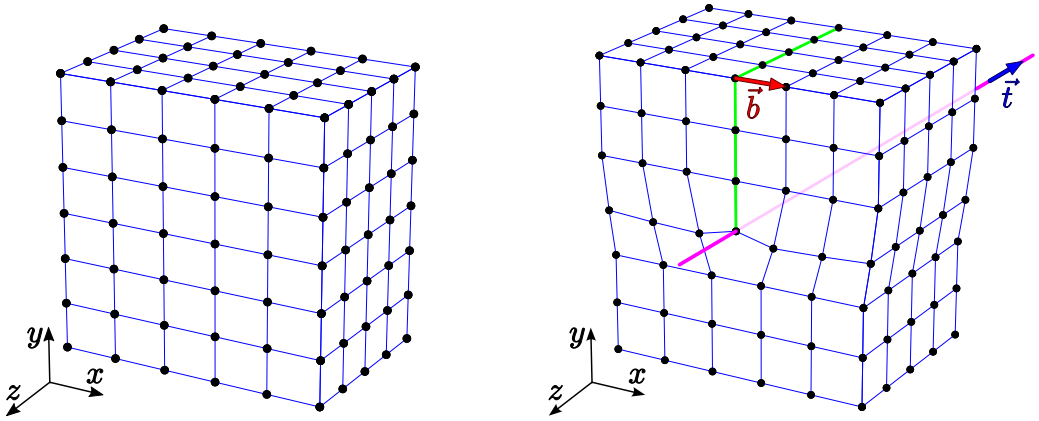

(a) (b)

Figure 1.8: (a) A perfect crystal lattice with a simple cubic unit cell. (b) Rearrangement of atomic positions around an edge dislocation, where the inserted extra layer has been highlighted by green.

atomic bonds are not in an equilibrium configuration, and thus the crystal energy and entropy change by introducing such defects.

The edge dislocation can simply be considered as termination of one atomic plane in the middle of crystal. Obviously, it can also be considered as insertion of an extra half-layer between other atomic layers. A schematic edge dislocation is presented in Fig. 1.8(b), where the inserted half-layer has been highlighted by green. The surrounding planes do not remain straight, but instead, bend around the edge in order to fill the newly created vacancies, resulting in reordering the crystal structure in either sides. Here, the dislocation line passes atomic position at the edge of the terminated layer (pink line in the figure). Compared to a perfect crystal (Fig. 1.8(a)), the crystal lattice is distorted around the dislocation line. The direction and the magnitude of this distortion is denoted by Burgers vector, $\vec{b}$, which is necessarily a lattice vector for *perfect* dislocations. Since magnitude of Burgers vector, b, is a measure for the *strength* of the dislocation, or the amount of elastic deformation in the core of the dislocation, $\vec{b}$ is usually the shortest translation vector of the lattice. For an edge dislocation, the Burgers vector is always perpendicular to the dislocation line (see Fig. 1.8(b)).

As already mentioned, dislocations change the crystal energy, which is usually expressed as the energy change per length of dislocation, $E = \frac{U}{L}$. This energy change is sum of two parts, *i.e.*, the elastic and the non-elastic parts. The elastic energy is due to the elastically strained bonds at further distances with respect to the dislocation line. The non-elastic energy is the result of distorted atomic bounds close to the dislocation line, where the elasticity theory can not be applied. The dependence of E on the magnitude of Burgers vector may be with a reasonable approximation expresses as

$$E = \alpha b^2 \tag{1.9}$$

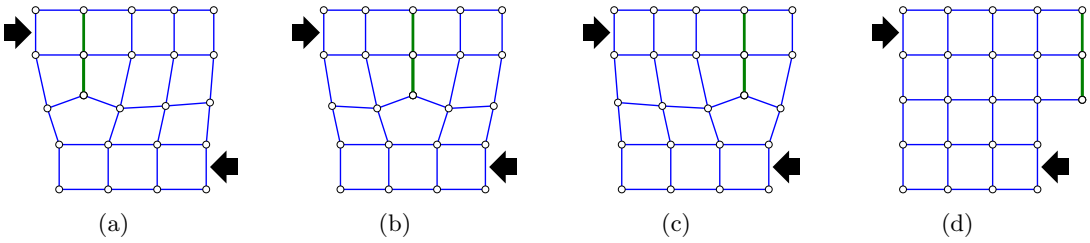

Figure 1.9: Slip movement of an edge dislocation in a simple cubic lattice.

where α is almost constant with respect to b and is a property of crystal. This equation shows that dislocations would energetically prefer to have the shortest possible Burgers vectors. That is why there are no dislocations with Burgers vectors larger than the smallest crystal translation vector; a dislocation with larger Burgers vector simply splits to two or more dislocations with shorter Burgers vectors.

Dislocations can slip in planes containing both the dislocation and the Burgers vectors. Such a plane is called *slip plane* or *glide plane*. For an edge dislocation, the dislocation and the Burgers vectors are perpendicular, so there is only one plane in which the dislocation can slip. In every step of a dislocation slip, around the dislocation line, atomic bounds break on one side of the defect, and new bounds form on the other side, resulting in the movement of the extra layer for one Burgers vector. Thus a series of single slips can move two crystal halves with respect to each other, pushing the dislocation out of structure (see Fig. 1.9). The required activation energy for dislocation slip may be provided by shear stress. In fcc structures, slip occurs within the close-packed {111} planes and along the <110> directions [35], which include the the shortest lattice vectors, $a = \frac{\sqrt{2}}{2}a_c$, and hence the shortest Burgers vector.

Suppose that the close-packed layers shown in Fig. 1.10(a) correspond to two adjacent layers in an fcc structure, where the atoms in blue and red are originally in sites C and A respectively. A perfect edge dislocation requires the translation of an atom in site A to the nearest site of the same type. In the figure, this nearest site is chosen along the $[\bar{1}01]$ direction whose corresponding Burgers vector is denoted by $\vec{b} = \frac{a_c}{\sqrt{2}}\hat{e}_{[\bar{1}01]}$, where a_c denotes the lattice parameter and $\hat{e}_{[\bar{1}01]}$ stands for the unit vector along the $[\bar{1}01]$ direction, both defined for the cubic unit cell. As it is shown in Fig. 1.10(b), the symmetry of the {111} plane provides an alternative path for the motion: from A at origin to a site of type B along the $[\bar{2}11]$ direction with Burgers vector $\vec{b}_1 = \frac{a_c}{\sqrt{6}}\hat{e}_{[\bar{2}11]}$, and then from B to A at destination with $\vec{b}_2 = \frac{a_c}{\sqrt{6}}\hat{e}_{[\bar{1}\bar{1}2]}$. This results in a crystal with two dislocations, bordering an area where atoms have been displaced from their original stacking positions. Regarding to our discussion in previous section, an intrinsic stacking fault occurs in this area. The Burgers vectors associated to these two dislocations, $\vec{b}_1$ and $\vec{b}_2$, are not translation vectors of the fcc lattice. Generally such dislocations are called *partial dislocations*, and necessarily border a two-dimensional defect, usually a stacking fault. Partial Burgers vectors and stacking faults thus may exist if the packing of atoms defining the crystal has additional symmetries not found in

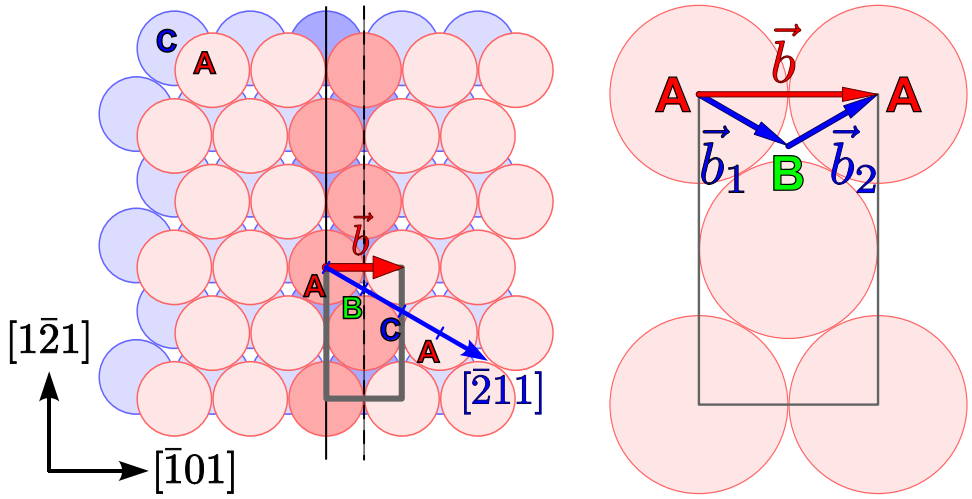

(a) (b)

Figure 1.10: (a) Top view of the {111} plane of an fcc structure, as a slip plane for an edge dislocation along the [1$\bar{2}$1] direction. Note that a perfect edge dislocation in this lattice requires insertion of two atomic layers, which have been highlighted here. (b) The Burgers vector of the perfect edge dislocation can be split into two shorter Burgers vectors, along [$\bar{2}$11] and [$\bar{1}\bar{1}$2] directions.

the lattice. These additional symmetries can appear where multiple atoms with proper symmetrical arrangement are placed in a lattice point.

The dissociation of a perfect dislocation to partials, as was explained here, substitutes the Burgers vector $\vec{b}$ with two shorter vectors $\vec{b}_1$ and $\vec{b}_2$. These two vectors are inclined at 60° to one another, hence their corresponding partials repel each other. Although the crystal restores its perfect lattice arrangement behind the partials, a ribbon of stacking fault is created as partials move apart. These partial dislocations with Burgers vectors of length $\frac{a_c}{\sqrt{6}}$ along the <112> directions and glissile on the {111} planes are called *Shockley partials* [35]. The procedure of dissociation of a perfect edge dislocation to extended dislocation consisting of two Shockley partials and an enclosed stacking fault is presented in Figs. 1.11 and 1.12. Fig. 1.11 depicts the perfect edge dislocation with dislocation and Burgers vectors along [1$\bar{2}$1] and [$\bar{1}$01] directions, respectively. In the figure, all atomic sites are indicated as spheres painted according to their stacking position along the {111} direction. For better imagination of the lattice periodicity along the [$\bar{1}$01] direction, only every second atomic plane is depicted. The inserted extra atoms and their layers are highlighted. Fig. 1.12 depicts the Shockley partials separated by distance d. Here, beside the inserted extra atoms, those atomic sites which are displaced due to the SF are highlighted too. Close to the slip plane, atomic bounds which are distorted due to the SF are highlighted by turquoise color.

The procedure of Shockley-partials separation influences the total energy of crystal by three terms. First of all, since in the fcc lattice $b = \frac{a_c}{\sqrt{2}}$ and $b_1 = b_2 = \frac{a_c}{\sqrt{6}}$, and

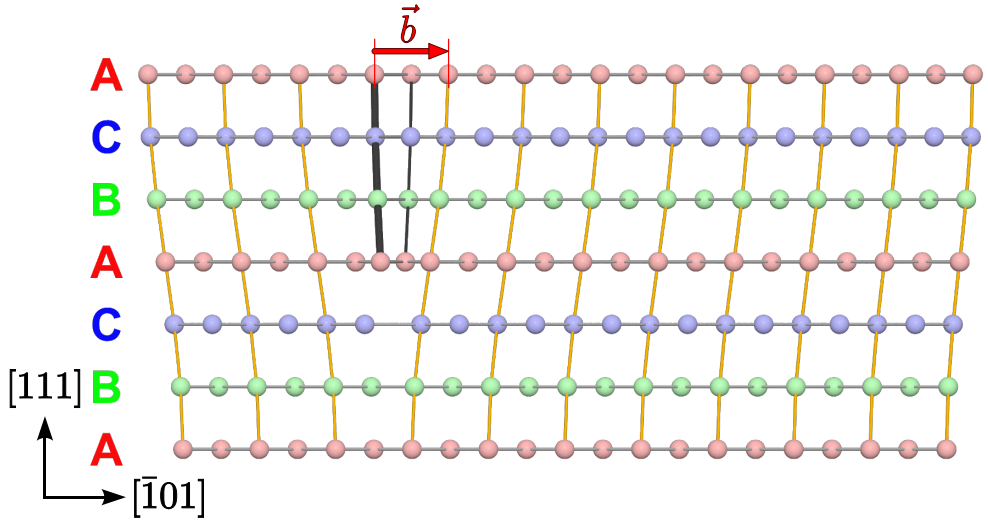

(a)

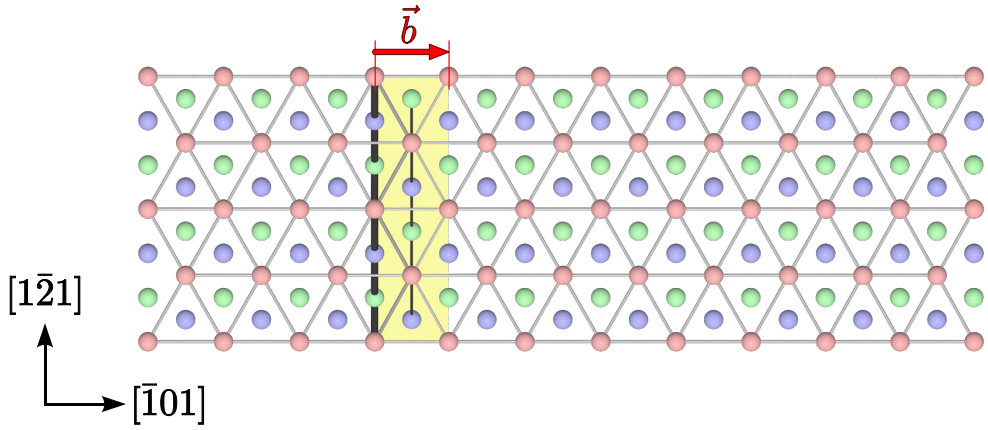

(b)

Figure 1.11: (a) A perfect edge dislocation in an fcc structure, as it is looked at along the dislocation line. (b) The same dislocation, as it is looked at from top.

hence $b^2 > b_1^2 + b_2^2$, the dissociation of Shockley partials lowers the dislocation energy (see Eq. 1.9). This energy change is not dependent on the distance d between partials. The second term is based on the interaction between two partials. Partials repel each other, and the interaction energy decreases by a factor of $1/d$. Based on this term alone, the partial dislocations would maximize the distance d. The third term altering the total energy is the energy increment upon the stacking fault which is stretched out by the dissociation of partials. This term is proportional to the SFE as the energy change per area, and the total area of the SF, which increases by d. Based on this term alone, the partial dislocations would minimize the distance d. In total, the crystal

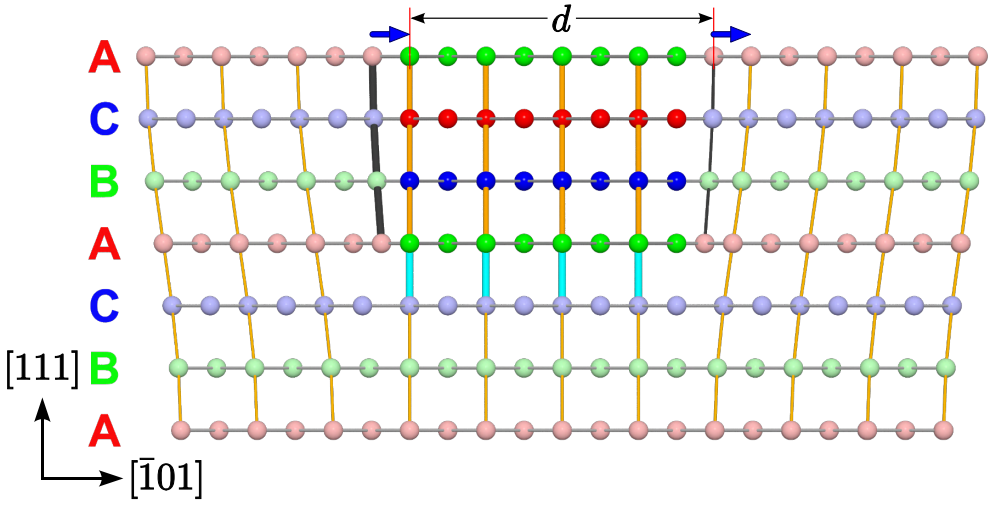

(a)

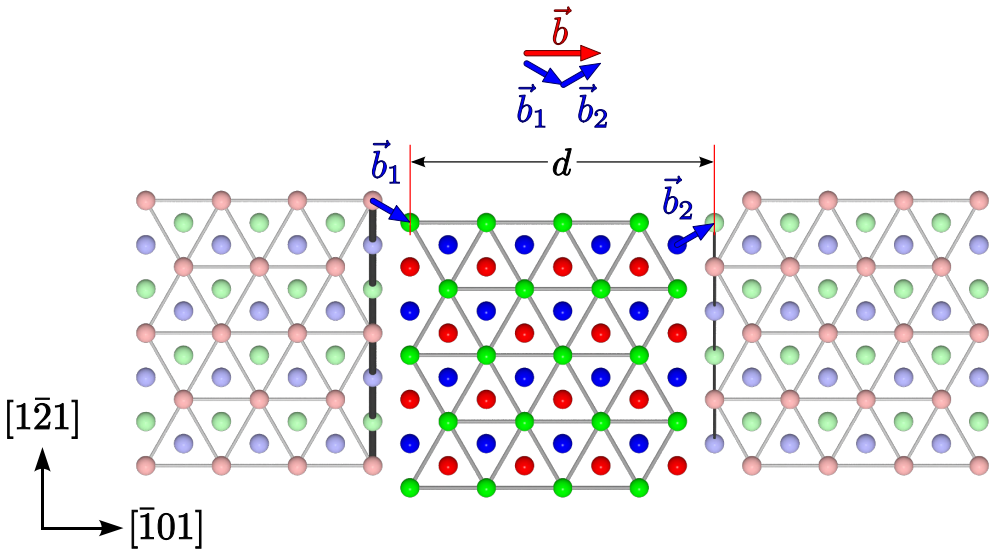

(b)

Figure 1.12: (a) Dissociation of a perfect edge dislocation to two Shockley partials, as it is looked at along the dislocation line. (b) Top view of the Shockley partials.

energy decrease by the partial dissociation, while the distance d is determined by an equilibrium between other two terms. This equilibrium d is mainly depend on the SFE, so that for a lower value of the SFE a larger separation between Shockley partials is expected.

1.4 The Importance of the SFE

Plastic deformations in fcc metals may occur through different mechanisms including partial and perfect dislocation gliding, twinning (resulting in the twinning induced plasticity, TWIP), and phase transformation (resulting in the transformation induced plasticity, TRIP). The SFE is a crucial parameter for understanding plastic deformation of fcc metals, since it governs the activation of these mechanisms. Although dislocation gliding is present everywhere, it is the dominant mechanism where the SFE is quite high. The TWIP mechanism generally occurs in stable austenite where the Gibbs free energy of the martensitic transformation ($\Delta G^{\gamma\rightarrow\epsilon}$, where γ and ϵ stand for austenite and martensite phases with fcc and hcp structures, respectively) is positive and the stacking fault energy fcc is in moderate range. The TRIP mechanism, on the other hand, is revealed in metastable austenite where the mentioned $\Delta G^{\gamma\rightarrow\epsilon}$ is negative and the stacking fault energy is rather low, which implies preferential formation of the hexagonal close packed ϵ phase [36, 37, 38].

The role of the SFE in behavior of fcc alloys under mechanical stresses has quantitatively been studied for high-manganese steels. Frommeyer *et al.* [36] have reported the dominance of the phase transformation for $\gamma_{\mathrm{SFE}} \leq 16$ mJ/m^2, and twining for $\gamma_{\mathrm{SFE}} \approx 25$ mJ/m^2. Grässel *et al.* [37] reported the dominance of the phase transformation for $\gamma_{\mathrm{SFE}} \leq 20$ mJ/m^2 and twining for $\gamma_{\mathrm{SFE}} > 20$ mJ/m^2. Allain *et al.* have reported that martensitic transformation is the dominant mechanism at low values of the SFE, *i.e.*, $\gamma_{\mathrm{SFE}} \leq 18$ mJ/m^2, twining occurs for moderate values, $12 < \gamma_{\mathrm{SFE}} \leq 18$ mJ/m^2, and for higher values dislocation gliding is favored [38].

1.5 The SFE Measurements

There is no direct way for measuring the SFE. However, several experimental methods have been used to determine the stacking fault energy. The most direct methods involve observation (by electron microscopy) of dislocation nodes, loops, and tetrahedra. Less direct methods include the measurement of x-ray texture, third-stage single-crystal work-hardening rates, and combined x-ray measurements of stacking-fault probability and dislocation density [9].

Not only the the measurement method, but also the sample preparation may strongly influence the experimental results. Bampton et. al have reported that different heat treatments applied to samples highly scatter the SFE values measured by observation of dislocation nodes. However, they show that the SFE values measured by observation of isolated dislocations are not dependent on these heat treatments [12]. The experimental values for the SFE are highly questionable since their reported ranges are too broad. For instance, Reed and Schramm [9] have summarized the reported SFE for five fcc metals, Ag, Au, Cu, Al, and Ni. Considering only the most direct methods and omitting others, they came up with average SFE for every element, as presented in Tab. 1.1.

As it is obvious from table, even the most consistent measurements result in a very

Table 1.1: The SFE measurements, summarized by Reed and Schramm [9].

Metal	Average [mJ/m^2]	Range [mJ/m^2]	Δ [%]
Silver (Ag)	22	16–31	−27–+41
Gold (Au)	50	42–61	−16–+22
Copper (Cu)	62	48–85	−23–+37
Aluminum (Al)	183	110–210	−34–+15
Nickel (Ni)	220	160–300	−27–+36

brad range, sometimes more than 35% variance with respect to the average value. Because of these controversies among published results and also technical difficulties which are present in the measurement processes, a theoretical approach for evaluating the SFE is highly motivated. Moreover, at the moment in many fields of industry, empirical approaches are employed in order to estimate the SFE and predict the plastic behavior of materials. A theoretical study would lead to a phenomenological understanding of the topic, which is of great importance for designing new materials.

2

Metallurgy

2.1 Iron

Steels are mainly consist of iron, thus a good starting point for understanding steels is studying solid iron. With [Ar].$3d^6.4s^2$ ground state electron configuration, the four unpaired 3d electrons are responsible for atomic magnetic moments of iron. At room temperature, these magnetic moments are aligned parallel within ferromagnetic domains, resulting in the well known ferromagnetic properties of iron. The lattice structure of iron at these temperature is the body-centered cubic (bcc), so called *ferrite* and denoted as α-iron.

As temperature increases, the random thermal agitation of atoms decreases the alignment within each domain. At the Curie temperature $T_c = 770$ °C $= 1043$ K, the ferromagnetic phase transfers to the paramagnetic phase, where magnetic moments are totally random oriented. Although the lattice structure remains unchanged, the new phase is historically known as β-iron. The bcc structure remains stable until temperature reaches $T^{\alpha\leftrightarrow\gamma} = 912$ °C $= 1185$ K, at which the structure transfers to fcc, so called *austenite* and denoted as γ-iron. The fcc lattice of austenite is more dense than the bcc lattice of ferrite, resulting in higher density of austenite by 2%. At higher temperature, *i.e.*, $T^{\gamma\leftrightarrow\delta} = 1394$ °C $= 1667$ K, the fcc lattice transfers to the paramagnetic bcc structure, which is denoted as δ-iron. Finally, at $T_c = 1538$ °C $=$ 1811 K, this δ-iron is melted.

2.2 Carbon Steels

Carbon steel is steel where the main interstitial alloying constituent is carbon. The American Iron and Steel Institute (AISI) defines carbon steel as the following [39]:

> Steel is considered to be carbon steel when no minimum content is specified or required for chromium, cobalt, columbium (niobium), molybdenum, nickel, titanium, tungsten, vanadium or zirconium, or any other element to be added to obtain a desired alloying effect; when the specified minimum

> for copper does not exceed 0.40 percent; or when the maximum content specified for any of the following elements does not exceed the percentages noted: manganese 1.65, silicon 0.60, copper 0.60.

Carbon steels, due to their wide range of strength, hardness, and ductility as well as their lower costs, are by far the most frequently used steels. Variations in carbon content have a great effect on mechanical properties of alloy. The addition of interstitial carbon up to 2 wt.% combined with an appropriate heat treatment increases the strength and hardness of steels and decreases its ductility. Higher carbon concentrations, however, decrease the strength and hardness. Moreover, regardless of the heat treatment, interstitial carbon decreases the melting point of steels [40].

Generally speaking, carbon steels contain up to 2 wt.% total alloying elements and can be subdivided into low-carbon steels, medium-carbon steels, high-carbon steels, and ultrahigh-carbon steels. Beyond this, an alloy of iron and carbon with carbon content within the range of 2–4 wt.% is called *cast iron*. The classification of carbon steels based on their carbon content is as the followings [39]:

- **Low-carbon steels** contain up to 0.30 wt% C. While their low carbon content disables hardening through heat treatment, it enables excellent formability in cold working.
- **Medium-carbon steels** are similar to low-carbon steels except that the carbon ranges from 0.30 to 0.60 wt%. This level of carbon content allows hardening through heat treatment. They make a balance between ductility and strength and have good wear resistance.
- **High-carbon steels** contain from 0.60 to 1.00 wt% C, which makes them very strong.
- **Ultrahigh-carbon steels** are experimental alloys containing 1.0 to 2.0 wt% C. They can be tempered to great hardness.

2.2.1 Thermodynamics of Carbon Steels

The addition of carbon significantly alters the phase stability of iron. Here we present the principle phases in carbon steels.

2.2.1.1 Carbon Steel: Ferrite (α)

In an iron-carbon alloy, the ferrite phase is a solid solution of iron and carbon with iron atoms arranged in a bcc lattice and carbons occupying interstitial vacancies. In the bcc structure, there are two types of interstitial vacancies, octahedral vacancies and tetrahedral vacancies. An Octahedral vacancy is an irregular octahedron, whose faces are isosceles rectangles of base a_{bcc} and equal sides $\frac{\sqrt{3}}{2}a_{\text{bcc}}$ (see Fig. 2.3(a)). The same triangles can compromise an irregular tetrahedron, so called tetrahedral vacancy (see Fig. 2.3(b)). Using the hard ball representation for atoms, the vacancy radius is

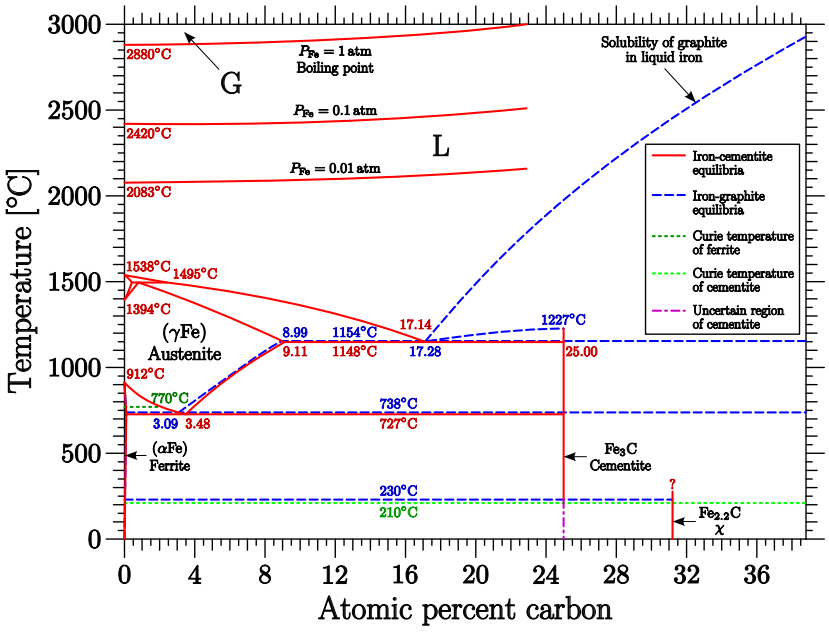

(a)

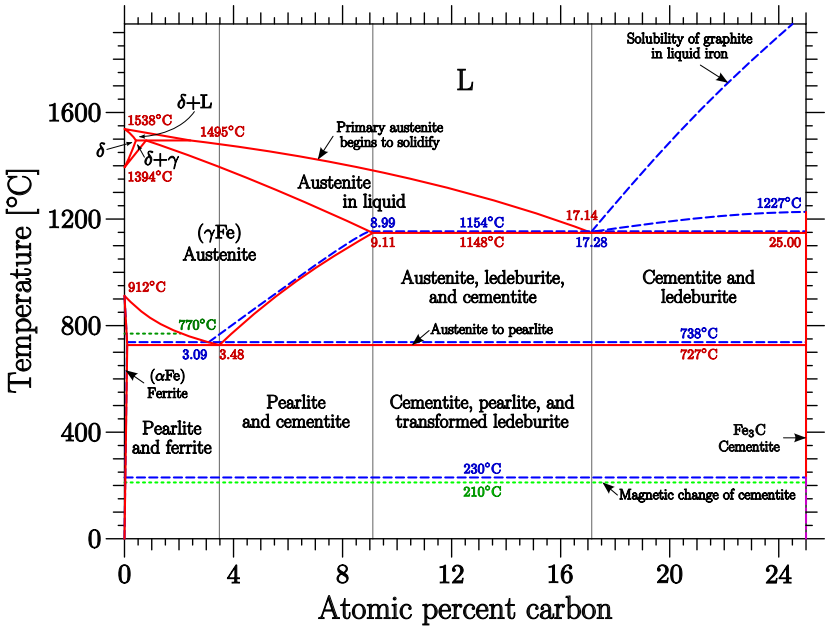

(b)

Figure 2.1: (a) Equilibrium phase diagram for the iron-carbon alloys in a wide range of concentration and temperature. The picture is a reproduction of the original diagram from *Binary Alloy Phase Diagrams*[1]. (b) The phase diagram for a range of lower carbon concentrations. The diagram was taken from *Materials Science and Metallurgy*[2].

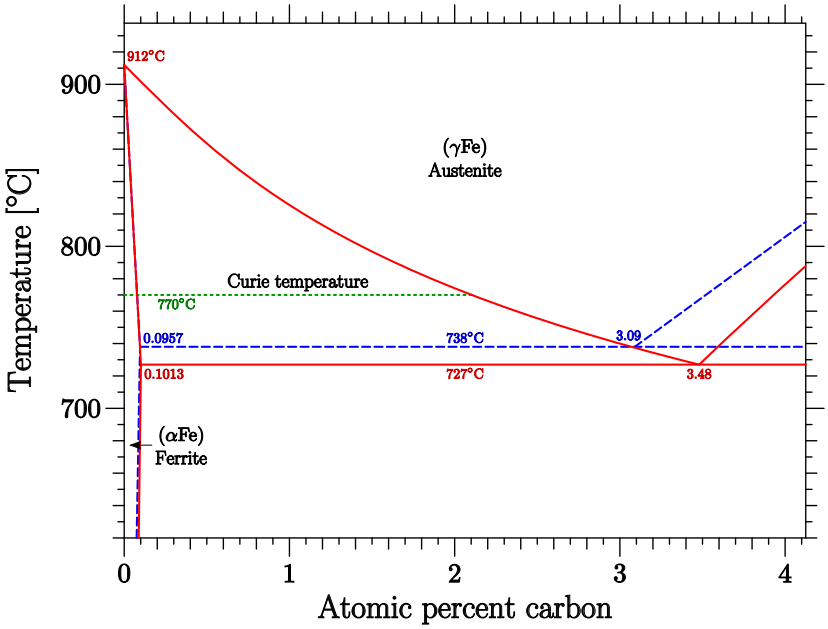

Figure 2.2: The Fe-C phase diagram for low carbon contents.

defined as the radius of the largest sphere which can be placed at the vacancy without overlapping with other atomic spheres. Taking into account that the radius of atomic spheres in a bcc structure is $\frac{\sqrt{3}}{4}a_{\text{bcc}}$, the ratio between the vacancy radius and the radius of iron atoms is found $\frac{2}{\sqrt{3}} - 1 \approx 0.1547$ and $\sqrt{\frac{5}{3}} - 1 \approx 0.2910$ for octahedral and tetrahedral vacancies, respectively. Although the radius of the tetrahedral vacancy is larger than that of the octahedral vacancy, experimental [41] and *ab initio* [42] studies show that carbon prefers to accommodate in tetrahedral sites. The metallic radius of iron and the covalent radius of carbon are 1.24 Å and 0.77 Å, respectively [43], thus the radius of a carbon atom is estimated to be 0.62 of that of iron atoms. It shows that both sites, in their initial configuration, are far too small for accommodating carbon. However, after relaxation of atomic forces, carbon atoms prefer to stay in distorted octahedral sites where they have only two iron atoms close to them, rather than four close iron atoms in the tetrahedral sites [42].

The small size of the octahedral vacancies makes it difficult to accommodate carbon atoms, thus the solubility of carbon in α-iron is very low, maximum 0.0218 wt.% (0.1013 at.%) at 727 °C. This limited solubility restricts the existence of the pure α-phase of the carbon steel in a very small area in the phase diagram (see Feg. 2.2). The α-ferrite is relatively soft and is ferromagnetic at temperatures below 768 °C [44].

As carbon concentration increases, a mixture of different phases like ferrite, cementite, pearlite, and ledeburite becomes stable. Cementite, also known as iron carbide, is a chemical compound of iron and carbon, with the formula Fe_3C, containing 6.67% carbon by mass. Since it is a chemical compound, unlike solid solutions, its carbon

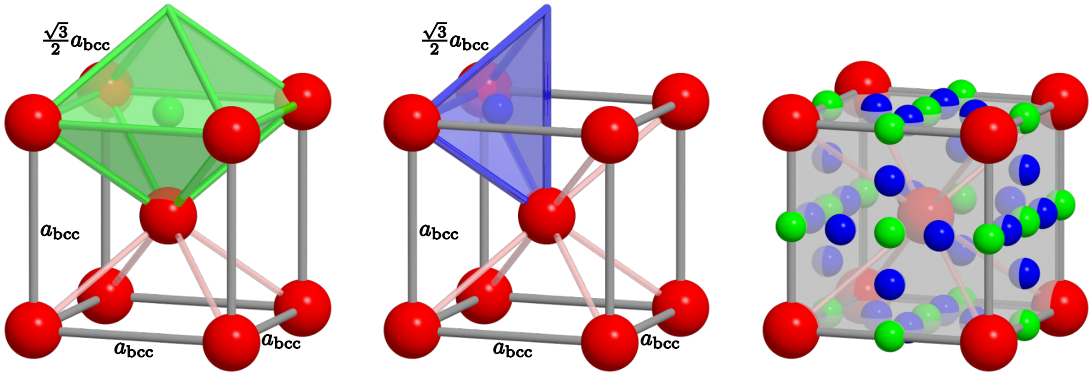

(a) (b) (c)

Figure 2.3: (a) An octahedral vacancy in a bcc structure, forming an irregular octahedron. An interstitial site is defined at its center, depicted by a green small sphere. (a) A tetrahedral vacancy in a bcc structure, forming an irregular tetrahedron. An interstitial site is defined at its center, depicted by a blue small sphere. (c) In every cubic unit cell of the bcc structure, there are six octahedral vacancies, three with centers lying on cell faces, and the other three with centers on the middle of the cell sides. There are also 12 tetrahedral vacancies, all with centers on the cell faces.

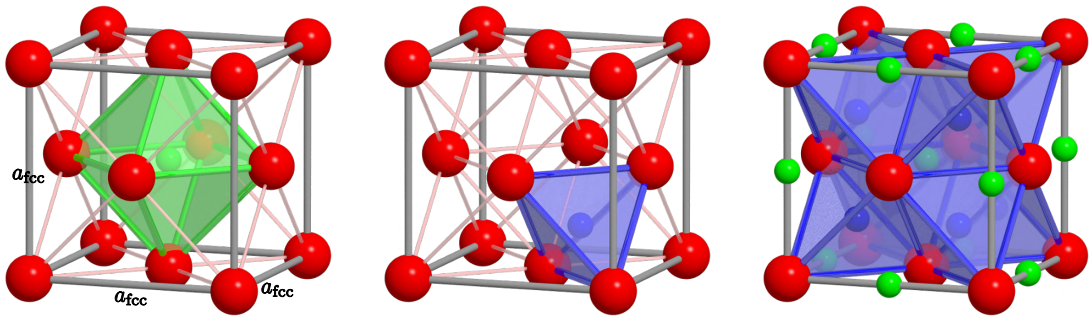

(a) (b) (c)

Figure 2.4: (a) An octahedral vacancy in an fcc structure, forming a regular octahedron. An interstitial site is defined at its center, depicted by a green small sphere. (b) A tetrahedral vacancy in an fcc structure, forming a regular octahedron. An interstitial site is defined at its center, depicted by a blue small sphere. (c) In every cubic unit cell of the fcc structure, there are four octahedral vacancies, one entirely confined at the center of cell, and others with centers on the middle of cell sides. There are also eight tetrahedral vacancies, entirely confined in the cell.

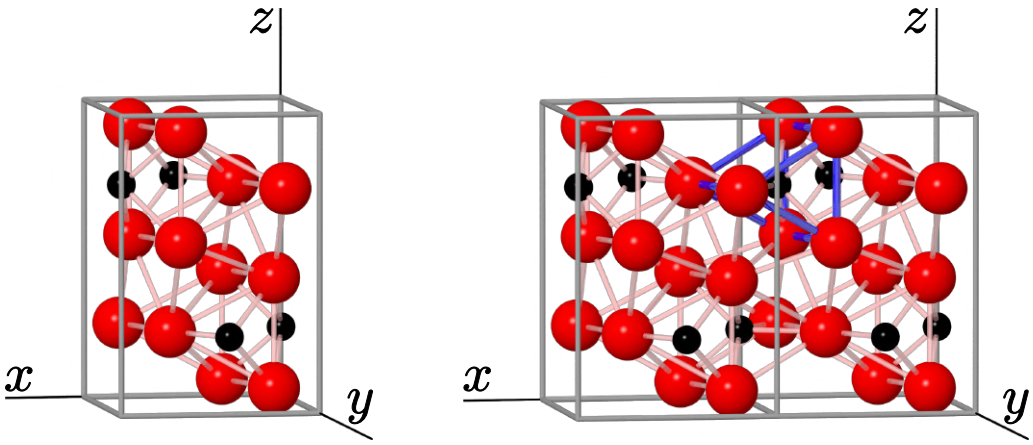

(a) (b)

Figure 2.5: (a) The unit cell of cementite with 12 iron and four carbon atoms. (b) Repetition of the unit cell along x-axis shows prismatic vacancies occupied by carbon. One prism has been highlighted for better imagination.

content is always fixed. It means that, in the phase diagram, the pure cementite phase exists only in a very narrow region, more accurately a vertical line, at carbon concentration of 6.67 wt.%. Cementite has an orthorhombic crystal structure, with 12 iron and four carbon atoms in unit cell (see Fig. 2.5(a)). Experimental [45] and theoretical [46] studies show that the interstitial carbon prefers to occupy prismatic vacancies rather than octahedral vacancies (see Fig. 2.5(b)). Mechanically, cementite is a very hard and brittle material, whose presence may greatly enhanced the strength of some steels [44].

Pearlite, also known as eutectoid steel, is a two-phases structure, composed of alternating layers of ferrite and cementite. Ferrite layers are much thicker than cementite layers, with the relative layer thickness of approximately 8 to 1 [44]. In an iron-carbon alloy, during slow cooling pearlite forms by a eutectoid reaction as austenite is below the eutectoid temperature, 727 °C. At temperatures below this, an iron-carbon alloy forms a mixture of ferrite and pearlite in the left side of eutectoid point ($x_C < 0.77$ wt.%) and a mixture of pearlite and cementite in the right side of the point ($x_C > 0.77$ wt.%). Mechanically, pearlite has properties intermediate between the soft, ductile ferrite and the hard, brittle cementite [44].

Ledeburite is a mixture of austenite and cementite, and forms at temperatures below 1148 °C in iron-carbon alloys. As temperature decreases, the austenite is converted into pearlite at temperatures below 727 °C.

2.2.1.2 Carbon Steel: Austenite (γ)

In an iron-carbon alloy, the austenite phase is a solid solution of iron and carbon with iron atoms arranged in an fcc lattice, and carbons occupying interstitial vacancies. The mentioned octahedral and tetrahedral vacancies are present in the fcc structure too,

however, here both are regular bodies of sides $a_{\text{fcc}}\frac{\sqrt{2}}{2}$ (see Fig. 2.4). While the packing of atoms in the fcc lattice is denser compared to the bcc structure, the vacancies in the fcc lattice are larger too. Taking into account that the radius of atomic spheres in an fcc structure is $\frac{\sqrt{2}}{4}a_{\text{fcc}}$, the ratio between the vacancy radius and the radius of iron atoms is limited to $\sqrt{2}-1 \approx 0.4142$ and $\sqrt{\frac{3}{8}}-\frac{1}{2} \approx 0.1124$ values for octahedral and tetrahedral vacancies, respectively. Unlike the bcc lattice, in the fcc structure, carbon accommodates in the larger vacancy. Experimental observations [47] as well as theoretical studies based on molecular dynamics [48] and *ab initio* calculations [42] agree in the fact that, in fcc iron, interstitial carbon prefers octahedral over tetrahedral coordination.

Because of larger holes between iron atoms in the fcc structure, austenite holds more carbon than ferrite. However, still the addition of carbon expands the lattice. According to the phase diagram, austenite can holds a maximum of 2.11 wt.% (9.11 at.%) of carbon at 1148 °C, which is almost 100 times bigger than the maxim carbon content in ferrite. As carbon content increases further, a mixture of austenite, ledeburite, and cementite is formed.

2.3 Stainless Steels

Stainless steels, also known as inox steels, are generally defined as corrosion resistant iron-based alloys with a minimum of about 11 % chromium content by mass (according to the European standard EN10088) [3, 49]. The chromium content in these steels combines with oxygen and forms a thin, invisible layer of chrome-containing oxide. Due to the ability of the chromium atoms and oxide molecules to pack together tightly, such a layer with a thickness of only a few atoms protects the steel underneath from further oxidation. Although stainless steel does not corrode, rust or stain with water as ordinary steel does, it is not fully stain-proof, most notably under low oxygen, high salinity, or poor circulation environments [citation]. Stainless steels are usually used in applications where both the properties of steel, *i.e.*, strength and fabricability, and resistance to corrosion are required.

Austenitic stainless steels, also known as 300 series, have an fcc crystal structure. Carbon is usually kept to low levels (C < 0.08 w.%) in these grades, while chromium content ranges from 16 to 28 w.% and nickel content ranges from 3.5 to 32 w.%. This chemical composition allows them to maintain an austenitic structure from cryogenic temperatures up to the melting point of the alloy. These alloys cannot be hardened through heat treatment. The key properties of these types of stainless steel are excellent corrosion resistance, ductility and toughness [49]. The most widely used steel in this category, is the 304 grade, containing 18–20 w.% Cr and 8–12 w.% Ni, which possesses an excellent combination of mentioned properties.

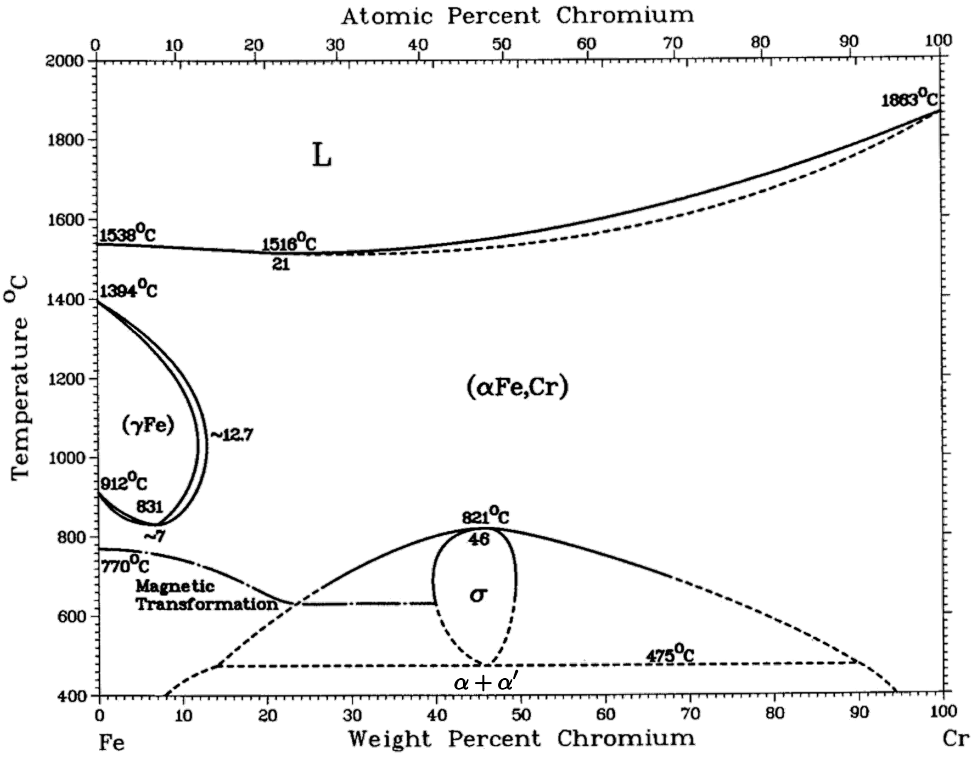

Figure 2.6: The iron-chromium phase diagram taken from *Binary Alloy Phase Diagrams* [1].

2.3.1 Thermodynamics of Stainless Steels

In stainless steels, the result of the large number of alloying elements in relatively high concentrations is that these alloys can have many stable phases concurrently. Here we introduce the principal phases found in stainless steels.

Md30=413-462(C+N)-9.2(Si)-8.1(Mn)-13.7(Cr)-9.5(Ni)-18.5(Mo)

2.3.1.1 Ferrite (α)

Crystallographic structure of a solid may vary with temperature. For example, many metals, included iron, have a less-dense bcc structure at high temperature and transform to a denser fcc structure at lower temperatures. However, iron has the curious characteristic of transforming from fcc back to the low-density bcc at still lower temperatures (see Fig. 2.6). This is a result of the unpaired 3d orbital electrons (those that give rise to ferromagnetism) that are not given up as valence electrons, causing repulsive forces between atoms and requiring a more widely spaced structure. This sequence of phase transitions shows that the free energies of both structures are close to each other [3].

The basis of stainless alloys is, of course, iron. Alloying elements that promote one structure over the other can therefore change which one predominates. The element

which provides the corrosion resistance in stainless steels, chromium, has bcc structure and hence has the characteristic of stabilizing the bcc phase. As chromium is added to iron, the temperature range over which austenite is stable grows smaller until, at about 12% chromium, ferrite becomes stable at all temperatures. This is, coincidentally, the approximate level of chromium needed to keep alloys from rusting under ambient conditions, but this effect is not related to whether the structure is bcc or fcc [3]. The iron-chromium phase diagram (Fig. 2.6) shows the composition and temperature regions where ferrite (α), martensite (α'), austenite (γ), and sigma phase (σ) are stable.

Although chromium is the principal ferrite-promoting alloying element, silicon, aluminum, molybdenum, tungsten, niobium, and titanium all favor ferrite. However, they do not produces the quality of corrosion resistance. On the other hand, carbon, nitrogen, manganese, nickel, and copper are austenite-promoting alloying element and expand the temperature range over which austenite exists. Elements that are insoluble in iron at austenite-forming temperatures, such as the impurities phosphorus, sulfur, and oxygen, have no influence on which phase is favored. At lower temperatures, the ferrite-promoting elements also promote the formation of intermetallic compounds generally composed of iron, chromium, and some of those alloying elements.

Carbon and nitrogen re quite soluble in molten iron-chromium alloys and are fairly soluble in ferrite at high temperatures. However, this solubility decreases exponentially with temperature so that it is essentially zero at room temperature. Since these elements have small atomic sizes compared to iron and chromium, after dissolving they diffuse into interstitial sites within the bcc matrix. Such interstitial solute atoms profoundly distort the structure. The fcc structure is denser than the bcc and hence can provide roomier interstitial spaces. This causes that these interstitials are much more soluble in the fcc structure, and stabilize it over the bcc. To preserve the ferrite structure, carbon and nitrogen must be eliminated. There are still additional reasons to eliminate carbon and nitrogen in stainless steels. During cooling as these elements become less and less soluble, they must precipitate. The most thermodynamically favorable form in which they can precipitate is as a compound of chromium, with which they are very reactive. This occurs at the grain boundaries, where nucleation is favored, and depletes those regions of chromium, rendering them less corrosion resistant. A second effect is a loss of toughness due to these precipitates. The diffusion rates of carbon and nitrogen in ferrite are too high to prevent this precipitation by quenching. Even modern refining methods can not reduce the concentration of carbon and nitrogen to low enough levels. So, to avoid the detrimental effects of chromium carbide and nitride formation in ferrite, other benign carbides and nitrides such as those of titanium or niobium are allowed to form preferentially. This approach is called *stabilization* and is used for most ferritic alloys today. The older approach, is to permit chromium carbides and nitrides to form but then to perform a subcritical anneal to re-homogenize the chromium and coarsen the precipitates so that they have only a small negative effect on mechanical properties. Moreover, in ferritic alloys, stabilizing makes it much easier to keep chromium from segregating. It maintains the homogeneity of the alloy, which is essential for a proper corrosion resistance.

The bcc structure of ferrite allows more rapid diffusion than does the fcc structure of austenite. This is true for both the interstitial diffusion of the elements helium, boron, carbon, nitrogen, and oxygen and the substitutional diffusion of all other elements. The rate of diffusion of all elements, both interstitial and substitutional, in ferrite is about two or three orders of magnitude higher than in austenite. The practical implication of this is that precipitation reactions generally cannot be suppressed by quenching in ferrite if they involve interstitial elements, whereas they can be in austenite. Intermetallic phases can form more rapidly in ferrite. This becomes an issue only when total chromium plus molybdenum exceeds about 20%, above which the sigma (σ) phase appears.

Ferrite has a greater thermal conductivity and lower thermal expansion than austenite. Its strength decreases with temperature more than that of austenite, but the good match in thermal expansion between the ferrite and its oxide still makes it an excellent high-temperature material. Ferrite has very nearly the same corrosion resistance as austenite, but since ferrite can hold no nitrogen in solution, it cannot benefit from this element.

2.3.1.2 Austenite (γ)

The second major constituent phase of the stainless steel alloy system is austenite which has an fcc atomic structure. The fcc structure is common in many transition metals to the right of iron in the periodic table. As stated, the fcc structure should be considered normal for metals well below their melting temperature as it is a denser structure. The presence of the bcc structure relates to the unpaired 3d electrons, which provide ferromagnetism. Adding elements to iron that causes pairing of the 3d electrons diminishes ferromagnetism and promotes the fcc structure. Nickel and manganese are the most prominent alloying elements that do this, but the interstitials carbon and nitrogen are the most powerful austenite stabilizers on a percentage basis. Their use is limited by their solubility and their tendency to form precipitating compounds with chromium. Manganese acts largely through its ability to promote nitrogen solubility.

Since all stainless steels contain principally iron and chromium, the addition of a substantial amount of austenitizing elements is necessary to transform the structure to austenite. As a rule of thumb, iron alloys require about 17% chromium and 11% nickel (or its equivalents) to remain austenitic at room temperature. One percent nickel can be replaced by about 2% manganese as long as nitrogen is present to maintain the same phase stability. The omnipresent carbon and nitrogen have an effect 30 times that of nickel, so even in the small amounts in which they are normally present, they have a significant effect.

In an alloy, the phase with the lowest free energy is most favored, but others may have low enough free energies that permit them to exist. Transition from one metastable phase to the equilibrium state, the one of the lowest energy, may require atomic rearrangements to reach the equilibrium compositions on an atomic scale. If diffusion is too sluggish for these rearrangements to take place, the structure may retain the prior metastable configuration indefinitely. That is why most stainless steels are used

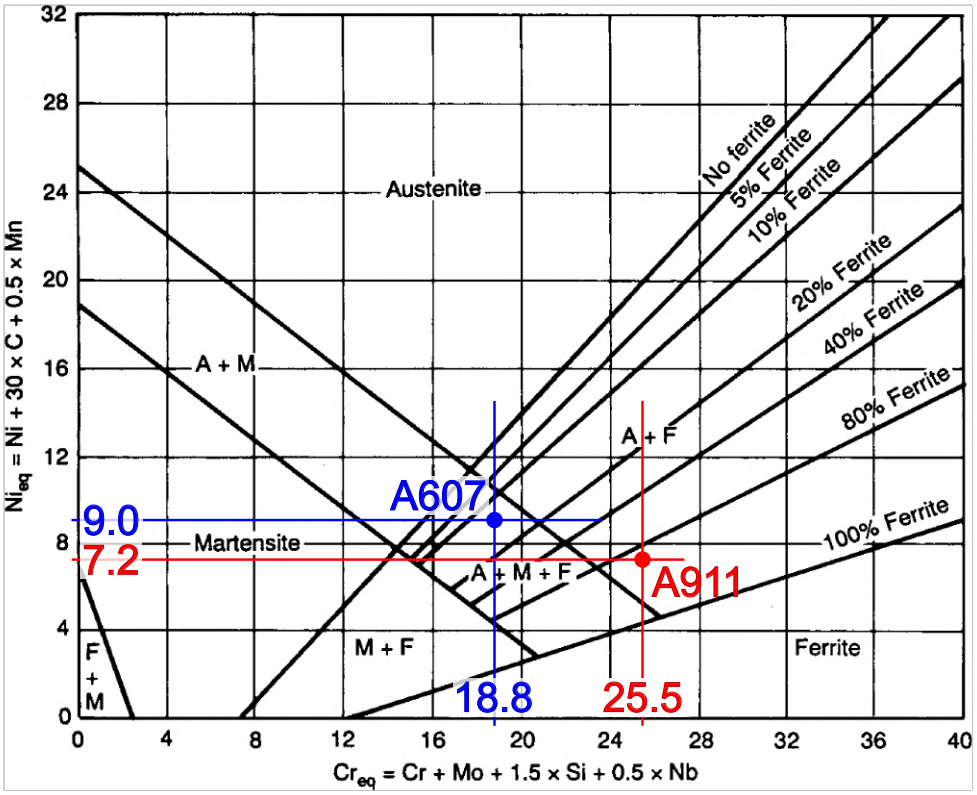

Figure 2.7: Schaeffler-Delong constitution diagram showing phases present in as-solidified stainless steels at room temperature as a function of composition. In this diagram, Cr, Mo, Si, and Nb push the system toward the ferrite phase (Cr-like effect), while Ni, Mn, and C push it toward the austenite phase (Ni-like effect). The diagram has been taken from M. F. McGuire, *Stainless Steels for Design Engineers*, 2008, p 12 [3].

in the metastable condition. For example, the common alloy 304 (also called 18-8 due to 18 w.% Cr and 8 w.% Ni) is normally used in the fully austenitic condition. It would *rather* be partly ferritic, but the substitutional diffusion of chromium in austenite which is required to form a ferrite phase of a separate composition is so slow that it can not occur in terrestrial time frames. However, if energy is applied by mechanical shear, the austenite can transform to the lower free-energy martensite phase without diffusion [3].

The structure of final product can be influenced by various parameters like heat treatment and mechanical working. That is why samples of the same chemical composition may be found in different phases, or they may even have different lattice parameters in the same phase. These conditions requires different sets of phase diagrams according to different production processes. Here we present two sets of diagrams: The Schaeffler-Delong constitution diagram which is used for predicting the metastable phases in rapidly solidified (as-solidified) stainless steels, and the equilibrium pseudo-

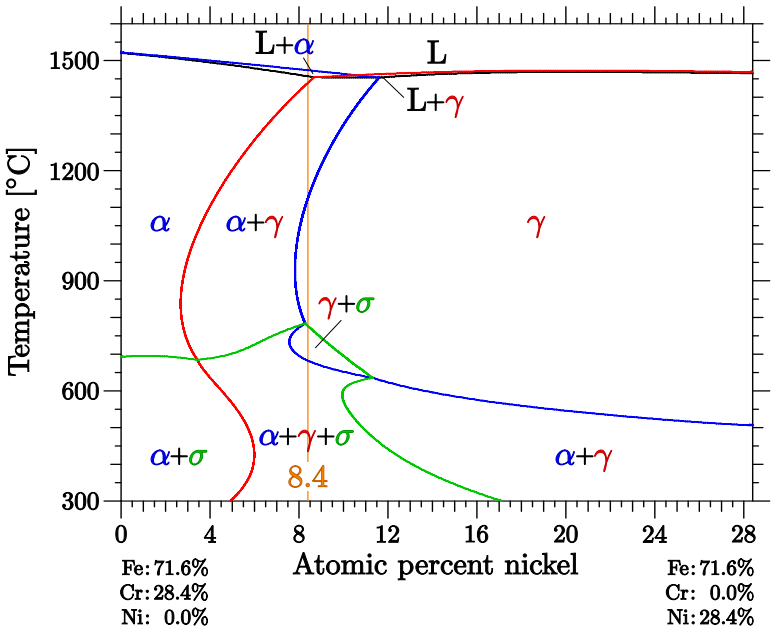

Figure 2.8: The equilibrium pseudo-binary phase diagram evaluated by Thermo-Calc software, where the concentration of iron has been selected according to the A607 alloy.

binary phase diagrams for specific concentration of iron.

The Schaeffler-Delong constitution diagram predicts the presence of different metastable phases in stainless steels at room temperature. An example of such diagram for weld metals is presented in Fig. 2.7. Since welds solidify relatively rapidly, no carbides or intermetallic phases form, and only ferrite, austenite, and martensite will be present. The horizontal axis depicts the concentration of a group of alloying elements which would push the system toward the ferrite phase. The main element in this group is chromium. However, to some extends, the chromium content may be replaced by other elements while maintaining the ferrite-preferring effect. For example, 1.0 % of chromium can be replaced by 1.0 % of molybdenum (Mo), 0.67 % of silicon (Si), or 2.0 % of niobium (Nb). Thus in the diagram, the parameter $Cr_{eq.}$ is defined which denotes the sum of concentrations of all ferrite-preferring elements in the alloy: $Cr_{eq.} = Cr+Mo+1.5\times Si+0.5\times Nb$. In a similar way, the vertical axis depicts the concentration of a group of alloying elements which would push the system toward the austenite phase. In the diagram, these effects are summarized in the parameter $Ni_{eq.}$ which is defined as $Ni_{eq.} = Ni+30\times C+0.5\times Mn$ [3]. Considering rapid solidification and neglecting other alloying elements else but chromium and nickel, the diagram shows that A607 alloy would solidify as a mixture of three phases, *i.e.*, austenite, martensite, and more than than 10 % ferrite.

However, the equilibrium phase diagrams show different phase combinations for two mentioned alloys. In Fig. 2.8 a phase diagram is presented where the iron contents is kept according to A607. On this diagram, the chemical composition corresponding to A607 has been depicted by a vertical line.

3

Theoretical Background

In the condensed matter physics and chemistry, we are interested to find the structure of materials in a scale which is small enough to allow us to ignore the internal structure of particles. Considering such scale, material can be considered as a system of nuclei and electrons. Generally, finding the structure of this system is a difficult task because of two reasons: first, the particles must be treated using the lows of quantum mechanics, rather than classical physics, and second, the number of particles in a small piece of material is so high making it impractical to study them individually. It is for this second issue that the structure of matter is known as the quantum many-body problem. In this chapter a very short review is presented on the theoretical background of the computational methods we have used in this study. For compiling the text, except the references which are explicitly cited, some parts of the PhD theses written by Peter Puschnig [50], Oleg Peil [51], Tetyana Khmelevska [52], and Philip Peter Rushton [53] have been reviewed.

An exact solution of the mentioned quantum many-body problem can be obtained using the Schrödinger equation [54, 55]. For any non-relativistic time-independent system, this equation is given as

$$\hat{H}\Psi(\mathbf{r}_1, \mathbf{r}_2, \mathbf{r}_3, \ldots, \mathbf{r}_N) = E\Psi(\mathbf{r}_1, \mathbf{r}_2, \mathbf{r}_3, \ldots, \mathbf{r}_N), \tag{3.1}$$

where $\hat{H}$, $\Psi(\mathbf{r}_1, \mathbf{r}_2, \mathbf{r}_3, \ldots, \mathbf{r}_N)$, and E are the Hamiltonian, the many-body wavefunction and the total energy of the system, respectively. Since the particles are interacting according to the Coulomb low, the Hamiltonian can be expressed as

$$\begin{aligned}\hat{H} = &-\sum_{i=1}^{M} \frac{\hbar^2}{2m_{Z_i}} \nabla^2_{\mathbf{R}_i} - \sum_{i=1}^{N} \frac{\hbar^2}{2m_e} \nabla^2_{\mathbf{r}_i} + \frac{1}{4\pi\epsilon_0} \sum_{i=1}^{M} \sum_{j>i}^{M} \frac{Z_i Z_j}{|\mathbf{R}_i - \mathbf{R}_j|} \\ &- \frac{1}{4\pi\epsilon_0} \sum_{i}^{N} \sum_{j=1}^{M} \frac{eZ_j}{|\mathbf{r}_i - \mathbf{R}_j|} + \frac{1}{4\pi\epsilon_0} \sum_{i=1}^{N} \sum_{j>i}^{N} \frac{e^2}{|\mathbf{r}_i - \mathbf{r}_j|},\end{aligned} \tag{3.2}$$

where M and N are the number of nuclei and electrons in the system, m_Z, Z, and $\mathbf{R}$ are the mass, the charge, and the position of the nuclei, m_e, e, and $\mathbf{r}$ represent are the

mass, and charge, and the position of an electron. The first two terms in 3.2 are the kinetic energy contributions from the nuclei and the electrons, respectively, while the rest are the Coulombic potential energy terms arising from the ion-ion repulsion, ion-electron attraction and the electron-electron repulsion, respectively. The Schrödinger equation 3.1 is simply too difficult to solve directly with this Hamiltonian in its exact form. The goal of this chapter is to introduce some practical methods which would solve the Schrödinger equation by approximating the Hamiltonian 3.2.

The nuclei are of order $\sim 10^3$ times heavier than the electrons, so can be considered to be stationary with respect to the electrons. This approximation is the first simplification to the mentioned many-body problem, and is known as the Born–Oppenheimer approximation, after their work published in 1927 [56]. Based on this approximation, nuclei are considered at fix positions, and their effect is taken into account by a constant term related to their interactions among themselves, and a fixed external potential acting on electrons. This simplifies the full many-body Hamiltonian 3.2 as

$$\hat{H} = E_{\text{nuc.}} - \sum_{i=1}^{N} \frac{\hbar^2}{2m_e} \nabla_{\mathbf{r}_i}^2 - \frac{1}{4\pi\epsilon_0} \sum_{i}^{N} \sum_{j=1}^{M} \frac{eZ_j}{|\mathbf{r}_i - \mathbf{R}_j|} + \frac{1}{4\pi\epsilon_0} \sum_{i=1}^{N} \sum_{j>i}^{N} \frac{e^2}{|\mathbf{r}_i - \mathbf{r}_j|}, \tag{3.3}$$

where $E_{\text{nuc.}}$ is the electrical potential energy stored in the fixed arrangement of nuclei. Although the Born–Oppenheimer approximation simplifies the Hamiltonian by reducing the many-body (electrons and nuclei) problem to the many-electron problem, it is still impractical to solve the Schródinger equation in a solid containing $N \sim 10^{26}$ electrons and consequently $3N$ variables.

In order to find an accurate enough solution for the many-electron problem, a number of methods have been developed, where the real system is approximated by a simplified virtual system with practical solution. In 1927, by approximating the many-electron wavefunction Ψ as a product of single-electron wavefunctions ψ, Hartree [57, 58] proposed one of the earliest and the most simple approximate solutions to the problem,

$$\Psi(\mathbf{x}_1, \mathbf{x}_2, \ldots, \mathbf{x}_N) = \psi_1(\mathbf{x}_1)\psi_2(\mathbf{x}_2)\ldots\psi_N(\mathbf{x}_N) \tag{3.4}$$

where $\mathbf{x}_i$ represent the pair $(\mathbf{r}_i, s_i)$, in which $\mathbf{r}_i$ and s_i are the position and the spin of the ith electron in system. Although this methods uses the Pauli exclusion principle [59] forbidding the presence of two electrons in the same quantum state, the many-electron wavefunction does not obey the Fermi statistics [60], which requires it to be antisymmetric with respect to the electron and the position exchanges. Later, in order to respect the principle of antisymmetry of the wavefunction, a new approximation was introduced where the many-electron wavefunction is considered as a Slater determinant [61] composed of many single-electron wavefunctions

$$\Psi(\mathbf{x}_1, \mathbf{x}_2, \ldots, \mathbf{x}_N) = \frac{1}{\sqrt{N!}} \begin{vmatrix} \phi_1(\mathbf{x}_1) & \phi_2(\mathbf{x}_1) & \cdots & \phi_N(\mathbf{x}_1) \\ \phi_1(\mathbf{x}_2) & \phi_2(\mathbf{x}_2) & \cdots & \phi_N(\mathbf{x}_2) \\ \vdots & \vdots & \ddots & \vdots \\ \phi_1(\mathbf{x}_N) & \phi_2(\mathbf{x}_N) & \cdots & \phi_N(\mathbf{x}_N) \end{vmatrix}. \tag{3.5}$$

This definition ensures the antisymmetry of the many-electron wavefunction with respect to any electron or position exchange. The present method was published by Fock [62], and is known as the Hartree–Fock approximation. Since a single Slater determinant results in poor description of the system, a better approximation is achieved by constructing the many-electron wavefunction as a linear combination of multiple Slater determinants describing also the excited configurations. However, considering the computational efficiency, this method is not practical for solids.

In the late 1920s, Thomas and Fermi [63, 64] established a theory where, for the first time, the electron density, $n(\mathbf{r})$ was chosen as the main unknown variable, instead of the many-electron wavefunction. This choice simplifies the problem significantly, as the degrees of freedom are reduced dramatically from $3N$ to 3, *i.e.*, the x, y, z coordinates of the system. Later, in 1960s, the electron density became the basis of the density functional formalism which is described in this chapter. In the rest of this chapter we use atomic units, whereby $\hbar = e = m_e = 4\pi\epsilon_0 = 1$.

3.1 Hohenberg-Kohn Theorems

Density functional theory (DFT) is based on two simple, but extremely important, theorems known as Hohenberg-Kohn Theorems [65]. Here we present these two theorems as stated in the book authored by Martin [66]. Their proof can be found in the book.

- **Theorem 1.** For any system on interacting particles in an external potential $V_{\text{ext}}(\mathbf{r})$, the potential $V_{\text{ext}}(\mathbf{r})$ is determined uniquely, except for a constant, by the ground state particle density $n_0(\mathbf{r})$.

It is then concluded from this theorem, that all properties of the system are completely determined given the ground state density $n_0(\mathbf{r})$ [66].

- **Theorem 2.** A *universal functional* for the energy $E[n]$ in terms of the density $n(\mathbf{r})$ can be defined, valid for any external potential $V_{\text{ext}}(\mathbf{r})$. For any particular $V_{\text{ext}}(\mathbf{r})$, the exact ground state energy of the system is the global minimum value of this functional, and the density $n(\mathbf{r})$ that minimizes the functional is the exact ground state density $n_0(\mathbf{r})$.

From this theorem, it can be concluded that the functional $E[n]$ alone is sufficient to determine the ground state energy and density [66].

Although the Hohenberg-Kohn theorems proof the existence of an exact solution for the ground state of the system, they do not offer an approach for its calculation. In 1965, about one year after the work by Hohenberg and Kohn [65], Kohn and Sham [67] proposed a simple method for the DFT calculations which is described in the next section.

3.2 The Kohn-Sham Formulation

In this section, we shortly discuss the method proposed by Kohn and Sham [67], in order to find the system ground state. The many-electron system is an interacting system, where the interactions originate from the Coulomb law, from the Pauli exclusion principle, and from the antisymmetry of the many-electron wavefunction. However, in the Kohn-Sham formulation, the full interacting system with the real potential is mapped onto a fictitious non-interacting system, with the same ground-state density as of the real system. The same ground-state density of these two systems assures that the Kohn-Sham method is still exact. In this non-interacting system, the electrons move within an effective single-particle potential $v_{\mathrm{KS}}(\mathbf{r})$, known as "Kohn-Sham" potential. This simplification greatly facilitates the calculation.

Kohn and Sham [67] suggested to write the energy functional in the form of

$$F[\tilde{n}(\mathbf{r})] = T[\tilde{n}(\mathbf{r})] + \frac{1}{2}\int \frac{\tilde{n}(\mathbf{r})\tilde{n}(\mathbf{r}')}{|\mathbf{r}-\mathbf{r}'|} d^3r\, d^3r' + E_{\mathrm{xc}}[\tilde{n}(\mathbf{r})] \tag{3.6}$$

where the $T[\tilde{n}(\mathbf{r})]$ is the kinetic energy functional for the non-interacting electrons, the second term is is the electro-static Hartree energy, and $E_{\mathrm{xc}}[\tilde{n}(\mathbf{r})]$ is the so-called exchange-correlation energy functional. Note that, $F[\tilde{n}(\mathbf{r})]$ is purely related to the system of electrons, *i.e.*, it is independent of the external potential. By applying the Hohenberg–Kohn minimum principle, Kohn and Sham introduce an approach which can find the ground-state properties of the system in through a self-consistent algorithm. Following the detailed approach as presented in the book authored by Parr and Yang [68], the ground-state energy of the electronic system is finally found in the form of

$$E = \sum_{i=1}^{N} \epsilon_i + E_{\mathrm{xc}}[n(\mathbf{r})] - \int v_{\mathrm{xc}}(\mathbf{r}) n(\mathbf{r}) d^3r - \frac{1}{2}\int \frac{n(\mathbf{r})n(\mathbf{r}')}{|\mathbf{r}-\mathbf{r}'|} d^3r\, d^3r', \tag{3.7}$$

where ϵ_i is the eigenvalue associated to the single electron state ψ_i, $n(\mathbf{r})$ is the electron density, $E_{\mathrm{xc}}[n(\mathbf{r})]$ is the exchange-correlation energy functional, and $v_{\mathrm{xc}}(\mathbf{r})$ is the derivation of the exchange-correlation energy with respect to the electron density:

$$n(\mathbf{r}) = \sum_{i=1}^{N} |\psi_i(\mathbf{r})|^2 \tag{3.8}$$

and

$$v_{\mathrm{xc}}(\mathbf{r}) = \frac{\delta}{\delta \tilde{n}(\mathbf{r})} E_{\mathrm{xc}}[\tilde{n}(\mathbf{r})]\bigg|_{\tilde{n}(\mathbf{r})=n(\mathbf{r})} \tag{3.9}$$

All many-body effects can be taken into account in the calculation of the ground state if the exact form of $E_{\mathrm{xc}}[n(\mathbf{r})]$ is known. Thus, the usefulness of the Kohn–Sham formalism is entirely depend on whether good approximations of the $E_{\mathrm{xc}}[n(\mathbf{r})]$ are available or not.

As presented here, the Kohn-Sham formalism reduces the problem of minimizing the energy functional to the problem of solving a set of single-electron Schrödinger equations. Various approaches have been developed in order to solve these single-electron

equations, differing mainly in the choice of the basis set for the single-particle orbitals. As a sequence of the choice, they are different in performance as well [66]. In solid state calculations, two basic classes of methods are used: Hamiltonian methods, based on the direct diagonalization of the Hamiltonian; and Green's function techniques relying on the multiple-scattering formalism. In the remaining part of these two approaches are shortly discussed.

3.3 The APW+lo Method

In order to solve the Kohn–Sham equations for an electronic system, the wavefunction must be expanded using an appropriate basis set. Generally, a good basis set must be simultaneously *unbiased*, *simple*, and *efficient*. Unbiased means that the basis set must not assume any preconceptions of the form of the problem. Simplicity requires the ease of implementation, which would require less technical efforts. And finally, the efficiency is determined by the number of the basis functions which are required in order to get accurate enough representation of the expanded wavefunction.

When studying periodic crystals, planewaves $e^{i(\mathbf{k}+\mathbf{K})\cdot\mathbf{r}}$ are a natural choice of basis functions, as they are compatible with the periodic boundary conditions. Here, $\mathbf{k}$ denotes a vector in the first Brillouin zone, and $\mathbf{K}$ is a reciprocal lattice vector. Moreover, planewaves are unbiased and technically very simple to implement. Using planewaves basis set, any eigenfunction of a periodic Hamiltonian can be expanded as

$$\Psi^n_{\mathbf{k}}(\mathbf{r}) = \sum_{\mathbf{K}} c^{n,\mathbf{k}}_{\mathbf{K}} e^{i(\mathbf{k}+\mathbf{K})\cdot\mathbf{r}}. \tag{3.10}$$

Despite the above mentioned advantages of the planewaves, they are not efficient, particularly when trying to construct the quick oscillations of the wavefunction near the nucleus. In order to describe the quick changes of the wavefunction in this regions, a large number of basis functions are needed which increases the computational burdens significantly.

One solution to this problem is using pseudopotentials which, in a region close to the nucleus, approximate the quickly changing real potential with a smooth virtual potential in order to reduce the number of required basis functions [69, 70, 71]. Despite to their efficiency, pseudopotential approaches are not a relevant choice when studying material properties which involve core electrons.

The augmented plane wave (APW) [72, 73, 74] method is another attempt to overcome the efficiency problems associated with the planewave basis set. In this approach, the unit cell is partitioned into two regions: the *muffin-tin* region which is a spherical space centered at the nucleus with radius R_{MT}, and the *interstitial* region (I) which is generally known as the spaces far from the nucleus. In the interstitial region, where electrons are far away from nucleus, electrons are almost free, and hence can be easily described using the planewave basis set. On the other hand, in the region near the nucleus, electrons behave almost as if they were in an isolated atom, and therefore can be described well using the atomic orbitals. The crystal wavefunction is expanded in

terms of the APW basis functions $\phi^{\mathbf{k}}_{\mathbf{K}}$

$$\Psi^n_{\mathbf{k}}(\mathbf{r}) = \sum_{\mathbf{K}} c^{n,\mathbf{k}}_{\mathbf{K}} \phi^{\mathbf{k}}_{\mathbf{K}}(\mathbf{r}, \epsilon), \tag{3.11}$$

where [74]

$$\phi^{\mathbf{k}}_{\mathbf{K}}(\mathbf{r}, \epsilon) = \begin{cases} \sum_l \sum_{m=-l}^{l} A^{\alpha,\mathbf{K}}_{lm} U^{\alpha}_l(r, \epsilon) Y_{lm}(\hat{\mathbf{r}}) & r' < R^{\alpha}_{\mathrm{MT}} \\ \frac{1}{\sqrt{V}} e^{i(\mathbf{k}+\mathbf{K})\cdot\mathbf{r}} & r \in I \end{cases} \tag{3.12}$$

Here, V is the unit-cell volume, and $\mathbf{r}' = \mathbf{r} - \mathbf{r}^{\alpha}$ where $\mathbf{r}^{\alpha}$ is the atomic position of atom α within the unit cell. $U^{\alpha}_l(r, \epsilon)$ is the numerical solution to the radial Schrödinger equation at the energy ϵ. The coefficients $A^{\alpha,\mathbf{K}}_{lm}$ are chosen such that the atomic functions, for all l, m components match the planewave with $\mathbf{k} + \mathbf{K}$ at the muffin-tin sphere boundary R^{α}_{MT}.

Inside the muffin-tin sphere, an accurate description of the Kohn–Sham orbital $\psi_i(\mathbf{r})$ requires the coefficient ϵ to be selected equal to the energy eigenvalue ε_i of $\psi_i(\mathbf{r})$. Therefore, for every energy eigenvalue ε_i a different energy-dependent set of APW basis functions must be found. This leads to a nonlinear eigenvalue problem which is computationally very demanding, and hence known as the main drawback on the APW method [74].

A successful attempt to improve the APW method was the linearization by Andersen [75], which led to the first implementation of the linearized augmented plane-wave LAPW method [76]. In the LAPW method the energy dependence of the radial functions inside each sphere is linearized by adding a second term to the radial part of the basis functions [74]

$$\phi^{\mathbf{k}}_{\mathbf{K}}(\mathbf{r}, \epsilon) = \begin{cases} \sum_l \sum_{m=-l}^{l} \left[A^{\alpha,\mathbf{K}}_{lm} U^{\alpha}_{1l}(r, \epsilon) + B^{\alpha,\mathbf{K}}_{lm} \dot{U}^{\alpha}_{1l}(r, \epsilon) \right] Y_{lm}(\hat{\mathbf{r}}) & r' < R^{\alpha}_{\mathrm{MT}} \\ \frac{1}{\sqrt{V}} e^{i(\mathbf{k}+\mathbf{K})\cdot\mathbf{r}} & r \in I \end{cases} \tag{3.13}$$

Here, U_{1l} is the solution to the radial Schrödinger equation at a fixed linearization energy ϵ_{1l}, and $\dot{U}_{1l}$ is its energy derivative computed at the same energy. The LAPW's, as defined above, are sufficiently flexible basis which can describe eigenfunctions with energy eigenvalues around the linearization energy. Therefore, the ϵ_{1l} values can be kept fixed and all energy eigenvalues can be obtained with a single diagonalization, resulting in a significant efficiency improvement [74].

However, LAPW's, are not suited for treating states that lie far from the linearization energy. Furthermore, the linearization is not sufficiently accurate for broad valence

bands if the partial wave shows a large energy variation inside the muffin-tin sphere. To improve the linearization, Singh [77] introduced local orbitals (LO's) to augment the LAPW basis set for certain l values [74]

$$\phi_{\mathrm{LO}}(\mathbf{r}) = \begin{cases} \left[A_{lm}^{\alpha,\mathrm{LO}} U_{1l}^{\alpha}(r') + B_{lm}^{\alpha,\mathrm{LO}} \dot{U}_{1l}^{\alpha}(r') + C_{lm}^{\alpha,\mathrm{LO}} U_{2l}^{\alpha}(r')\right] Y_{lm}(\hat{\mathbf{r}}) & r' < R_{\mathrm{MT}}^{\alpha} \\ 0 & r \in I \end{cases} \tag{3.14}$$

An LO is constructed by the LAPW radial functions at the energy ϵ_{1l} and a third radial function $U_{2l}^{\alpha}(r')$ at a second energy ϵ_{2l}, chosen to most efficiently improve the linearization. The three coefficients are determined by the requirements that the LO's should have zero value and slope at the muffin-tin sphere boundary and the normalization. LO's were found to be more efficient in improving the linearization than alternative methods with APW's having continuous second and third derivatives [77].

Later, Sjöstedt *et al.* [78] suggested an important modification of the LAPW method. They introduced an APW+lo basis, where the APW's, Eq. 3.12, are evaluated at a fixed energy and flexibility is added by including another type of local orbitals (denoted as lo's) combining a U and $\dot{U}$

$$\phi_{\mathrm{lo}}(\mathbf{r}) = \begin{cases} \left[A_{lm}^{\alpha,\mathrm{lo}} U_{1l}^{\alpha}(r') + B_{lm}^{\alpha,\mathrm{lo}} \dot{U}_{1l}^{\alpha}(r')\right] Y_{lm}(\hat{\mathbf{r}}) & r' < R_{\mathrm{MT}}^{\alpha} \\ 0 & r \in I \end{cases} \tag{3.15}$$

The lo's are evaluated at the same fixed energy as the corresponding APW's. The two coefficients are determined by the normalization and the condition that $\phi_{\mathrm{lo}}(\mathbf{r})(R_{\mathrm{MT}})$ has zero value. In this version, the $\dot{U}_l$ is independent from the PW's and only included for a chosen set of "physically important" l-quantum numbers.

Koelling and Arbman pointed out that LAPW converges somewhat slower than the APW method with respect to the number of basis functions [76]. The LAPW basis functions are required to be differentiable at the muffin-tin boundary and are therefore not optimally suited for describing the orbitals inside the sphere. Such constraints are not introduced on the APW basis set when the energy derivatives are included in form of local orbitals [78]. In the APW+lo method, the energy derivative term is only included in a few lo's and not in every PW, as in LAPW. It is therefore not obvious that the linearization of the APW+lo basis is as accurate as the LAPW scheme in all cases. However, Madsen *et al.* shown that the results calculated with the APW+lo basis set can be as accurate as those obtained using the LAPW basis set [74].

Generally, considerable computational savings can be achieved by employing an APW+lo basis set. It is has also been reported that results obtained with the APW+lo converge faster and often more systematically towards the final value. Thereby, accurate calculations can be performed at a much lower cost than with the LAPW basis set [74].

The FP-LAPW and the FP-APW+lo method are among the most accurate *ab-initio* methods [79]. These two methods have been implemented in the WIEN2k code

[79, 80]. We use the version 8.3 of this code in order to simulate the iron–carbon system. As carbon occupies interstitial sites, relaxations of atomic forces becomes significantly important. The WIEN2k code is capable of doing this task.

3.4 The EMTO Method

In this section we would try to shortly introduce the *exact muffin-tin orbitals* (EMTO) method, which is based on Green's function formulation. The text is a short summary of a more detailed discussion presented in the PhD theses by Oleg Peil [51] and Tetyana Khmelevska [52].

When disordered alloys are interested, Green's function technique becomes an essential approach as it allows to construct models of a disordered state of alloys in a systematic way [51]. The single-electron Green's function is defined as

$$\left[-\frac{1}{2}\nabla^2 + v(\mathbf{r}) - \epsilon \right] G(\mathbf{r}, \mathbf{r}', \epsilon) = -\delta(\mathbf{r} - \mathbf{r}'), \tag{3.16}$$

where G and δ are the Green's function and the Dirac delta function, respectively. Note that, here the spin indices have been ignored for simplicity. The Green's function can be explicitly represented in terms of the corresponding single-electron wave functions of the original Kohn-Sham equation as

$$G(\mathbf{r}, \mathbf{r}', \epsilon + i\xi) = \sum_{\mathbf{k}} \frac{\phi_{\mathbf{k}}(\epsilon, \mathbf{r}) \phi^*_{\mathbf{k}}(\epsilon, \mathbf{r})}{\epsilon + i\xi - \epsilon_{\mathbf{k}}}. \tag{3.17}$$

Once the Green's function is given, different quantities can be calculated. For instance, the electron density is obtained as

$$n(\mathbf{r}) = -\frac{1}{\pi} \int^{\epsilon_{\mathrm{F}}} d\epsilon \, \mathrm{Im}\big(G(\mathbf{r}, \mathbf{r}', \epsilon)\big), \tag{3.18}$$

where the upper limit of the integral is specified by the Fermi energy ϵ_{F}.

The Korringa-Kohn-Rostocker (KKR) method [81, 82] is a very efficient way of calculating the Green's function using the multiple-scattering formalism [83]. In this approach, each site is treated as a scattering center, and the solution of the original equation is obtained by demanding the self-consistency of the scattering at all sites. The scattering centers are defined by dividing the space into the atomic Wigner-Seitz (WS) cells. The solutions of the Schrödinger equation inside the cells are treated as outgoing waves. Then, the self-consistent scattering implies that the outgoing wave for a given site cancels all the waves incoming from other sites.

In the original and in many modern implementations of the KKR method, the full potential is approximated by a so-called muffin-tin potential representing a sum of spherical potentials within spheres of radius S_{MT} (muffin-tin radius) centered at atomic sites, and a constant potential in the remainder of space [81]. The cancellation of scattering waves is satisfied at the muffin-tin spheres, resulting thus in a solution of

the Schrödinger equation smooth in the entire space. The muffin-tin potential is very well justified on physical grounds in homogeneous systems with close-packed structures, but can give erroneous results in open structures with anisotropic distortions, where the full potential must be considered. A general formulation of the KKR for the case of potentials of arbitrary shape is possible within the full-potential (FP) KKR scheme [84, 85, 86, 87]. Calculations with FP-KKR are quite demanding, although affordable with modern computers.

The exact muffin-tin orbital (EMTO) method [88] belongs to the family of KKR methods. The main idea of the EMTO approach is to use large overlapping muffin-tin spheres instead of non-overlapping ones, which greatly improves the representation of the full potential in terms of the muffin-tin potential.

The method described here allows one to calculate the Green's function of a system with a periodic potential. However, disordered alloys are not translationally invariant and the method is not directly applicable. The point is that to represent a disordered alloy, a very large supercell with randomly distributed atoms in it has to be considered [89, 90]. On the other hand, one can use the one-electron Green's function, which is a self-averaging quantity, and find an average Green's function of an alloy considered as a one-component effective medium having translational symmetry of the underlying lattice.

The simplest consistent method of performing configurational averaging of the Green's function is the coherent potential approximation (CPA) [91, 92, 93] which reduces a multi-component disordered alloy to a translationally invariant system with a single component representing an effective medium. The major property of the effective medium is that its scattering properties are the same as those of the original components on average.

Studying the paramagnetic state on an alloy requires the simulation of a system of local magnetic moments with random orientations. In order to calculate the effects of magnetic disorder on the electronic structure, a mean-field like approximation called disordered local moment (DLM) [94] approach can be applied. The idea of the DLM formalism is to represent magnetic disorder within the CPA by treating magnetic metals as a pseudo-binary alloy, $\mathrm{M}^{\uparrow}_{1-x}\mathrm{M}^{\downarrow}_{x}$, where $1-x$ is the concentration of atoms of sort M with positive spin moment $\mathrm{M}^{\uparrow}$ and x of those with negative moment $\mathrm{M}^{\downarrow}$. The case of $x = 0$ describes a ferromagnetic solution, while $x = 0.5$ represents a state with positive and negative local moments equipartitionally distributed on the all magnetic sites (DLM state), thus modeling a paramagnetic state of a magnetic metal in an alloy analogy [52].

The EMTO method, in combination with the CPA and the DLM approaches provide an excellent tool in order to investigate the random alloys with any arbitrary compositions in the paramagnetic state. However, this approach does not allow to relax the atomic forces, which can be existing due to atomic size mismatch. Although these forces are not severe when calculating substitutional alloys composed of atoms of similar sizes, it becomes extremely important in the case of interstitial compounds, where the lattice around the interstitial atom is significantly distorted.

4

Fe–C Through the LAPW Method

4.1 Introduction

As it was partially explained in Chap. 2, carbon steels have numerous applications in different fields of industry, which leads to a great interest to shed light on the mechanisms relevant for their plastic deformation behavior. The plastic deformation of fcc materials is strongly governed by the SFE, as discussed in Chap. 1. This chapter is dedicated to evaluation of the SFE and the γ-surface in austenitic carbon steels.

Experimental observations [47] as well as theoretical studies based on molecular dynamics [48] and *ab initio* calculations [42] agree that, in fcc iron, carbon occupies interstitial sites, preferring octahedral over tetrahedral coordination. However, concerning the influence of carbon on the SFE in austenitic steels, experimental studies give controversial answers. An early work by Schramm and Reed [4] suggests a linear dependence of the SFE on the elemental compositions of Ni, Cr, and C in the form of

$$\text{SFE } [\text{mJ/m}^2] = 4 + 1.8\,x_{\text{Ni}} - 0.2\,x_{\text{Cr}} + 410\,x_{\text{C}}, \tag{4.1}$$

where x denotes the concentration of the respective element in weight percent. This result, exhibiting a strong dependence of the SFE on x_{C}, was based on measurements on samples with a maximum of 0.036% carbon concentration. Later, Brofman and Ansell [5] included newer experimental data from samples with carbon concentrations up to 0.29% and came up with the following modification,

$$\text{SFE } [\text{mJ/m}^2] = 16.7 + 2.1\,x_{\text{Ni}} - 0.9\,x_{\text{Cr}} + 26\,x_{\text{C}}, \tag{4.2}$$

indicating a carbon dependence which is 15 times smaller. Considering that in this class of steels we deal with carbon concentrations of the order of 0.1, and that the magnitude of the SFE is 15–60 mJ/m^2, the influence of carbon on the SFE lies within the typical experimental accuracy of $\pm$15–20 mJ/m^2 [16]. In other words, the latter measurements suggest that the SFE is very small and its dependence on the carbon

concentration is very weak. The diversity of experimental results does not only exist for the magnitude of the SFE, but it is also found in the behavior of this quantity when carbon is added. For instance, while above mentioned works predict a linear increase, Petrov [6] reported that the SFE decreases for small carbon content, while it increases for higher concentrations. This controversy in the existing literature suggests that presently the influence of carbon on the SFE is difficult to determine experimentally, and insight from theory, in particular from first principles, is highly desirable.

A strong influence on the SFE of fcc iron in the presence of interstitial atoms has already been shown by earlier theoretical studies. For instance, Kibey and coworkers [95] have found nitrogen to significantly alter the γ-surface. Moreover, for carbon concentrations up to 1.33 w%, Abbasi *et al.* [7] have reported the SFE to linearly increase with a slope of 340 $\mathrm{mJ/m^2}$ per weight-percent carbon. However, the γ-surface has not been computed for the iron-carbon system so far.

In this chapter, we present the generalized stacking-fault energy evaluated by means of *ab initio* calculations within the framework of density functional theory (DFT) [65, 96], applying the all-electron full-potential linearized augmented planewave plus local-orbital (FP-LAPW+lo) method as implemented in the WIEN2k package [97].

We study the influence of interstitial carbon on the γ-surface of fcc iron by adopting a supercell approach including the explicit ISF. We find that the γ-surface and the SFE strongly depend on the carbon concentration, and we analyze in detail how they are affected by the position of carbon atoms with respect to the stacking-fault plane.

We simulate the SF by utilizing the supercell technique. Compared to SFE calculations based on the ANNNI model [98, 99], this approach allows the calculation of the γ-surface and the relaxation of the atomic positions around the interstitial atoms and the fault. On the other hand, chemical and magnetic disorder can not be easily accounted for.

The former restriction is not severe in this case since experimental [100] and *ab initio* [42] studies show that the carbon–carbon interaction for interstitial carbons in fcc iron is repulsive, supporting the implicit assumption of a homogeneous carbon distribution by the supercell approach. Concerning magnetic effects, we note that a comparison between magnetic (ferromagnetic) and non-magnetic calculations resulted in only small differences in terms of relative changes of the SFE as a function of carbon concentration [7]. We therefore consider the Fe–C model system in the non-magnetic state. We note that for accurate computation of the absolute values of the SFE, the paramagnetic state must be taken into account [8, 101]. However, the treatment of magnetic disorder in combination with (i) large supercells and (ii) the need for local lattice relaxations, is unfortunately, out of reach within present day *ab initio* methodologies.

4.2 Methodology

We evaluate the SFE and the γ-surface explicitly, which requires finding the energy difference between two structures with proper carbon concentration, where one of them includes a SF and the other one has bulk fcc structure. For this purpose, we calculate

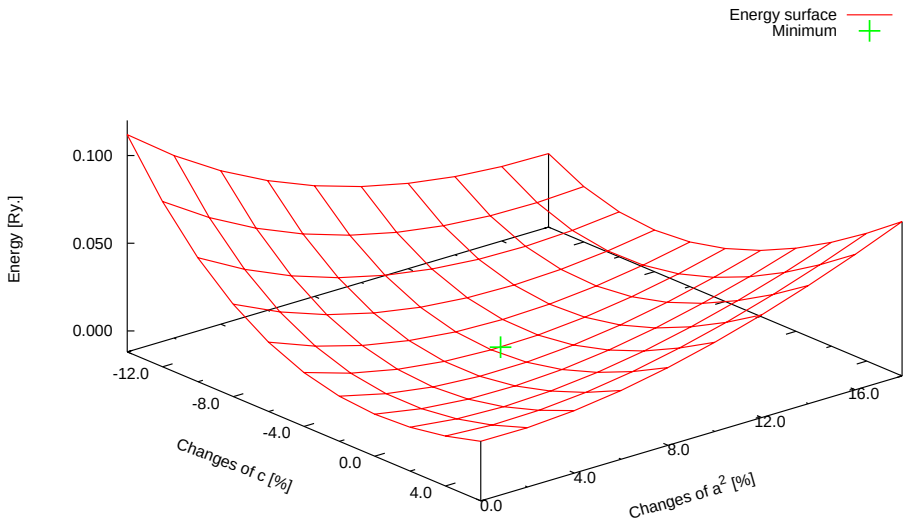

Figure 4.1: Optimization of cell dimensions for Fe_3C.

the total energy of every system utilizing the supercell method. Since every point on the γ-curve corresponds to a specific displacement in the crystal lattice, our approach requires many supercells. These supercells are constructed using blocks of bulk with perfect structure. The bulk itself requires relaxations in order to find the relevant lattice parameters and atomic positions. Once the energy differences are calculated, a relevant two-dimensional function is fitted to them in order to comprise the entire γ-surface. In this section we explain these steps in more detail.

4.2.1 Bulk Crystal Structures

Experimental data for the lattice parameter of austenite are available only for temperature-ranges where the phase becomes stable, well above the room temperature. However, the DFT simulations are performed for zero Kelvin, thus use equilibrium lattice parameters in our simulations. We calculate the equilibrium lattice parameters and atomic positions for austenite with different carbon concentrations, *i.e.*, pure iron, $Fe_{24}C$, and Fe_3C, corresponding to 0.00, 0.89, and 6.67 weight percent of interstitial carbon, respectively. The equilibrium volume for pure iron is calculated in the primitive unit-cell of the fcc structure where no force relaxation is required. For Fe_3C and $Fe_{24}C$, however, hexagonal unit-cells are utilized, where both parameters a and c are optimized independently. Moreover, since there are variable internal positions in these two cells, all atomic forces are relaxed in every step of the cell optimization. More technical details are found in the following:

- **Fe:** The structure of this element is fcc with only one atom in the unit cell, and hence no freedom for internal positions. Thus the relaxation of atomic forces is

not needed and only finding the equilibrium volume is required. We calculate the total energy for a limited number of unit-cells with slightly different lattice parameters. The equilibrium lattice parameter is then found by fitting the Murnaghan's equation of state to these calculated points (see Fig. 4.1).

- **$Fe_{24}C$**: For this compound the unit-cell is hexagonal which contains six nonequivalent iron atoms and one carbon atom. There are eight degrees of freedom for the unit-cell shape and the internal positions: the lattice parameters a and c, and the internal positions of the six nonequivalent atoms. In order to find the equilibrium configuration, we construct a limited number of unit-cells, where the cell parameters a and c have independently been changed. The total energy is calculated for these structures after the relaxation of atomic forces. The equilibrium parameters a and c are then found by fitting a two-dimensional polynomial, $f(x, y)$, to the calculated points, (a, c, E).

- **Fe_3C:** For this compound the structure is hexagonal which contains two nonequivalent iron atoms. It has three degrees of freedom: the unit-cell dimensions, a and c, and the internal position of the iron atom which is placed inside the unit-cell. The equilibrium parameters a and c are found as it was explained for $Fe_{24}C$.

The summary of the results are presented in Tab. 4.1.

Table 4.1: The equilibrium volumes for bulk structure of different compounds investigated in this work. V_{cell} denotes the unit-cell equilibrium volume, V_{atom} stands for the volume per iron atom, and ΔV shows the change in the volume by adding carbon, compared to the volume for pure iron: $\Delta V = \frac{(V_{\text{atom}})_{\text{composite}} - (V_{\text{atom}})_{\text{Fe}}}{(V_{\text{atom}})_{\text{Fe}}} \times 100$ in %.

compound	lattice type	atoms Fe	atoms C	a [a.u.]	c [a.u.]	V_{cell} [a.u.^{3}]	V_{atom} [a.u.^{3}]	ΔV %
Fe	fcc	1	0	6.524	6.524	69.42	69.42	0.00
$Fe_{24}C$	hexagonal	24	1	9.351	22.905	1734.40	72.27	4.10
Fe_3C	hexagonal	3	1	4.955	11.810	251.11	83.70	20.57

4.2.2 Supercells for the Stacking-Fault Simulations

The principle of supercell constructing for the γ-surface simulations was mentioned in chapter 1: in an fcc structure, a stacking fault can be created by fixing the atomic layers below the fault, and sliding all upper layers along the $[\bar{2}11]$ direction (see Fig. 1.6(a)). The displacement vector must span every point in $\{111\}$ plane in order to evaluate the entire γ-surface. Among different available approaches for applying this principle, we construct our supercells in a special way by considering two facts: first is that when using the supercell methods for calculating the energy differences between different

structures, for reducing the probability of occurring errors, it is highly recommended to use the same basis sets in all calculations. The second is that in the WIEN2k package, relaxing the atomic forces in the direction of lattice vectors is more straightforward than other directions. In this section we explain our method and compare it with other often used methods.

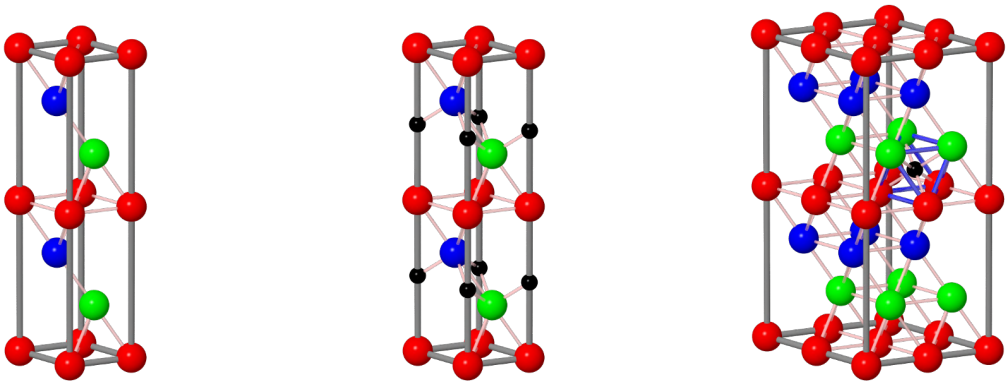

(a) (b) (c)

Figure 4.2: Bulk unit-cells which are used for constructing supercells with an ISF; (a) shows the bulk unit-cell for pure iron, and (b) for Fe_3C. (c) depicts the unit-cell for $Fe_{24}C$ with a highlighted octahedral site for better imagination.

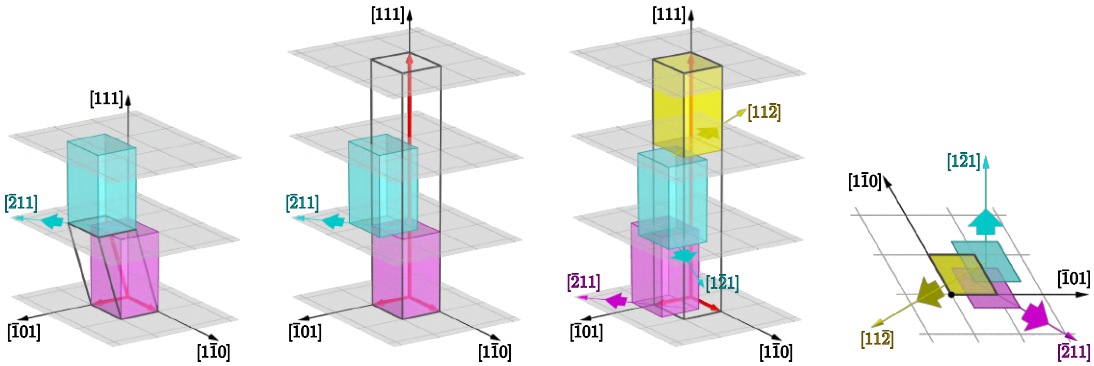

(a) (b) (c) (d)

Figure 4.3: Schematic representation of three possible supercells for γ-surface calculations. (a) depicts the *tilted*, (b) the *single-shift* supercell, and (c) and (d) show side and top views of the *triple-shift* supercell, respectively. The gray cages show the supercells including one ((a) and (b)) or three ((c)) SFs, while the boxes in different colors represent building blocks with bulk structure.

There are different ways to construct a supercell for simulating an explicit ISF in fcc structures. Here we explain three possible supercells which are suitable for *ab initio*

simulations of the ISF based on DFT codes using periodic boundary conditions. Perfect bulk unit-cells are shown in Fig. 4.2 and supercells with ISFs are represented in Fig. 4.3. Fig. 4.3(a) shows the smallest possible supercell, denoted by us as *tilted* supercell, which contains only one bulk slab. Since the cell vector $\vec{c}$ is tilted, a displacement appears between the bulk layers of the cell and its periodic image. In Fig. 4.3(b), another possible supercell is depicted containing two bulk slabs which are slided with respect to each other. In order to ensure periodic boundary conditions in z-direction, sufficient vacuum has to be added such to prevent any interaction between the slabs and their periodic images. We call it here *single-shift* supercell. Figs. 4.3(c) and 4.3(d) depict a third possibility for choosing a supercell. It is a supercell with three bulk slabs containing three SFs with displacement vectors of identical magnitude but different directions, namely $[\bar{2}11]$, $[1\bar{2}1]$ and $[11\bar{2}]$, respectively. Thus, the resulting displacement vector adds up to zero ensuring periodic boundary conditions. We call it here *triple-shift* supercell. Unlike the two former supercells where only one ISF is associated with every cell, the *triple-shift* supercell contains three ISFs per unit-cell (see Fig. 4.3(c)).

Tab. 4.2 summarizes the main features of these supercells. The *tilted* supercell exhibits the smallest cell, *i.e.*, its volume is three times smaller than that of the other two supercells, which clearly reduces the computational cost. However when structures along the γ-surface are considered, the cell shape and consequently the basis set changes for *tilted* supercell, while the other two supercells have fixed shape and dimensions. Thus, the *tilted* supercell requires higher energy cut-offs and denser k-meshes to ensure convergence of results. Moreover, since in the *tilted* supercell the cell vector $\vec{c}$ is not perpendicular to the fault plane, atomic force relaxations with the constraint that only the component perpendicular to the SF plane is relaxed, is not straightforward. These two drawbacks led us to discard the *tilted* supercell for our studies of the γ-surface. Concerning the *single-shift* supercell, it requires an additional vacuum layer which introduces surface effects, and also decreases the symmetry. The *triple-shift* supercell does not suffer from any of these difficulties. In fact, for $Fe_{24}C$, the *single-shift* supercell has 50 non-equivalent atoms, while the *triple-shift* supercell has only 25. Thus, we chose the *triple-shift* supercell for all our computations.

4.2.3 Interstitial Carbon

We use the $\cdots AcBaCbAcBaCb\cdots$ scheme for labeling the position of octahedral interstitial sites with respect to the atomic layers. Here, capital letters denote atomic positions and lowercase letters mark octahedral vacancies. The usage of the same letter in upper and lower case (for instance A and a) indicates that their corresponding sites are on top of each other when viewed along the <111> direction (see Fig. 4.4).

While in the perfect fcc structure all octahedral vacancies are naturally identical, they must be differentiated according to their distance from the fault plane in presence of a SF. We indicate this distance by the parameter d (see Fig. 4.4). For instance, $d = 0$ represents an octahedral vacancy positioned within the fault plane. Similarly, $d = 1$ denotes such a vacancy separated from the fault plane by one atomic layer, and so on. A carbon atom has different effects on the γ-curve, when positioned at octahedral

Table 4.2: Comparison of possible supercells

property	*tilted* supercell	*single-shift* supercell	*triple-shift* supercell
supercell height	L	$2L + l_{\text{vacuum}}$	$3L$
symmetry	very low	low	high
fixed supercell shape	×	✓	✓
straightforward relaxation	×	✓	✓

sites with different values of d, while all possible octahedral sites belonging to the same parameter d have identical energy due to translational symmetry. Thus, the ideal supercell for computing the γ-curve for a homogeneous distribution of interstitial carbons, should simultaneously include carbon atoms at all kinds of octahedral sites. Such a supercell requires extending along the {111} plane, so that the single-layer concentration of carbon, θ, is fixed for all layers. The supercell concentration of carbon, x, is then found equal to θ, since $x = \sum_d \theta_d / \sum_d$ (see Fig. 4.5(a)). This ideal supercell would, however, be huge and computationally impractical for low carbon concentrations. By assuming that carbon atoms influence the γ-curves independently from each other, one can investigate their impact within smaller cells, each of which including only one or a few carbon atoms (see Fig. 4.5(b)). The γ-curve is then calculated for every such small cell, and finally an average over all individual γ-curves is taken (see Fig. 4.5) according to

$$\gamma_{\text{av}} = \frac{\sum_{d=0}^{d_{\max}} \gamma_d}{d_{\max} + 1}, \tag{4.3}$$

where γ_d denotes the γ-curve obtained for a cell with an octahedral carbon at a distance d from the fault plane, and $d_{\max}$ is the maximum distance considered.

When calculating γ-surfaces, iron atoms within two atomic layers next to the SF plane are allowed to move perpendicular to the plane. However, carbon atoms in this region are fully relaxed in all directions.

4.2.4 Interpolation of the γ-surface

The complete γ-surface requires the evaluation of the energy differences for a two-dimensional grid of points in the {111} plane. However, by considering the symmetry of the surface, the problem can be reduced to the evaluation of the so-called γ-curve,

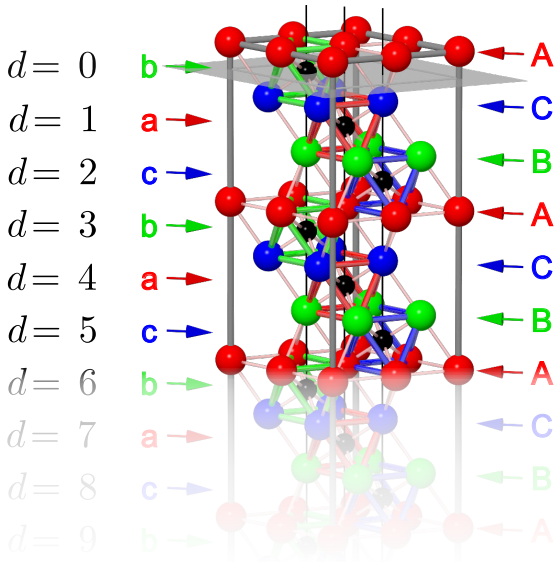

Figure 4.4: Labeling of octahedral sites with respect to atomic layers and the SF plane (gray plane). Large spheres and capital letters denote the stacking of the atomic layers in a perfect fcc lattice, while small black spheres and lower-case letters indicate the interstitial sites at the center of octahedral vacancies. For better imagination, every octahedral vacancy is highlighted by a cage, whose color corresponds to the stacking position of its site. The distance between a site and the SF plane is indicated by the parameter d.

which depicts the energy change versus displacement in the $[\bar{2}11]$ direction. The energy differences between the perfect structure and structures with SFs are calculated for displacement vectors of different sizes, 0 to $u_{[\bar{2}11]}$, along the $[\bar{2}11]$ direction (see Fig. 1.6(a)). The γ-curve and, consequently, the γ-surface are then interpolated using a Fourier series taking into account the symmetry properties of the surface, thereby recovering the full two-dimensional dependence of the γ-surface.

The general form of the two-dimensional Fourier expansion for a function $f(x, y)$ is given by

$$f(x,y) = \sum_{m,n \in Z} C_{mn} e^{i\frac{2\pi x}{a}m} e^{i\frac{2\pi y}{b}n}, \tag{4.4}$$

where m and n are integer numbers, C_{mn} denote expansion coefficients, and a and b are the periodicities along the x and y-axes, respectively. For expanding the γ-surface in the $\{111\}$ plane of an fcc structure, we select the x and y-axes along $[\bar{2}11]$ and $[0\bar{1}1]$, respectively. This choice requires $a = b\sqrt{3}$. Since the γ-surface is a real function and obeys the symmetries of the structure, the expansion should have the following features:

- a three-fold rotational symmetry of the $\{111\}$ plane,

$$R_{[111]}(240^\circ) f(x,y) = R_{[111]}(120^\circ) f(x,y) = f(x,y),$$

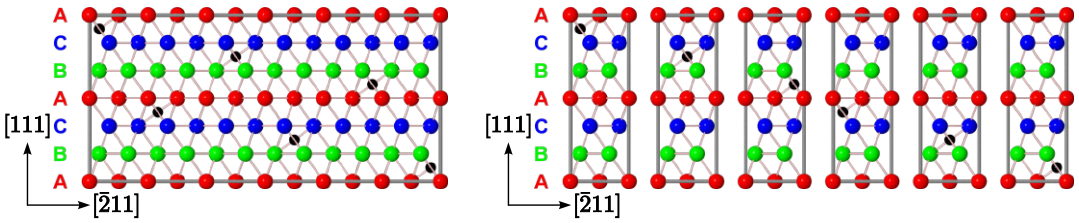

(a) (b)

Figure 4.5: (a) A supercell, where carbon atoms are distributed as homogeneous as possible among all layers. (b) The supercell is split into smaller cells, each containing only one carbon atom.

- reflection symmetry with respect to the x-axis,

$$f(x,-y) = f(x,y),$$

- and real value,

$$f^*(x,y) = f(x,y).$$

By applying these criteria to Eq. 4.4, $f(x,y)$ is obtained as

$$\begin{aligned} f(x,y) = & \qquad (4.5)\\ & \sum_{\substack{n\in Z\\ n\geq 0\\ n=2l}}{}' \left\{ p_{0n} \left[\cos(\frac{2\pi y}{b}n) + 2\cos(\frac{2\pi x}{a}\frac{3n}{2})\cos(\frac{2\pi y}{b}\frac{n}{2}) \right] \right\} \\ + & \sum_{\substack{m,n\in Z\\ m>0\\ n\geq 0\\ m+n=2l}}{}' \left\{ p_{mn} \left[\cos(\frac{2\pi x}{a}m)\cos(\frac{2\pi y}{b}n) \right.\right. \\ & \qquad + \cos(\frac{2\pi x}{a}\frac{m+3n}{2})\cos(\frac{2\pi y}{b}\frac{m-n}{2}) \\ & \qquad \left. + \cos(\frac{2\pi x}{a}\frac{m-3n}{2})\cos(\frac{2\pi y}{b}\frac{m+n}{2}) \right] \\ & + q_{mn} \left[\sin(\frac{2\pi x}{a}m)\cos(\frac{2\pi y}{b}n) \right. \\ & \qquad + \sin(\frac{2\pi x}{a}\frac{m+3n}{2})\cos(\frac{2\pi y}{b}\frac{m-n}{2}) \\ & \qquad \left.\left. + \sin(\frac{2\pi x}{a}\frac{m-3n}{2})\cos(\frac{2\pi y}{b}\frac{m+n}{2}) \right] \right\}, \end{aligned}$$

where p_{mn} and q_{mn} are constants. The prime sign of $\sum'$ means that every pair of integer numbers (m,n) can appear in the arguments of sin and cos only once. In other

words, once m and n have values m_0 and n_0, they will not take any of the values $\frac{m_0+3n_0}{2}$, $\frac{m_0-n_0}{2}$, $\frac{m_0-3n_0}{2}$, and $\frac{m_0+n_0}{2}$. p_{mn} and q_{mn} are found by fitting the function f to a number of total energies obtained by DFT calculations. For more details of the derivation of this equation, see Appendix A.

4.3 Computational Details

As it was already mentioned, we apply the all-electron full-potential augmented planewave plus local-orbital (FP-APW+lo) method as implemented in the WIEN2k package [97]. Since the method is among the most accurate first principle methods, we selected it to provide a benchmark for further studies. In our work, the exchange-correlation effects are treated within the generalized gradient approximation (GGA) according to Perdew, Burke and Ernzerhof [102].

In *ab-initio* electronic-structure methods, there is a set of computational parameters (convergence parameters) which can affect the accuracy of calculation on one hand, and of course, the computational costs on the other hand. Therefore they should be selected carefully to have reasonable and accurate enough results and also to minimize the computational effort as much as possible. To achieve these two purposes, convergence tests are required before starting heavy simulations. The aim of this section is to explain the optimizations which are applied in this part of the work. However, for a quick reference, all computational parameters are summarized in Tab. 4.3.

Table 4.3: Cell dimensions together with convergence parameters as used in our calculations. In all cases, muffin-tin radii R_{MT} of 1.6 and 1.4 a.u. were chosen for Fe and C, respectively.

			Lattice parameters							
		lattice type	a [a.u.]	b [a.u.]	c [a.u.]	cell volume [a.u.^{3}]	$RK_{\max}$	$R_{\mathrm{MT}}^{\min}$	matrix size	k-mesh $k_x \times k_y \times k_z$
Bulk	Fe	fcc	4.613	4.613	4.613	69.42	9.00	2.0	125	$15 \times 15 \times 15$
	Fe_3C	hexag.	4.955	4.955	11.810	251.11	7.00	1.4	580	$15 \times 15 \times 5$
	Fe_4C	cubic	6.520	6.520	6.520	277.11	7.00	1.4	811	$15 \times 15 \times 15$
	$Fe_{24}C$	hexag.	9.351	9.351	22.905	1734.40	7.00	1.4	2604	$8 \times 8 \times 2$
γ-curve	Fe	hexag.	4.613	4.613	67.799	1249.46	8.00	1.6	2921	$11 \times 11 \times 1$
	Fe_3C	hexag.	4.955	4.955	70.860	1506.67	7.00	1.4	3377	$10 \times 10 \times 1$
	$Fe_{24}C$	hexag.	9.351	9.351	68.714	5203.46	6.50	1.4	9596	$4 \times 4 \times 1$

4.3.1 Number of k-points

The electron density is usually denoted by ρ and obtained from the equation

$$\rho(\mathbf{r}) = \sum_{n \in \mathrm{occ.}} \int_{\Omega} d\mathbf{k} |\psi_{n\mathbf{k}}(\mathbf{r})|^2, \tag{4.6}$$

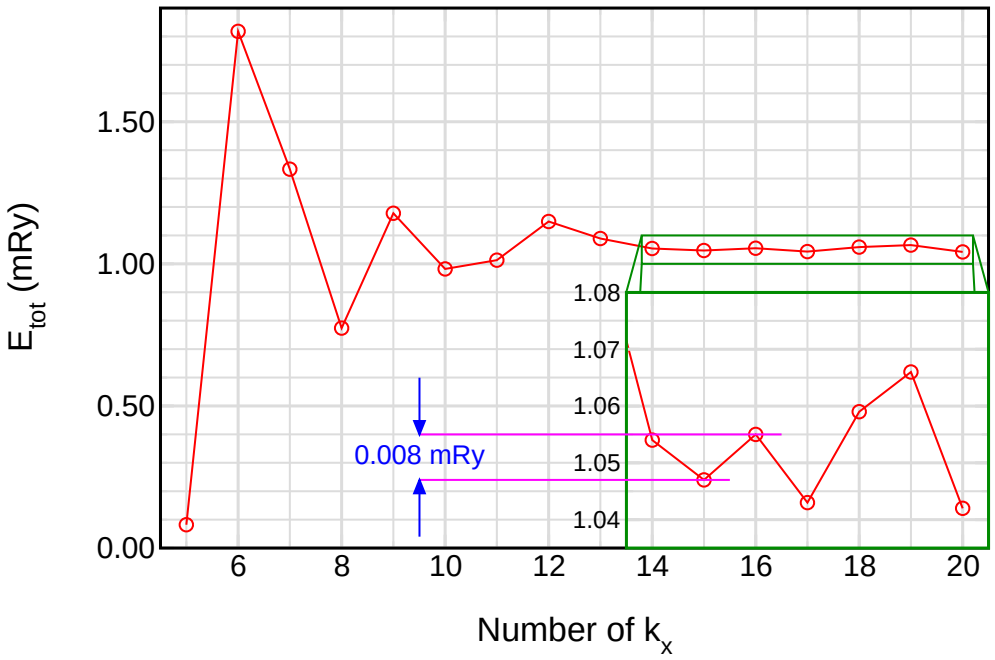

Figure 4.6: Total energy versus the number of the k-points for Fe_4C. A homogeneous k-mesh in all directions has been used. The inset depicts a zoom into a larger scale.

where $\mathbf{k}$ is the reciprocal space vector, ψ_n is the wavefunction corresponds to the nth orbital, Ω is the volume of the Brillouin zone (BZ), and the summations is performed over all the occupied states. The ψ_n are found from the Kohn-Sham equation

$$\mathcal{H}\psi_{n\mathbf{k}}(\mathbf{r}) = \varepsilon_{n\mathbf{k}}\psi_{n\mathbf{k}}(\mathbf{r}) \tag{4.7}$$

in which ε_n is the eigenvalue corresponding to the nth orbital. In practice, the numerical evaluation of the integral requires a proper k-mesh sampling in the BZ. The Kohn-Sham equation (Eq. 4.7) must be independently solved for every k-point in the mesh. Solving this equation is usually the most time-consuming part of the DFT calculations, so the computational cost of the calculations scales linearly with the total number of k-points. However, reducing the number of k-points in the mesh affects the accuracy of results. Therefore, a compromise between the accuracy and the number of k-points becomes important. This is usually done by finding the smallest mesh of k-points which can guarantee the required accuracy of results.

The required accuracy is usually defined corresponding to the goals of the calculations. Moreover, the system specifications (unit-cell shape and size, symmetry, atoms, ...) and calculation type (magnetic fashion, desired properties, ...) can influence the optimized k-mesh. We perform some tests for Fe_4C in order to find an optimum k-mesh for the bulk calculations. We evaluate the dependence of the total energy on the number of k-points as plotted in Fig. 4.6. For this cubic system, a k-mesh of $15 \times 15 \times 15$ guaranties the required accuracy. For other concentrations, the commensurate k-mesh is selected by comparing the unit-cell shape and size to those of Fe_4C.

4.3.2 Number of Basis Functions

The Kohn-Sham equation (Eq. 4.7) is a differential eigenvalue equation which can numerically be solved by using the variational principle. In this approach, the wavefunction is expanded into a proper basis set, and the solution is equal to finding the expansion coefficients so that the comprised wavefunction minimizes the total energy of system. In the LAPW method, the unit-cell is divided into non-overlapping atomic spheres centered at the atomic sites (muffin-tin spheres), and the interstitial region. Different basis sets are then employed for these two regions in order to expand the wavefunction. In the muffin-tin spheres a linear combination of atomic orbitals is applied as the basis sets, while in the interstitial region planewaves are used. A planewave basis is defined as

$$\phi_{\mathbf{k}_n} \propto e^{i\mathbf{k}_n.\mathbf{r}}, \tag{4.8}$$

where $\mathbf{k}_n = \mathbf{k} + \mathbf{K}_n$; $\mathbf{K}_n$ are the reciprocal lattice vectors and $\mathbf{k}$ is the wave vector inside the first BZ. A trial wavefunction in the interstitial region is expanded into this basis set according to the linear variation method,

$$\psi_{\mathbf{k}} = \sum_n c_n \phi_{\mathbf{k}_n}, \tag{4.9}$$

and the coefficients c_n are determined by the Rayleigh-Ritz variational principle. Technically, the expansion must be truncated at a certain $\mathbf{k}_{n_{\max}} = \mathbf{k} + \mathbf{K}_{n_{\max}}$. A bigger basis set (with higher number of terms) produces more accurate results at the cost of extra computational resources. Therefore selecting a reasonable upper bound for the expansion to keep a compromise between the accuracy and efficiency becomes important. In the WIEN2k package, this upper bound is controlled by the cutoff parameter $R_{\mathrm{mt}}K_{\max}$, where R_{mt} is the smallest atomic-sphere radius in the unit-cell and $K_{\max}$ is the magnitude of the largest $\mathbf{K}$ vector in the expansion.

The applied optimization method is explained in the following:

- **Bulk:** The lattice parameter and the bulk modulus are calculated for Fe_4C bulk using different values of $RK_{\max}$. The results are shown in Fig. 4.7. Any $RK_{\max}$ larger than or equal to 7.00 gives required accuracy for both desired parameters (see Table 4.3).

- **Slab, Fe_3C:** For this structure, the k-mesh and $RK_{\max}$ are optimized simultaneously. Some points on the γ-curve are calculated using a k-mesh of $10 \times 10 \times 1$ and $RK_{\max} = 7.0$. The calculations are repeated using a $15 \times 15 \times 1$ k-mesh and $RK_{\max} = 8.0$. Since no significant difference in the γ-curve is observed the smaller values are selected (see Fig. 4.8 and also Table 4.3).

- **Slab, $Fe_{24}C$:** For this concentration which has larger unit-cell, the effect of $RK_{\max}$ on the atomic forces in the slab is investigated. The results are shown in Fig. 4.9 (see also Table 4.3). Here $RK_{\max} = 6.5$ leads to reasonable results.

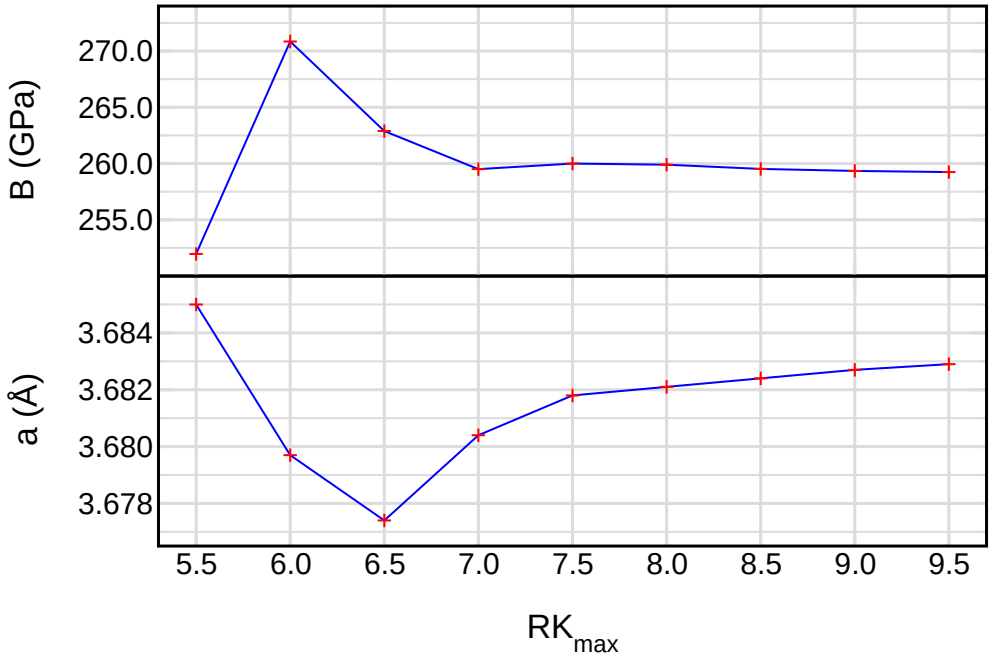

Figure 4.7: The dependence of the Lattice parameter, a, and bulk modulus, B, of Fe_4C on the values of $RK_{\max}$. Here $RK_{\max} = 7.0$ is enough for required accuracy.

4.3.3 Number of Layers in Slab

In order to evaluate the γ-curve for an fcc structure, two halves of the perfect crystal must be shifted along the $\{111\}$ plane. Technically, this can be managed by constructing a supercell including two or more slabs of perfect bulk and possibly a vacuum region, where every slab is displaced along the $\{111\}$ plane with respect to its neighbors. While using slabs with small number of atomic layers, L, are computationally favored, for keeping the accuracy of the results, L must be big enough so that the layer in the center of slab would feel an environment quite similar to that of the perfect bulk. A compromise between accuracy and performance can be found by investigating the influence of the number of layers on the γ-curve. Some points on the γ-curve are calculated using slabs with different number of layers, *i.e.*, $L = 3, 6, 9, 12$, as shown in Fig. 4.10. Since no significant change is found in the results going from $L = 6$ to 9 or 12, we select $L = 6$.

4.4 Results

4.4.1 The γ-curve of Fe

For non-magnetic pure iron at 0 K, DFT predicts the hcp phase to be energetically more stable than fcc [103]. Therefore, an fcc structure exhibiting an ISF is energetically more favorable than a perfect fcc structure since the $\cdots ABCAB|ABC\cdots$ stacking

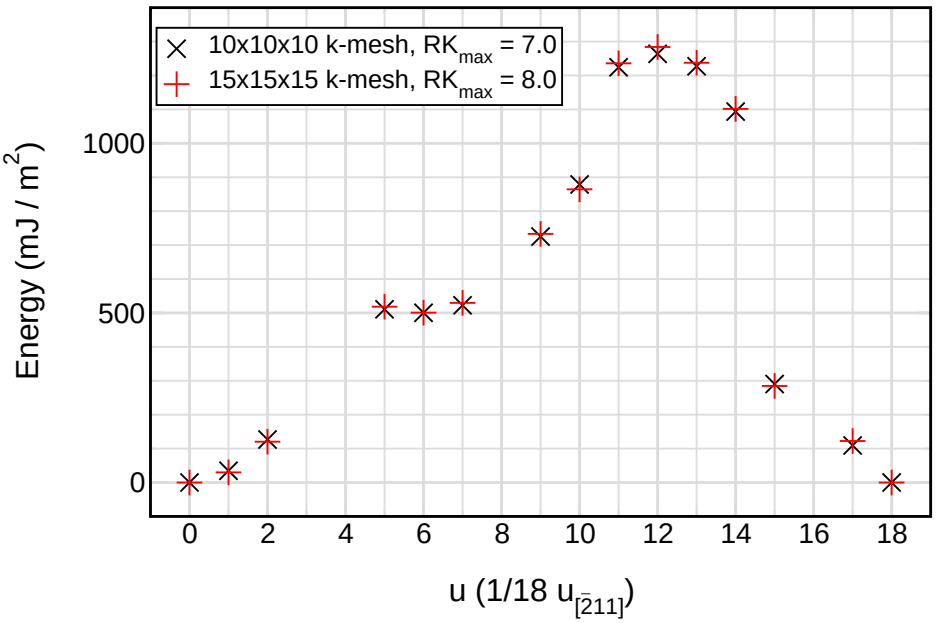

Figure 4.8: γ-curve in Fe_3C for two different sets of k-mesh and $RK_{\max}$.

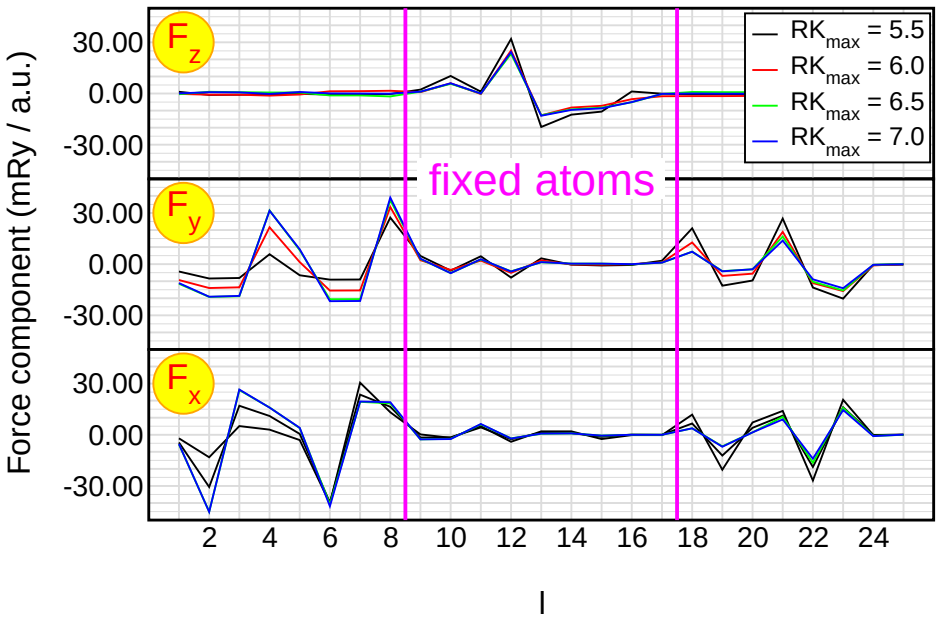

Figure 4.9: The dependence of the atomic forces on the value of $RK_{\max}$ for the $Fe_{24}C$ slab. l denotes the index of non-equivalent atoms in the unit-cell. The atoms in the middle layers (*i.e.* far away from the SF) are not allowed to relax. The results for $RK_{\max} = 6.50$ (green) and $RK_{\max} = 7.00$ (blue) are almost the same.

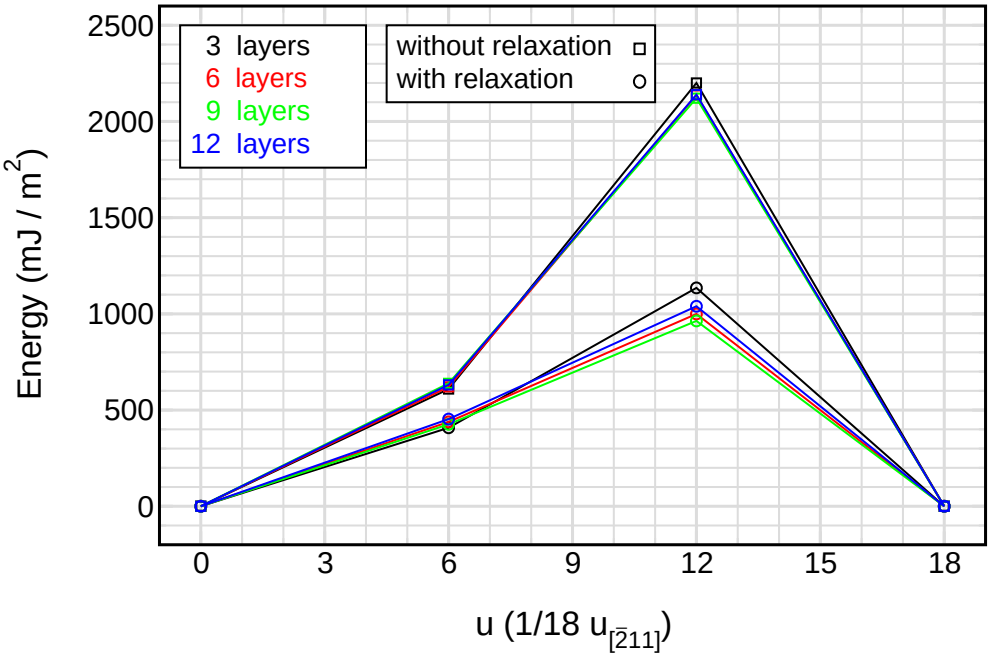

Figure 4.10: The dependence of the γ-curve on the number of atomic layers, l, between two consecutive SFs.

sequence of the former resembles an hcp-like stacking ($ABAB$) which appears close to the fault plane. This is reflected in our results which produce negative values of the γ-curve around $u = \frac{6}{18}u_{[\bar{2}11]}$ (see Fig. 4.11(c)). Our SFE of -450 mJ/m^2 is in good agreement with the work of Abbasi and coworkers [7], who found values between -452 and -464 mJ/m^2 for different unit-cell choices. The first peak in the curve, *i.e.*, at $u \approx \frac{3}{18}u_{[\bar{2}11]}$, describes the energy barrier which must be overcome in order to create an ISF. The second peak at $u = \frac{12}{18}u_{[\bar{2}11]}$ corresponds to a configuration with an $\cdots ABCAB|BCAB\cdots$ stacking sequence, which strongly violates the close-packing and, thus, is energetically very unfavorable. To preserve the close-packed stacking, the displacement can transform to an *extrinsic* SF by shearing one layer with respect to the entire crystal [35].

4.4.2 The γ-surface of $Fe_{24}C$

The supercell of $Fe_{24}C$ along the $[\bar{2}11]$ direction is twice as long as that of Fe and Fe_3C (see Fig. 1.6(a)). Hence, differences in the γ-curve between the first and the second half of this periodicity may arise due to the presence of carbon. However, when analyzing the γ-curve along the full doubled unit-cell, our calculations show that the second half of the curve, *i.e.*, $u_{[\bar{2}11]} < u < 2u_{[\bar{2}11]}$, is only slightly different than its first half, *i.e.*, $0 < u < u_{[\bar{2}11]}$, particularly when carbon is not placed in the fault plane. For this reason we present only the first half of the γ-curve here. This has the advantage that the horizontal axes in all presented γ-curves are of the same length and scale.

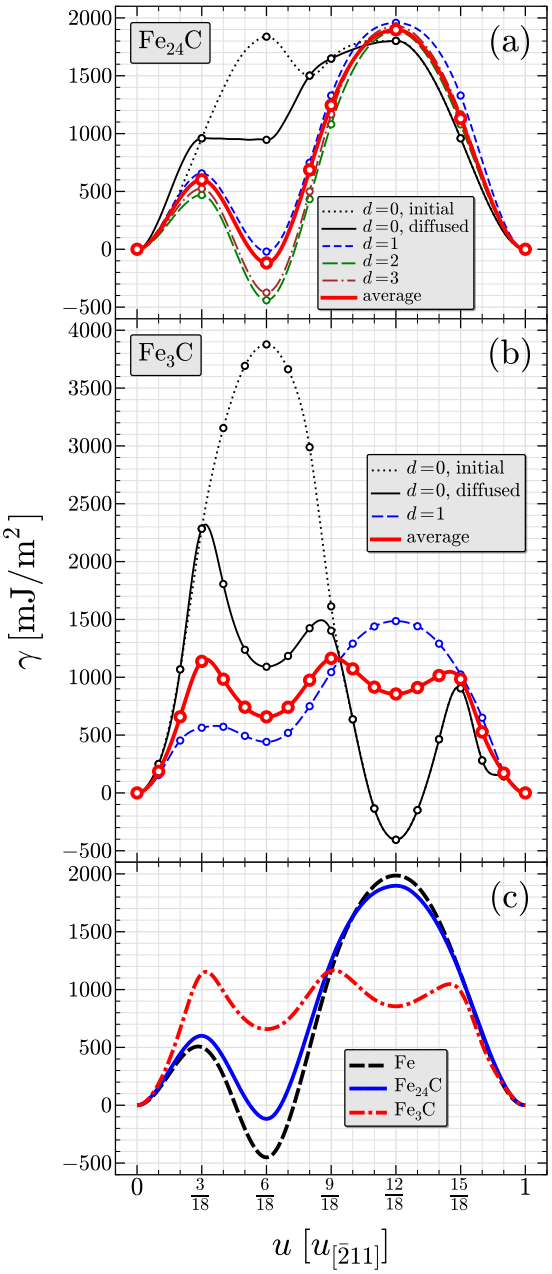

Figure 4.11: (a) The γ-curve for different positions of carbon with respect to the fault plane and their average, all calculated for $Fe_{24}C$. (b) The same for Fe_3C. (c) Comparison of the averages with pure Fe.

In Fig. 4.11(a), we present the γ-curves for carbon atoms positioned at various octahedral vacancies, corresponding to distances from the fault plane $0 \leq d \leq 3$. The results for $d = 0$ (dashed black curve) yield a very large energy for $u = \frac{6}{18} u_{[\bar{2}11]}$ since

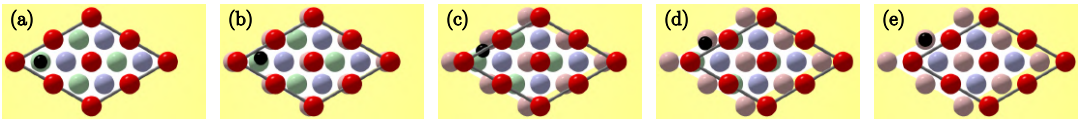

Figure 4.12: Carbon diffusion in $Fe_{24}C$ along the {111} plane. Spheres with pale and deep colors denote atomic layers belonging to fixed and shifted crystal halves, respectively. When a carbon atom is located in the SF plane, shifting the atomic layers requires an iron atom to pass on top of the carbon. The resulting configuration is highly unstable, thus the carbon diffuses to a new vacancy, which has just been created due to the shift.

this point corresponds to an unfavorable configuration in which an iron atom sits on top of the interstitial carbon. The creation of the SF, on the other hand, leads to new octahedral vacancies, which can be occupied by small interstitial atoms like carbon (see Fig. 4.12). Thus, the diffusion of carbon into this new interstitial site at the fault plane decreases the energy considerably, as indicated by the solid black curve. We further observe that the second peak in the curve with $d = 0$, is somewhat lower than the corresponding peak in the other ones. This can be explained by considering the fact that this peak is due to repulsion between iron atoms in two consecutive atomic layers, which is reduced when the distance between iron layers is increased through the presence of carbon. Focusing on the d-dependence at $u = \frac{6}{18}u_{[\bar{2}11]}$, *i.e.*, the ISF, we observe a monotonic behavior when increasing the carbon distance from $d = 0$ to $d = 2$, so that the curve corresponding to $d = 2$ is similar to the γ-curve for pure iron. However, the curve for $d = 3$ breaks this monotonicity which was assigned to Friedel-like oscillations [7]. Such oscillations appear in the charge density when an impurity is doped in a cloud of electrical charges. Here, the cloud is the body of the metal, and the impurity is the carbon atom. In order to visualize these oscillations, we calculate the charge densities for three supercells, including iron, carbon, and iron–carbon systems. The changes in the charge density is found by subtracting the charge densities of iron and carbon systems from the charge density of the iron–carbon system. These differences are presented in Figs. 4.13 and 4.14, for the two mentioned structures, *i.e.*, $d = 2$ and $d = 3$, respectively. The dependence of the SFE on the distance of the carbon atom from the fault plane is summarized in Fig. 4.15. It demonstrates that, the closer the carbon atom is positioned with respect to the fault plane, the higher is its influence on the SFE.

As explained in Sec. 4.2.3, we are interested in the γ-curve for a homogeneous carbon distribution. Therefore, we have to average over the results for various carbon positions characterized by their distances d from the fault plane in an appropriate manner. The $Fe_{24}C$ supercell, which has been utilized in this work, contains six types of interstitial octahedral sites, *i.e.*, $0 \leq d \leq 5$, while the γ-curve is calculated explicitly only for four sites with d up to 3. The effect of the other two layers, *i.e.*, $d = 4, 5$, on the γ-curve is taken into account by approximating their contribution by the mean value of the curves for $d = 2$ and $d = 3$. Using this mean value, we simulate the environment far from the fault plane, smearing out the above mentioned oscillations. In short, using $\gamma_4 = \gamma_5 = (\gamma_2 + \gamma_3)/2$, the general behavior of the γ-curve for $Fe_{24}C$ is found from the

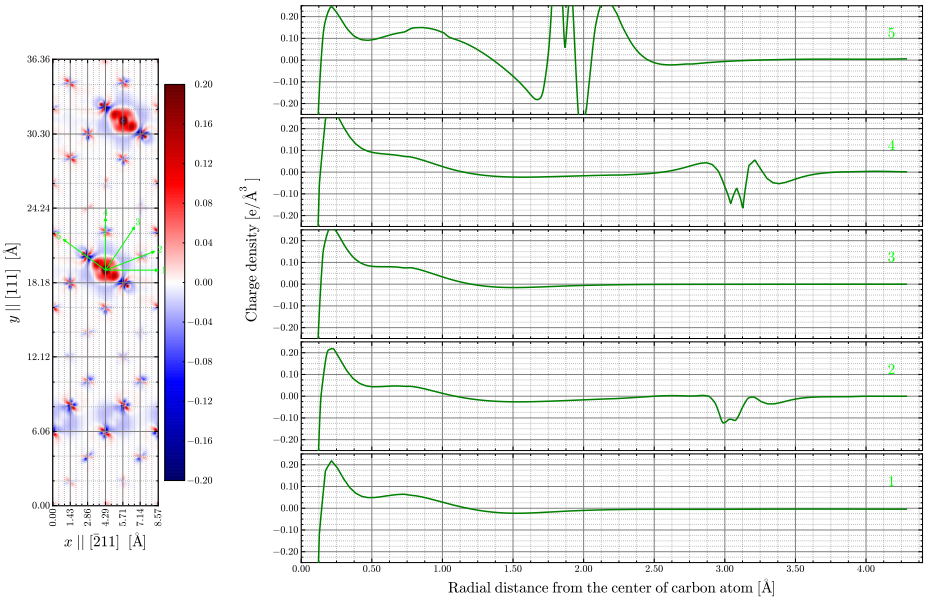

Figure 4.13: The difference in the charge density due to doping a carbon atom in $d = 2$ positions.

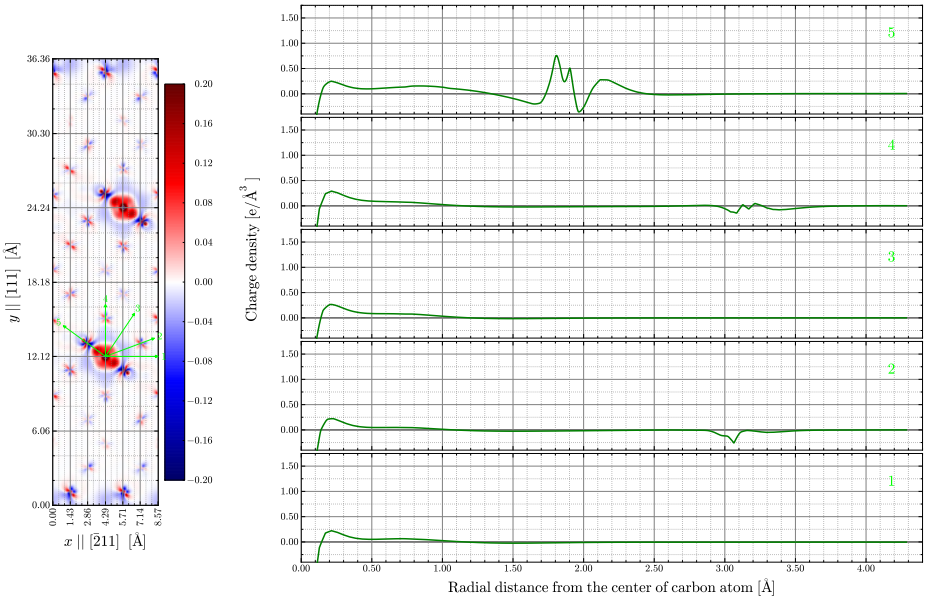

Figure 4.14: The difference in the charge density due to doping a carbon atom in $d = 3$ positions.

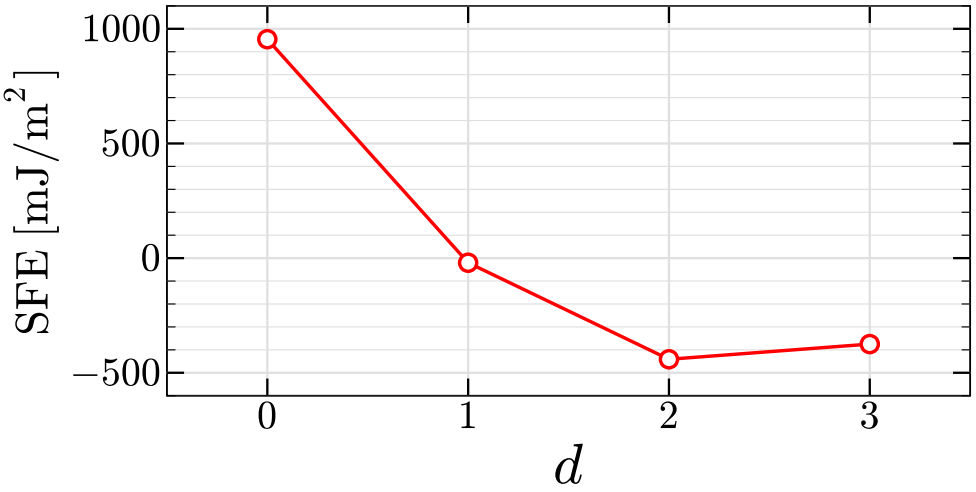

Figure 4.15: Dependence of the SFE on the distance of carbon from the fault plane for $Fe_{24}C$. For definition of d, see Sec. 4.2.3.

following expression

$$\gamma_{\text{av}}^{\text{Fe}_{24}\text{C}_1} = \frac{\gamma_0 + \gamma_1 + 2(\gamma_2 + \gamma_3)}{6}. \tag{4.10}$$

Using the approach described in Sec. 4.2.2, we can reconstruct the full two-dimensional γ-surface by making use of the symmetry properties of the crystal. It is presented in Fig. 4.16 for a rectangular area within the {111}-plane.

4.4.3 The γ-curve of Fe_3C

Fe_3C, or iron carbide, is a chemical compound of iron and 6.67 w% of carbon. At low temperatures, it is found in an orthorhombic crystal structure, known as cementite. It contains two kinds of vacancies, with octahedral and prismatic environment. A prismatic vacancy is formed by six iron atoms which are located at the vertices of a triangular prism. DFT calculations show that carbon prefers to occupy the prismatic vacancy rather than the octahedral one [46].

As we are interested in the austenitic phase, our approach to calculate the γ-curve for Fe_3C is, like the case of $Fe_{24}C$, based on an fcc structure where carbon occupies octahedral sites. When introducing a staking fault, two possible interstitial carbon sites must be distinguished which we characterize by the distance from the fault plane as $d = 0$ and $d = 1$. For $d = 0$, we calculate a value of 3877 mJ/m^2 at $u = \frac{6}{18}u_{[\bar{2}11]}$, as shown in Fig. 4.11(b). Diffusion of interstitial carbon along the {111}-plane into another possible interstitial site decreases this value to 1091 mJ/m^2. In contrast to all other curves, the case of $d = 0$ at $u = \frac{12}{18}u_{[\bar{2}11]}$ has a deep minimum instead of a high maximum. The reason is that in the corresponding configuration, $\cdots ABCAB|BCAB\cdots$, iron atoms around the SF are all located at vertices of triangular prisms with bases parallel to the

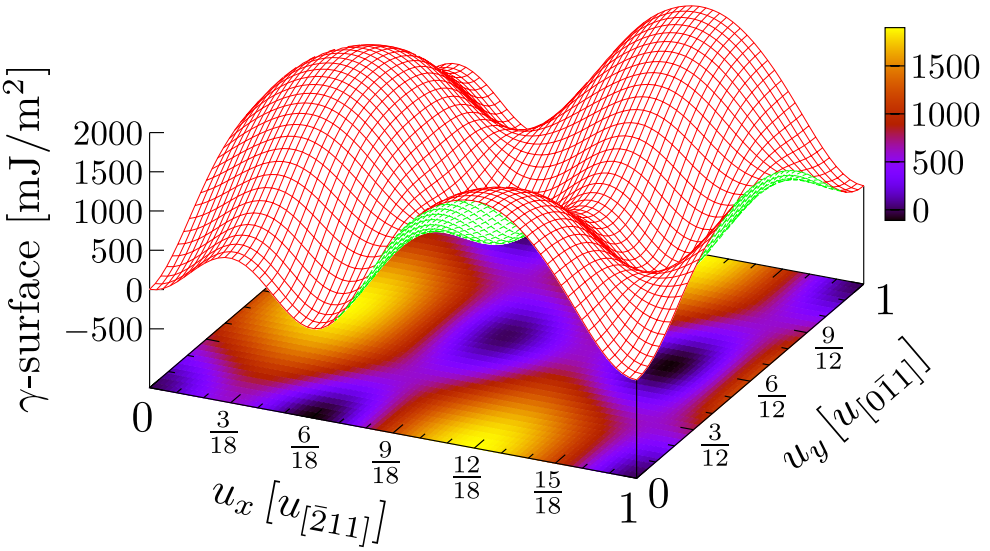

Figure 4.16: The γ-surface for $Fe_{24}C$.

fault plane. Every second prism contains a carbon atom in its center, providing six Fe-C bonds. Thus, the observed deep minimum results from the fact that for Fe_3C the cementite structure, described above, is more stable than austenite.

The average SFE for Fe_3C is presented by the red solid curve in Fig. 4.11(b). It shows a positive SFE, indicating that for this concentration the fcc structure is more stable than the hcp structure.

4.5 Discussion

In Fig. 4.17, our results about the influence of carbon on the SFE in fcc iron are summarized and confronted with available experimental and other theoretical results. As already mentioned in Sec. 4.1, experimental data are controversial: While a common behavior is that the SFE increases with carbon concentration, there is a large spread in the magnitude of the effect. Our calculations show that the SFE increases from -450 mJ/m^2 for pure iron to -116 mJ/m^2 for $Fe_{24}C$ with 0.89 w% of carbon. Thus, for carbon concentrations between 0 and 0.89 w%, the SFE dependence on the carbon concentration can be approximated by 376 mJ/m^2 per weight percent of carbon. This value is in good agreement with recently published results by Abbasi *et al.* [7] and also compares well with experiments by Schramm and Reed [4]. Our results for Fe_3C, *i.e.*, in the limit of very large carbon concentrations, show that the dependence of the SFE on the carbon concentration levels off at large carbon content. Although our calculations have been performed for zero Kelvin, we expect the fcc phase to become stable for carbonic steels with about 2 w% of carbon.

The barrier height at $u \approx \frac{3}{18} u_{[\bar{2}11]}$ increases with the carbon content. In contrast, at $u = \frac{12}{18} u_{[\bar{2}11]}$ the curves for $Fe_{24}C$ and Fe_3C show different behavior. There are two

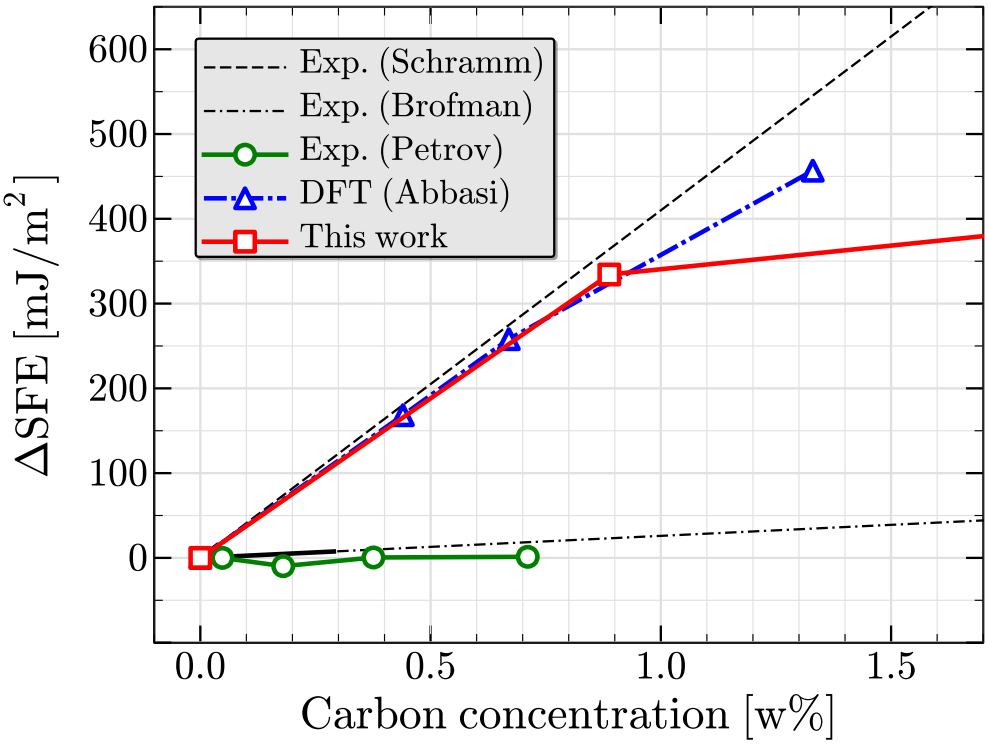

Figure 4.17: Carbon-induced change in the intrinsic SFE, ΔSFE, as a function of carbon concentration. Note that the values are normalized to the value of the intrinsic SFE for pure iron. Our calculations are compared to experimental [4, 5, 6] and the DFT [7] results.

competing phenomena affecting the total energy at this point: the distance between iron layers and the presence of a carbon at a prismatic site. For all values of d, the small inter-layer distance around the fault plane increases the total energy. Since the increase in cell volume per iron atom upon adding carbon is 4.1 % and 20.6 % for $Fe_{24}C$ and Fe_3C, respectively (see Tab. 4.3), $Fe_{24}C$ is more affected than Fe_3C. Occupation of prismatic sites by carbon decreases the energy. The possibility of occupying such site, which only occurs for $d = 0$, is $\frac{1}{12}$ and $\frac{1}{6}$ for $Fe_{24}C$ and Fe_3C, respectively. This confirms its more significant influence on the γ-curve of Fe_3C. As a result of these counteracting effects, we observe a high maximum for $Fe_{24}C$ and a local minimum for Fe_3C at $u = \frac{12}{18} u_{[\bar{2}11]}$.

5

Fe–Cr–Ni Through the EMTO Method

5.1 Introduction

Stainless steels, their classifications, and their properties were partially discussed in Chap. 2. The importance of this class of steels in many applications arises a great motivation for finding efficient producing and shaping methods. Shaping steels under shear stresses involves plastic deformations, a process where the SFE has a well-known influence [36, 37, 38]. The SFE in turn depends on temperature and on the composition of alloy (see Appendix B for experimental reports, and [8, 104, 105] for theoretical references), making it particularly important when considering the thermal treatments and shaping of the metal at high temperatures.

In this work, we study the influence of temperature on the SFE of a ternary alloy with $Fe_{0.716}Cr_{0.200}Ni_{0.084}$ composition. In order to do so, using DFT and the EMTO method described in Sec. 3.3, the SFE is calculated in the temperature range of 273–1273 K (0–1000 °C). The chromium and nickel contents in this alloy are similar to those in the commercial product known as Böhler[1] A607. However, as shown in Tab. 5.1, this commercial alloy contains small amounts of additional elements which are not taken into account in our simplified calculations. For brevity, in this document, the code A607 is used in order to point to the simulated compound, while the corresponding alloy with real composition is referred by its full name, *Böhler A607* (see Tab. 5.1).

Our simulations are performed for random alloy in paramagnetic austenitic phase at the mentioned temperature range. As it was discussed with more details in Sec. 2.3, at room temperature, stainless steels might be found in a variety of stable or metastable phases, depend on their composition and heat treatment. However, most of stainless steels, including 18/8 class containing around 18wt.% chromium and 8wt.% nickel, are designed to maintain their paramagnetic fcc phase (γ-austenite) in their service condition. As a member of this class, A607 is also known as an austenitic stainless steel,

[1] *Böhler Special Steels*, A-8605 Kapfenberg, Austria

whose fcc structure has been proven with the X-ray diffraction (XRD) measurements on the Böhler A607 alloy.

Briefly speaking, in this work, we use the axial next-nearest-neighbor Ising (ANNNI) model [98, 99] in order to expand the SFE in terms of the free energies of bulk with fcc, hcp, and double-hcp (dhcp) crystal structures (see Fig. 5.1 and Sec. 5.2). These free energies are dependent on the lattice parameter which is obtained from experimental thermal expansion data measured using the XRD technique, and on the thermal excitation of the local magnetic moments which is evaluated by running a Monte-Carlo simulation on the system energy maps calculated using the DFT techniques (see Sec. 5.4.2. The DFT calculations are performed using the exact muffin-tin orbitals (EMTO) method [106] and the locally self-consistent Green's function (LSGF) methods [107], where random alloy and paramagnetic state are modeled using the coherent potential approximation (CPA) [93] and the disordered local moment (DLM) [94], respectively.

Table 5.1: The atomic and mass concentrations of the commercial alloy, Böhler A607, compared to their simplified equivalents used in our simulations.

alloy	unit	Cr	Ni	Mn	Mo	C	Fe
Böhler A607	wt. %	18.00	9.00	≤2.00	—	≤0.03	70.17
	at. %	19.97	8.47	≤2.01	—	≤0.14	69.41
Simulated A607	wt. %	18.80	8.91	—	—	—	72.29
	at. %	20.00	8.40	—	—	—	71.60

5.2 Methodology

Stacking faults are irregularities in the stacking of layers of atoms in a crystalline solid, and hence change the total energy of the system. These changes, compared to the crystal total energy, are generally very small, presented in the unit of mJ/m^2. While the SFE can be accurately and explicitly calculated using the first-principles techniques [7, 95, 108], these methods are quite cumbersome, since they require large supercells. A more efficient solution, which is going to be explained here, is to expand the SFE in terms of the free energies of bulk unit-cells with fcc, hcp, and dhcp structures (see Fig. 5.1).

In the fcc lattice, an ISF, which corresponds to the removing of one atomic layer from the perfect $ABCABCABC\cdots$ structure, may be represented as the arrangement of atomic layers with the repeat unit of $ABCBC(ABC)^n$ $(n = 0, 1, 2, \cdots)$, consisting of N layers $(N = 5, 8, 11, 14, \cdots)$ in the limit $N \to \infty$. We can now apply the ANNNI model to this representation, where the analogue of the Ising spin S_i for layer i, has a

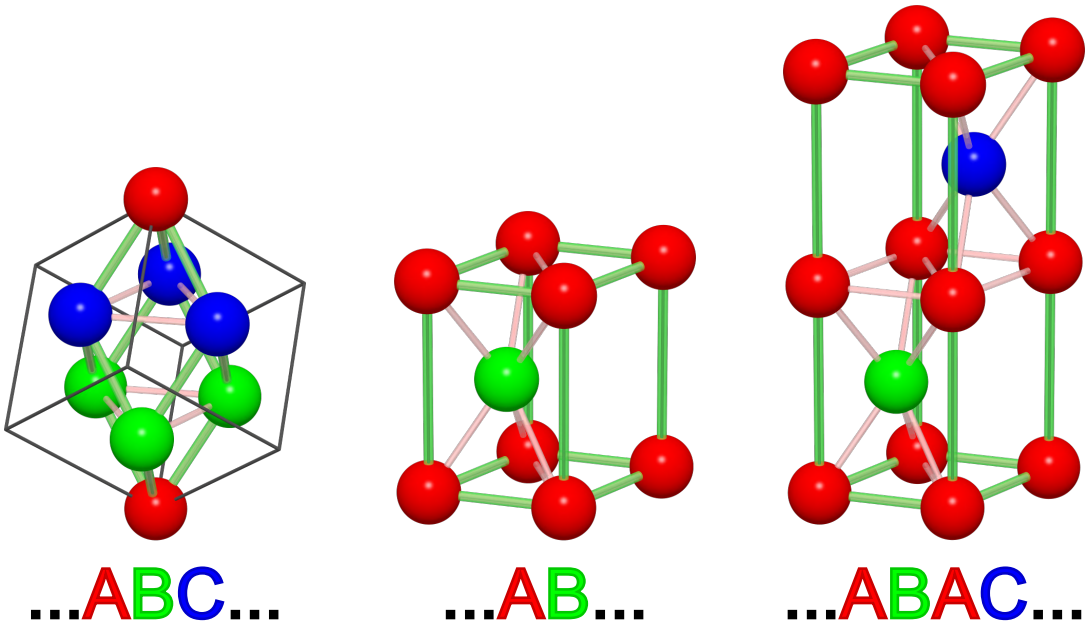

(a) (b) (c)

Figure 5.1: Primitive cells of three crystal phases used in the ANNNI model. Atoms are painted corresponding to their stacking position along the [111] direction. (a) depicts the primitive cell of the fcc structure with only one atomic site. The cubic cell is shown for a better imagination of the lattice. (b) shows the primitive cell of the hcp structure containing two non-equivalent atoms (two atomic sites). (c) represents the primitive cell of the dhcp structure with four non-equivalent atoms (four atomic sites).

value $+1$ (-1) if the next layer with index $i+1$ does (not) conform the ideal stacking sequence. This idea results in the following expression for the Helmholtz free energy of any arbitrary stacking sequence [99]:

$$\mathcal{F} = \mathcal{F}_0 - J_1 \sum_i S_i S_{i+1} - J_2 \sum_i S_i S_{i+2} - J_3 \sum_i S_i S_{i+3} - \cdots , \tag{5.1}$$

where $\mathcal{F}_0$ is the energy contribution disregarding all interactions between layers, and thus is the same for any arbitrary stacking sequence. The parameters $J_n (n = 1, 2, 3, \cdots)$ may be interpreted as interaction energies between two layers that are nearest neighbors (J_1), next-nearest neighbors (J_2), ... It is expected that the magnitude of J_n decreases for increasing n. In the ANNNI model, by definition, all J_n with $n \geq 3$ are neglected [98].

In the limit of large N, the above equation suggests the following expressions for

the Helmholtz free energies of the stacking sequences with different repeat units [99]:

$$\begin{array}{lllllll} ABC & \mathcal{F}^{\rm fcc} = J_0 & -J_1 & -J_2 & -J_3 & -J_4 - \cdots, \\ AB & \mathcal{F}^{\rm hcp} = J_0 & +J_1 & -J_2 & +J_3 & -J_4 + \cdots, \\ ABAC & \mathcal{F}^{\rm dhcp} = J_0 & & +J_2 & & -J_4 + \cdots, \\ ABCBC(ABC)^n & \mathcal{F}^{\rm ISF} = J_0 & -\frac{N-4}{N}J_1 & -\frac{N-4}{N}J_2 & -\frac{N-4}{N}J_3 & -\frac{N-4}{N}J_4 - \cdots, \end{array} \tag{5.2}$$

where the energies are normalized to a unit cell in one layer, and J_0 is the energy per unit cell in one layer if the interactions between layers are disregarded. Using the first three equations, J_0 is found as

$$J_0 = \frac{\mathcal{F}^{\rm fcc} + \mathcal{F}^{\rm hcp} + 2\mathcal{F}^{\rm dhcp}}{4} + O(J_4). \tag{5.3}$$

The energy difference between a structure with an ISF and the fcc bulk structure, both of the same thickness equal to N layers, is defined as

$$\begin{aligned} \lim_{N\to\infty} N\{\mathcal{F}^{\rm ISF} - \mathcal{F}^{\rm fcc}\} &= 4\{J_1 + J_2 + J_3 + J_4 + \cdots\} \\ &= -4\{\mathcal{F}^{\rm fcc} - J_0\} \\ &= \mathcal{F}^{\rm hcp} + 2\mathcal{F}^{\rm dhcp} - 3\mathcal{F}^{\rm fcc} + O(J_4). \end{aligned} \tag{5.4}$$

Since the number of atomic sites per volume is equal in bulks with ideal fcc, hcp, or dhcp structures (see Fig. 5.1), we can rewrite the above equation in the terms of the Helmholtz free energies per atomic site, F. Finally, by neglecting all J_n with $n \geq 4$ according to the definition of ANNNI model, and by considering the dependence of the Helmholtz free energies on temperature, the SFE is expressed as

$$\mathrm{SFE}(T) \approx \frac{F^{\rm hcp}(T) + 2F^{\rm dhcp}(T) - 3F^{\rm fcc}(T)}{A}, \tag{5.5}$$

where A is the area in a close-packed layer occupied by a single atomic site, and its value can simply be obtained in terms of the fcc lattice parameter: $A = \frac{\sqrt{3}}{4}a_{\rm fcc}^2$.

The Helmholtz free energy is defined as

$$F(T) = E(T) - TS(T), \tag{5.6}$$

where E and S are the total energy and entropy per site, respectively. The entropy is calculated by accounting all available excitations which may occur in the microscopic configuration (microstate) of the system. Particularly, in an alloy, as a crystalline solid with nonzero density of states at its Fermi level, microstate might change due to different excitations: the *configurational excitations*, considered as the interchange of positions between atoms of different types, the *vibrational excitations*, defined as small displacements of atoms around their lattice sites, the *magnetic excitations*, which are fluctuations in the size or the orientation of the atomic magnetic moments, and, finally, the *electronic excitations*, which are changes in the electronic structure of the metal as electrons are excited to levels higher then the Fermi level. Depends on the diffusion

rate, for very fast diffusions in solids, the configurational excitations occur in the time scale of 10^{-5} or 10^{-4} seconds, while the the atomic vibrations are in the time scales of 10^{-11} 10^{-10} seconds. The magnetic excitations are faster then the vibrations, and the electronic excitations are the fastest in the list. The large differences between these time scales allow to apply a course-graining method in order to calculate the excitations independently, which finally results in their separate contributions to the total entropy of the crystal [109]:

$$S = S_{\text{conf.}} + S_{\text{mag.}} + S_{\text{el.}} + S_{\text{vib.}}, \tag{5.7}$$

where all terms are related to a single site in the lattice.

For the vibrational entropy, there are currently no available theoretical tools to determine it accurately in paramagnetic random alloys, and thus we do not include it in our calculations. However, considering its contribution to the free energy differences between the fcc and the hcp phases, *i.e.*, $\Delta F_{\text{vib.}} = F_{\text{vib.}}^{\text{hcp}} - F_{\text{vib.}}^{\text{fcc}}$, it is estimated that this simplification may introduce an error of 2 mJ/m^2 in the SFE [8], which is rather small.

Considering totally random alloys, the configurational entropy depends only on the chemical composition [110]:

$$S_{\text{conf.}} = -k_{\text{B}} \sum_{i \in \{\text{elements}\}} c_i \ln(c_i), \tag{5.8}$$

where c_i denotes the atomic concentration of element i. The assumption of the random distribution of all atoms on a sublattice is best in situations when (a) the temperature is very high, so the atoms are indeed randomly distributed on the sublattice; (b) the temperature is very low, and only a few antisite atoms are present [110]. For other situations, particularly when temperature is not very high or when chemical compositions of elements in an alloy are not very small, this assumption is not entirely correct, since atoms show certain preferences when interacting with their neighbors. In a solid solution, these atomic interactions can express the local tendency for preferences of like or unlike neighbor pairs, which is known as *short-range order* (SRO). The SRO might be better understood compared to the *long-range order* (LRO), a crystal character which precisely specifies the properties (the position and the type) of atoms in the entire lattice by knowing them at a single lattice point. This term might also be pointed as the chemical or the atomic SRO (LRO) for the sake of distinguishing from its analogue in magnetism, *i.e.* the magnetic SRO (LRO).

In an ordered alloy, the SRO can change with some independence of the LRO, resulting in changes in the configurational entropy. Particularly at high temperatures, where the LRO vanishes, considerable SRO exists, increasing its importance in the entropy calculations. Additional to the entropy, the total energy $E(T)$ also changes due to the SRO, resulting in further changes in the free energy. In order to take the SRO into account, some corrections to the CPA approximation and the configurational entropy equation, Eq. 5.8, are required. However, at the moment, the effect of the atomic short range order is neglected in our work by approximating the alloy as a fully random configuration of atoms. Such an assumption results in equal configurational

entropies for all phases with the same chemical compositions, canceling each other out in Eq. 5.5.

In a system of localized magnetic moments of the same size and completely disordered orientations, *i.e.*, the ideal paramagnetic state, the magnetic entropy is evaluated using the mean-field expression [111]

$$S_{\text{mag.}} = k_{\text{B}} \sum_{i \in \{\text{elements}\}} c_i \ln\big(m_i(T) + 1\big), \tag{5.9}$$

where $m_i(T)$ is the average (over time and space) local magnetic moments of element i, and is obtained using statistical approaches where the thermal excitations of magnetic moments are taken into account (see Sec. 5.4.2). Similar to the existence of the atomic SRO even at temperatures where the atomic LRO has already vanished, the magnetic SRO might exist in a paramagnetic state. However, its influence on the accuracy of the final results is not as large as that of the atomic SRO [citation].

The electronic entropy can be calculated using the Fermi-Dirac distribution for the occupation of valence states, as implemented in the Mermin functional [66, 112]. This approach is already available in the EMTO code, and we use it in order to calculate the electronic entropy. However, as we will present in Sec. 5.4.6.1, the influence of the electronic entropy on the final SFE is very small, and hence an be safely neglected.

The total energy is calculated using the DFT approach, where the system is considered in its ground state at 0 K. Hence, the temperature dependence of the total energy is taken into account via the lattice parameter, $a(T)$, and the average local magnetic moments, $m_i(T)$ (here $i \in \{\text{Fe, Cr, Ni}\}$):

$$E(T) = E[a(T), m_i(T)]. \tag{5.10}$$

The first principles evaluation of the lattice parameter as a function of temperature requires the calculation of vibrational excitations for the random alloy in the paramagnetic state. Such calculations are not straightforward, since no relevant computational tools are available yet. Despite these complexities in the theoretical approach, the lattice parameter can easily be measured at different temperatures. Thus, we obtain the temperature dependence of the lattice parameter using the XRD measurements of the thermal expansion of the alloy.

The thermal dependence of the local magnetic moments is difficult to be measured. However, considering the thermal excitation of the individual moments through statistical methods, it is possible to calculate the average magnetic moments at different temperatures. We will present this approach in Sec. 5.4.2.

As a summary of our methodology, the he necessary steps for evaluating the SFE can be listed as the following:

- **Magnetic moments calculations:** In this step, for every element in every phase, we calculate the average magnetic moments as a function of temperature (see Sec. 5.4.2 for details). The calculations are broken into two major parts:

1. **The DFT calculations:** In this part the dependence of the total energy of the system on the local magnetic moments of every element is obtained(see Sec. 5.4.2.1).

2. **The Monte-Carlo calculations:** A set of simulations with magnetic Hamiltonians are performed on the system energy maps calculated in part 1, and the temperature dependence of the average magnetic moments is found (see Sec. 5.4.2.2).

- **Constrained DFT calculations:** In this step, according to Eq. 5.10, for different temperatures, the experimental lattice parameter and the magnetic moments from the previous step are used in DFT calculations in order to find the total energy as a function of temperature. These calculations are called *constrained*, because all magnetic moments are fixed (see Sec. 5.4.3 for details).

- **Free energy evaluation:** Using the results of the previous steps, according to Eqs. 5.6 and 5.9, the Helmholtz free energy is evaluated for all phases at different temperatures by subtracting the magnetic entropy from the total energy. Finally, using these free energies in the ANNNI model gives the SFE as a function of temperature (see Sec. 5.4.3 for details).

5.3 Computational Details

In a simulation, the accuracy of the final results is influenced by two major choices: the physical model, and the computational method. The physical model, using available theories, tries to approximate the real interactions between the individual parts of a system. In order to get a correct physical description of the system, these approximations must be as sophisticated as possible. In other words, the more detailed interactions are considered in the model, the more accurate results can *potentially* be obtained. However, it is possible, specially when investigating the difference between properties of two systems, that the shortcomings of the applied physical model are hidden as the errors in calculations cancel each other out. Practically, when developing a physical model, very often, a compromise is necessary between the importance of the present interactions and the complexities of their accounting. In fact, by such a compromise, the physical model defines the limit of accuracy and the reliability of the final results. We discussed our physical model in the previous section.

Considering the chosen physical model to be sufficiently accurate, the computational method calculates the system properties in the frame of this model. Here also, by setting proper computational parameters, a compromise is achieved between the desired accuracy and the required numerical efforts. The subject of this section is to discuss the most important computational parameters we have in out simulations.

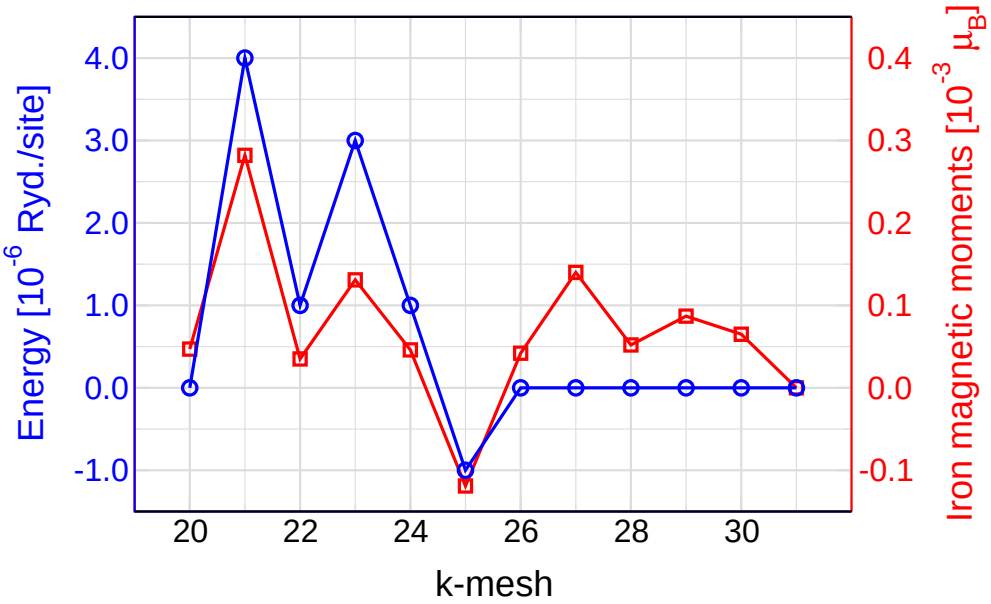

Figure 5.2: k-mesh optimization for the fcc structure of A607 alloy

5.3.1 Number of k-points

The SFE is usually expressed in the unit of mJ/m^2, and its value has been reported in the range of 10–50 for stainless steels with composition close to A607 (for a summary of experimental values, see Appendix B and Fig. 5.19). Considering the geometry of the {111} surface of an fcc structure, we find that

$$1\ \mathrm{mJ/m^2} = 1.98641346 \times 10^{-6} a_{\mathrm{fcc}}^2\ \mathrm{Ry/site}, \tag{5.11}$$

where a_{fcc} stands for the fcc lattice parameter in the unit of Angstrom (Å). Speaking about the The equation suggests that, in order to get the SFE with an accuracy of 1 mJ/m^2, the differences between the free energies of the three phases must be calculated with the accuracy of 10^{-6}Ry/site. Using the Eq. 5.9, it is found in a similar way that the local magnetic moments must be obtained with the accuracy of $10^{-3}\mu_{\mathrm{B}}$. The number of k-points is one of the parameters affecting the accuracy of results, and hence must be selected carefully. We calculate the total energy and the local magnetic moments for different k-meshes to obtain the smallest mesh which guaranties the desired accuracy. As presented in Fig. 5.2, for the A607 alloy with the fcc structure, a k-mesh of $31 \times 31 \times 31$ results in converged values for both energy and magnetic moments. Using these informations, the commensurate sets of k-meshes for hcp and dhcp are found $30 \times 30 \times 16$ and $30 \times 30 \times 8$, respectively.

5.3.2 Core-electrons Treatment

There are two possible treatments for core electrons, the *soft-core* approach versus the simplified *frozen-core* approximation. In the frozen-core approximation, the wave

Table 5.2: The electronic configuration of elements iron, chromium, and nickel, according to the default definitions in the EMTO code. n indicates the principle quantum number, and κ stands for the relativistic quantum number (see Tab. 5.3). For better readability, core states have been highlighted by gray background.

^{26}Fe: $1s^2$ $2s^2$ $2p^6$ $3s^2$ $3p^6$ $4s^2$ $3d^6$										
n	1	2	2	2	3	3	3	3	3	4
κ	−1	−1	1	−2	−1	1	−2	2	−3	−1
occupation	2	2	2	4	2	2	4	4	3	1

^{24}Cr: $1s^2$ $2s^2$ $2p^6$ $3s^2$ $3p^6$ $4s^1$ $3d^5$									
n	1	2	2	2	3	3	3	3	4
κ	−1	−1	1	−2	−1	1	−2	2	−1
occupation	2	2	2	4	2	2	4	4	2

^{28}Ni: $1s^2$ $2s^2$ $2p^6$ $3s^2$ $3p^6$ $4s^2$ $3d^8$										
n	1	2	2	2	3	3	3	3	3	4
κ	−1	−1	1	−2	−1	1	−2	2	−3	−1
occupation	2	2	2	4	2	2	4	4	4	2

Table 5.3: The derivation of the relativistic quantum number and the maximum occupations of electronic states per spin. Indicating the *principle*, the *azimuthal*, and the *spin* quantum numbers respectively by n, $0 \leq l < n$ and $s = \pm 1/2$, the *orbital* and the *relativistic* quantum numbers are defined as $j = l + s/2$ and $\kappa = -s(j + 1/2)$, respectively [10].

orbital	l	$j = l + s/2$		$\kappa = -s(j + 1/2)$		max. occupation	
		$s = -1$	$s = +1$	$s = -1$	$s = +1$	$s = -1$	$s = +1$
s	0		1/2		−1		2
p	1	1/2	3/2	1	−2	2	4
d	2	3/2	5/2	2	−3	4	6
f	3	5/2	7/2	3	−4	6	8

functions of the core electrons are assumed not to be affected by different surrounding environments. Based on this assumptions, the lowest atomic orbitals are kept exactly as they are in isolated atoms, and are constrained to remain doubly-occupied by the inner-shell electrons. Unlike this, in the soft-core approximation, all electrons (including both core and valance electrons) are calculated through the self-consistent approach. Tab. 5.2 presents the electronic configurations of iron, chromium, and nickel atoms, where core states are indicated by gray background. Note that, these are the default values defined in the EMTO code we use in this work, and might be changed by user. In the table, electronic states are split according their *relativistic* quantum number, κ, which is derived using the *azimuthal* and *spin* quantum numbers, *i.e.* l and s respectively (see Tab. 5.3).

The frozen-core approach might speed up the calculation, but in the price of losing accuracy, as it approximates the core orbitals with atomic orbitals. This simplification affects the physical description of the system, as it neglects all changes which might appear in the core states. Moreover, it has already been reported that when atoms are brought together to form molecules or solids the change in the kinetic energy of the core electrons can be an order of magnitude larger than the change in total energy [113]. Generally, if no sufficient corrections are applied, it is recommended to avoid this approximation where an accuracy higher than 0.1 eV is desired [113]. We apply the soft-core approximation in order to get a better description of interactions between atoms in the alloy.

5.3.3 Screening Parameters

For every element in the system, a pair of screening parameters must be given: a_{scr} which is related to charge transfers in the system, and b_{scr} which is related to the electrostatic energy. The influence of b_{scr} is small compared to that of a_{scr} [citation], thus we investigate the effect of a_{scr} only. While in the new LSGF-EMTO method they are calculated self consistently, in the version of the EMTO code we use in this work they must be given as input parameters. Since it could be time-consuming to calculate them, we used values suggested by Prof. Andrei Ruban, the developer of the code.

As a convergence test, we calculate the influence of the screening parameters on the equilibrium volume and the magnetic moments of the A607 alloy in the fcc phase. The results of these tests are presented in Fig. 5.3. Our calculations show that scaling all screening parameters uniformly shifts the entire E-V curve along the energy axis, where a set of larger screenings results in the lower total energy, and vise versa. The equilibrium volume has reverse relation with the uniformly scaled screenings: it increases 0.06% for scaling factor of 0.7, and decreases 0.13% for scaling factor of 1.3. Such small changes might be considered as negligible. Moreover, the local magnetic moments presented in Fig. 5.3(b) show only small changes due to the uniform scaling of the screening parameters. Further investigations by calculating the same quantities for the hcp and dhcp phases, show that the total-energy shifts are equal for all three phases. As presented in Fig. 5.4, when evaluating the SFE, these changes cancel each other out, leaving the SFE unchanged.

The behavior of the E-V curve and the magnetic moments versus the non-uniform scaling of the screening parameters is presented in Fig. 5.5, where these two quantities are plotted for scaling factors of 0.8, 1.0, and 1.2. Similar to the case of the uniform scaling, the changes in the equilibrium volume are negligible. For the magnetic moments, although our results show an increase of up to 0.2 μ_B in the local magnetic moments of iron at smaller lattice volumes, changes at equilibrium volume are negligible. The interesting result which is found by analyzing the equilibrium energy E_0 is the fact that, despite to their concentrations, the total energy is mainly affected by the screening parameter of chromium, then nickel, and finally iron. This result is plotted in Fig. 5.6, where scaling factor are distinguished by different colors. The curly brackets and their labels in the figure indicate categories of calculations with the same screening for the specified atom type.

We can finally conclude that, as long as the screening parameters are not selected too far from their correct values, they are not affecting the accuracy of the SFE significantly. A set of screenings with less than ±10% errors might be consider accurate enough for the SFE calculations.

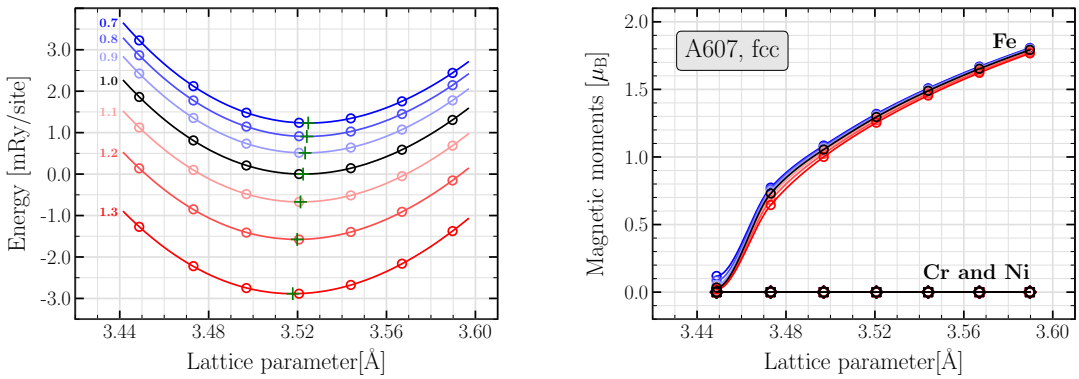

(a) (b)

Figure 5.3: For the fcc phase of A607 alloy, (a) and (b) show the effect of uniform scaling of all screening parameters on the E-V curve, and on the local magnetic moments, respectively.

5.4 Results

5.4.1 Volume Effects

In order to investigate the properties of bulk materials, we evaluate the dependence of the total energy and the local magnetic moments on the volume. We simulate random alloys in the paramagnetic state, where the chemical composition is set according to the mentioned A607 alloy. These simulations are repeated for the three phases which are present in the ANNNI model, *i.e.*, fcc, hcp, and dhcp (see Fig. 5.7(a)). By using the ideal c/a ratio for the hcp and dhcp phases, and the same lattice parameter a for

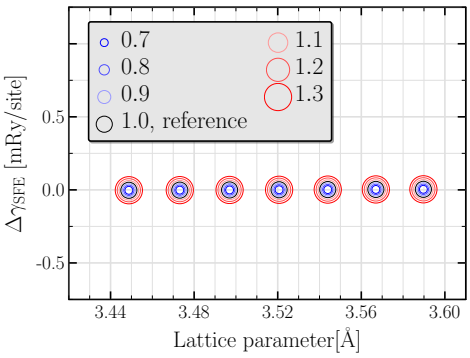

Figure 5.4: The influence of uniform scaling of the screening parameters on the SFE, calculated for A607 alloy.

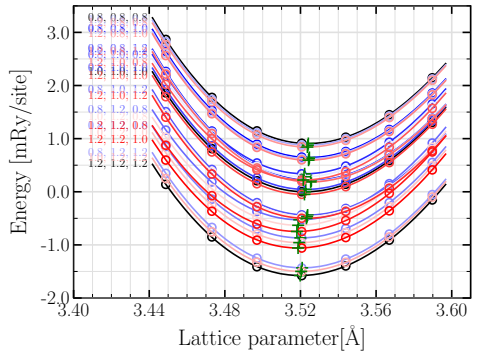

(a)

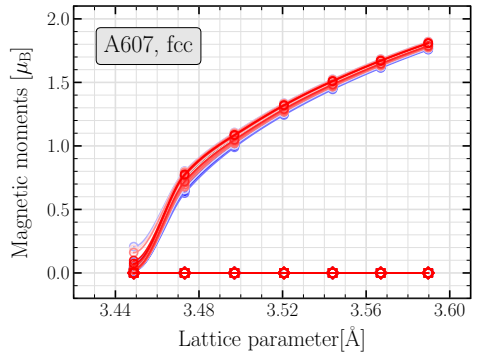

(b)

Figure 5.5: For the fcc phase of A607 alloy, (a) and (b) show the effect of non-uniform scaling of all screening parameters on the E-V curve, and on the local magnetic moments, respectively.

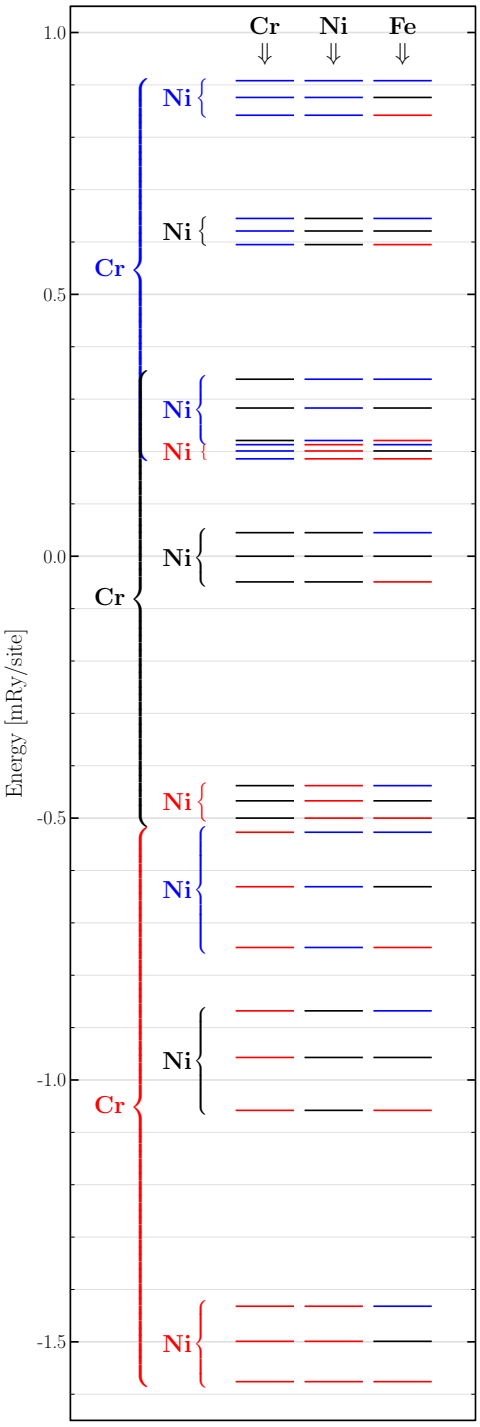

Figure 5.6: The effect of non-uniform scaling of the screening parameters on the total energy of fcc phase. Blue, black, and red lines depict the scaling factors of 0.8, 1.0, and 1.2, respectively.

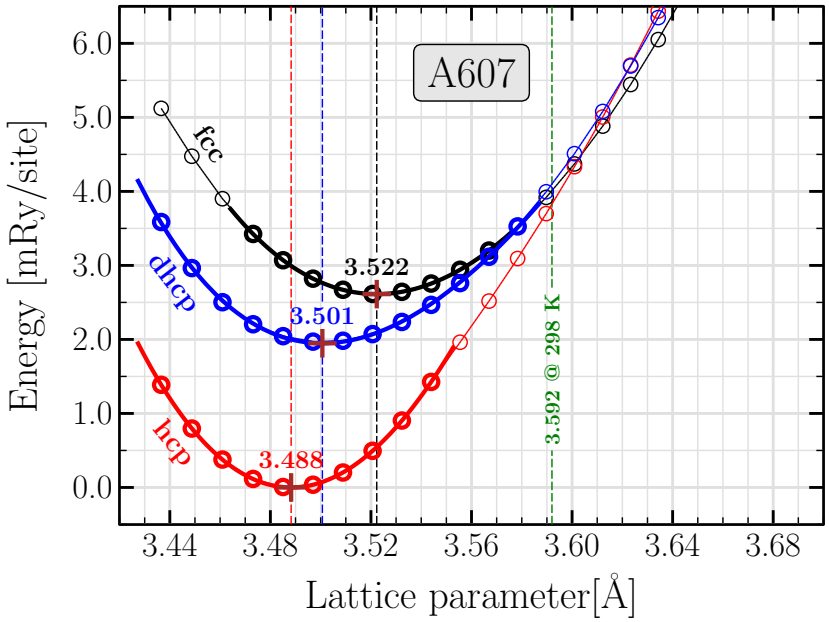

(a)

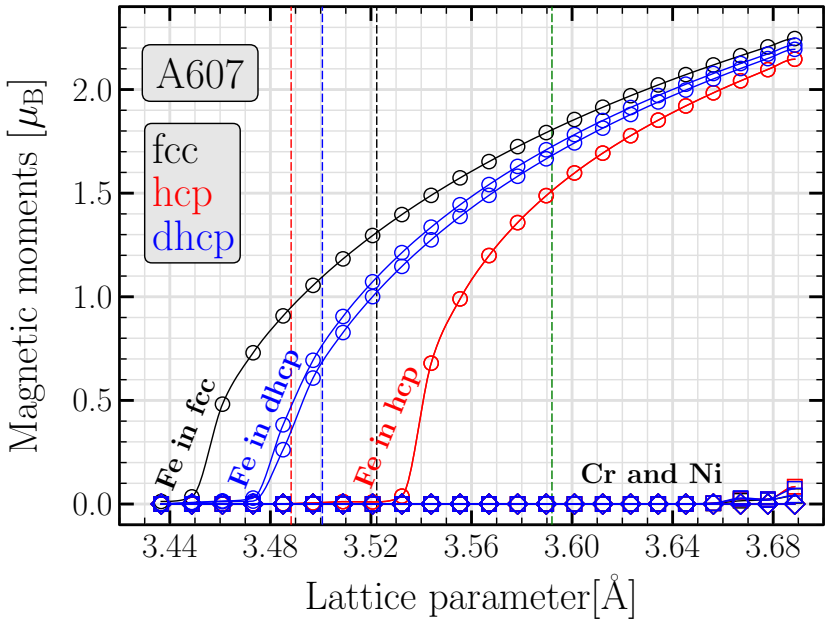

(b)

Figure 5.7: In the A607 alloy, as the lattice parameter changes, (a) shows the changes in the total energy, and (b) depicts the behavior of the local magnetic moment of all elements. Both parameters have been calculated using the soft-core approach and the GGA functional. The green vertical line indicates the measured fcc lattice parameter at room temperature, as presented in Fig. 5.10

all three phases, we ensure the equal inter-atomic distances and also the same volume per site for all of them.

The equilibrium lattice parameter is obtained by fitting the Murnaghan equation of state [114] to a number of total energies calculated for different volumes, as presented in Fig. 5.7(a). Our results show, for the A607 alloy in the paramagnetic state at 0 K equilibrium, that hcp is found as the most stable phase among the three studied phases, followed by dhcp and finally fcc. It is also found that the equilibrium volume is smaller for the more stable phases. As the volume increases from the equilibrium, the phase stability in the paramagnetic state changes so that the fcc phase first overtakes the dhcp phase, and later overtakes the hcp phase, resulting in an hcp→fcc phase transition.

In metallurgy, the higher stability of the hcp phase at low temperatures, with respect to the fcc phase, is a well-known fact which results in the cryogenic transition of γ-austenite to the ϵ-martensite (a paramagnetic [11] hcp phase) on cooling [115]. The ϵ-martensite is usually considered as an intermediate phase which transforms to the more stable α'-martensite with ferromagnetic body-centered tetragonal (bct) structure [11, 13, 116, 117, 118, 119]. The overall $\gamma \rightarrow \epsilon \rightarrow \alpha'$ transition is called *martensitic transformation*. The formation of α'-martensite is a subsequence of the presence of carbon in the alloy. In fact, at very low temperatures, the most stable phase of the high-purity Fe–Cr–Ni alloys is the α-ferrite with ferromagnetic bcc structure. Since the carbon solubility in the bcc phase is very low, the unit cell is expanded along one of its sides, resulting in body-centered tetragonal structure. With higher carbon concentrations, more interstitial sites are filled, and the tetragonality increases [115].

When cooling austenite, the martensitic transformation starts as temperature reaches the *martensite start temperature*, M_s. However, the transition may also occur at higher temperatures, if mechanical stresses are applied to the material, for example during the process of cold work. In the absence of these mechanical stresses, M_s may be estimated using Eichelman and Hull empirical equation[1] [115]

$$\begin{aligned} M_s\ [\mathrm{K}] = 1578 - 41.67\,x_{\mathrm{Cr}} - 61.11\,x_{\mathrm{Ni}} - 33.33\,x_{\mathrm{Mn}} \\ -27.78\,x_{\mathrm{Si}} - 1667(x_{\mathrm{C}} + x_{\mathrm{N}}), \end{aligned} \tag{5.12}$$

where x_i denotes the concentration of element i in the unit of weight percent. Substituting the chromium and nickel concentrations in the equation, M_s is estimated about 250 K (−23 °C) for the A607 alloy, explaining its fcc structure at room temperature and its hcp structure at low temperatures. This agrees with the results of our ground-state DFT calculations, where, at 0 K, the paramagnetic hcp phase is found more stable than the paramagnetic fcc phase.

[1] As mentioned in the book *STEELS: Processing, Structure, and Performance* [115], the equation has originally been published in 1953 by Eichelman and Hull [120]. Since we did not have access to the original article, we took the equation from this book in the form of

$$M_s\ [^\circ\mathrm{F}] = 75(14.6 - x_{\mathrm{Cr}}) - 110(8.9 - x_{\mathrm{Ni}}) - 60(1.33 - x_{\mathrm{Mn}}) - 50(0.47 - x_{\mathrm{Si}}) - 3000[0.068 - (x_{\mathrm{C}} + x_{\mathrm{N}})]$$

and converted it from Fahrenheit unit (°F) to Kelvin (K).

Experimental data shows that stainless steels with composition close to A607 may have a mixture of different phases, depending on their production conditions like cooling rate. The equilibrium phase diagram predicts that this alloy may contain γ, α, and σ phases at room temperature (see Fig. 2.8). However, as the alloy is found in austenite phase at high temperatures, the full austenite phase can be maintained by rapid cooling to room temperature (for instance, by quenching in water) [121]. These statements emphasizes the importance of the production process. As a direct experimental evidence, we can refer to our XRD measurements on samples of Böhler A607, where only the presence of fcc phase was observed. We can compare our *ab-initio* lattice parameter with its corresponding experimental value measured for the fcc lattice at 298 K (25 °C), presented in Fig. 5.10. Our theoretical value, $a_{\mathrm{A607}}^{\mathrm{fcc,DFT}} = 3.522$ Å, agrees with the measured value, $a_{\mathrm{A607}}^{\mathrm{fcc,EXP}}(T = 298\,\mathrm{K}) = 3.592$ Å, within 2%.

In Fig. 5.7(b), the magnetic moments in the DLM state are plotted versus the lattice parameter for all elements in the three phases. The plot shows that, in all three phases, chromium and nickel remain nonmagnetic in the entire range of the lattice parameter. However, the magnetic moment of iron shows a direct dependence on the lattice spacing, so that while it remains negligible for smaller volumes, it increases significantly with the lattice parameter, introducing a low-spin to high-spin magnetic transition. In different phases, this transition occurs at different volumes, so that at a certain lattice parameter, an iron atom has quite different magnetic moments in different phases. As a result of this behavior, iron is already magnetic at the equilibrium volume of the fcc and dhcp phases, while it is still nonmagnetic at the equilibrium volume of the hcp phase. In the limit of large volumes, however, all three phases exhibit the same magnetic behavior. In all three phases, unlike their equilibrium volumes, iron atoms have significant magnetic moments between $1.55\,\mu_{\mathrm{B}}$ and $1.85\,\mu_{\mathrm{B}}$ at the lattice parameter measured at room temperature. It shows that the usage of the theoretical lattice parameter can lead to an unrealistic description of the magnetic configuration of the alloy, resulting in wrong values for the SFE.

Delczeg *et al.* have recently calculated the equilibrium lattice parameters for the paramagnetic state of Fe–Cr–Ni alloys using a method similar to what we use here, *i.e.*, the EMTO approach [122]. For $Fe_{74}Cr_{18}Ni_8$ alloy, they have reported 3.605 Å for the fcc lattice parameter at 0 K equilibrium, which, compared to our result, is closer to the room-temperature experimental value.

The difference between this value and our result comes from the different treatments applied for core electrons. While we use the soft-core approach, they have used frozen-core approximation, a simplified description of core electrons that results in larger equilibrium lattice parameters at 0 K which are closer to experimental data [122, 123, 124], but can not be justified theoretically. A comparison between the soft- and the frozen-core approaches is presented in Fig. 5.8, where the equilibrium volume and the local magnetic moments are plotted for the fcc phase of A607 alloy. More detailed informations, including the experimental values for the room-temperature lattice parameter and the bulk modulus are given in Tab. 5.4. Our results show that the equilibrium volume and the bulk modulus calculated using the soft-core approach

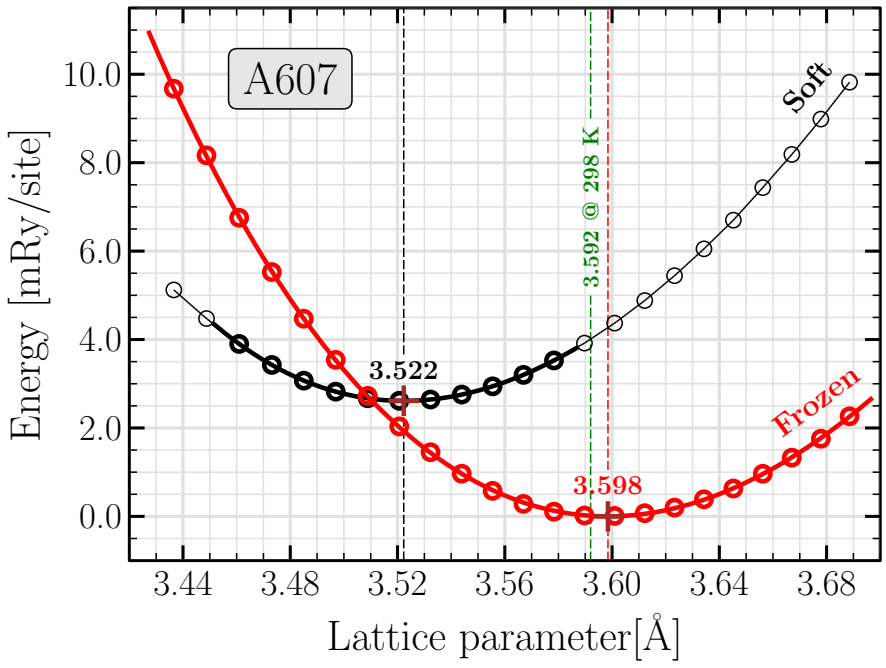

(a)

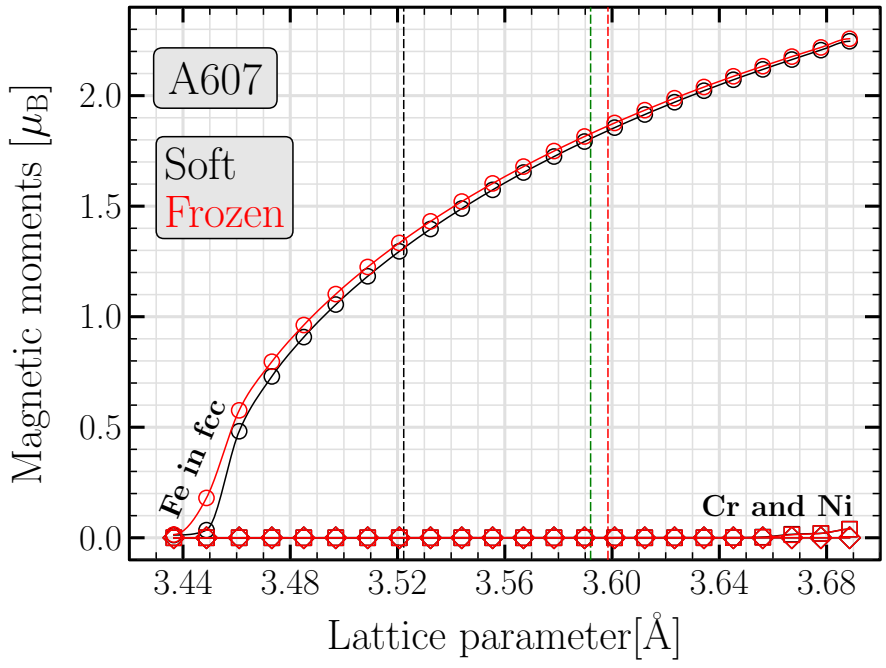

(b)

Figure 5.8: Comparison of the physical properties of the A607 alloy, calculated using the soft-core and the frozen-core approaches. As the lattice parameter increases, (a) presents the changes in the total energy, while (b) shows the behavior of the local magnetic moments.

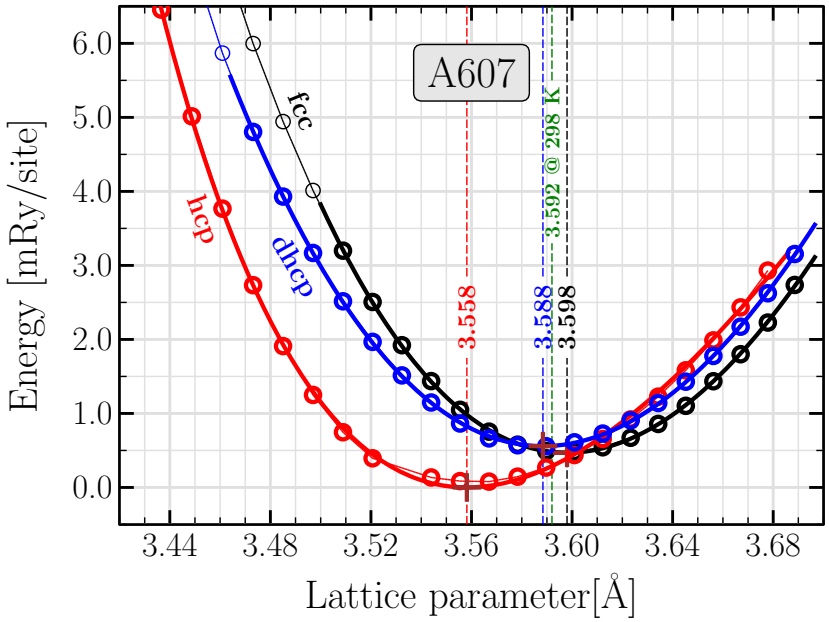

(a)

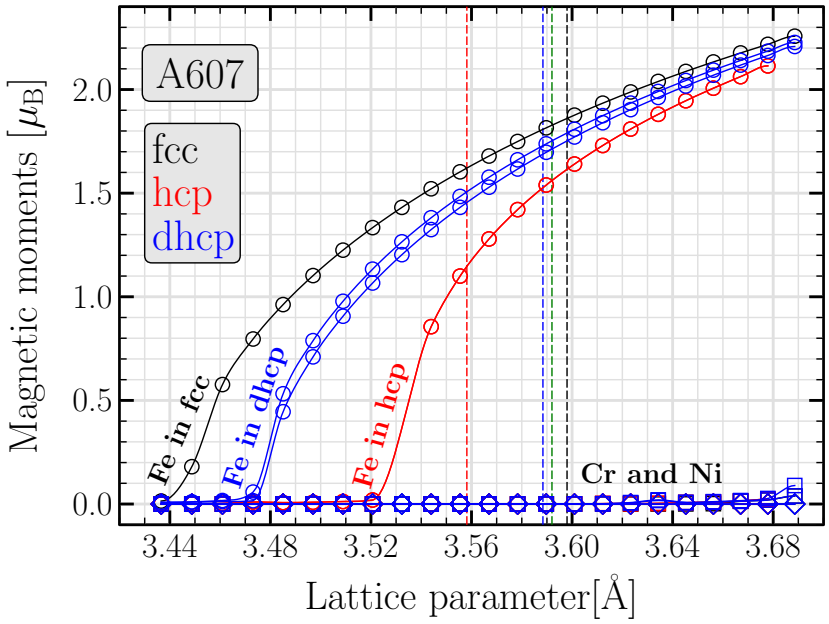

(b)

Figure 5.9: A607 alloy: as the lattice parameter changes, (a) shows the changes in the total energy, and (b) depicts the behavior of the local magnetic moment of all elements. In these calculations the frozen-core approximation has been applied. Compared to Fig. 5.7, these approximation results in a significant shift in the equilibrium lattice parameter, while the behavior of the magnetic moments remain almost unchanged.

Table 5.4: The calculated equilibrium lattice spacing and the bulk modulus of three phases, compared to available experimental data. Note that the fcc lattice parameter a_{fcc}, is derived using the equilibrium volume of every phase.

phase	a_{fcc} [Å]			B [GPa]		
	soft-core	frozen-core	experiment	soft-core	frozen-core	experiment
fcc	3.522	3.598	3.592	172.2	164.9	∼160.0 [23]
hcp	3.488	3.558	—	271.5	152.2	—
dhcp	3.501	3.588	—	178.2	153.0	—

are respectively smaller and larger then those coming through the frozen-core approximation. This suggest that the frozen-core approximation, compared to the soft-core approach, underestimate the strength of atomic interactions in the metal.

Despite significant difference in the equilibrium volumes calculated using the two core-electron treatments, Fig. 5.8(b) shows that both approaches result in very similar values calculated for the magnetic moments. In the first look, it might point the dominance of the valence states in the magnetization of elements, as these states are equally calculated in both approaches. However, unless it is proven using other methods, a question rises here: If the frozen-core approximation can describe the magnetic structure of the system in similar manner as it is done by the soft-core approach, why it results in different equilibrium volume? To answer this question, whether the mentioned magnetic makeup is correct, or it is just an accident, or it is a bug in the implementation of the frozen-core approximation in the code, further investigations are required.

The E-V curves calculated for three phases using the frozen-core approximation are presented in 5.9. These results show that, using the frozen-core approximation, the most stable phase at 0 K equilibrium is hcp, followed by fcc and dhcp. This is different than the order we found using the soft-core approach: hcp, dhcp, and fcc (see Fig. 5.7). Moreover, compared to Fig. 5.7, Fig. 5.9 shows that, at 0 K equilibrium, the energy differences between the three phases become smaller when the frozen-core approximation is applied. These differences become of particular importance when investigating the SFE which, in the absence of the entropy at 0 K, is calculated as

$$\text{SFE}(T = 0\,\text{K}) = \frac{E^{\text{hcp}} + 2E^{\text{dhcp}} - 3E^{\text{fcc}}}{A}, \tag{5.13}$$

resulting in values of $-126\,\text{mJ/m}^2$ and $6\,\text{mJ/m}^2$ for soft- and frozen core approaches, respectively. Finally, in the hcp phase, Fig. 5.9 shows a kink in the E-V curve at $a_{\text{fcc}} \approx 3.53\,\text{Å}$, which can be related to a low-spin to high-spin magnetic transition of iron atoms. Although the same transition is observed in all phases in Figs. 5.7(b) and 5.9(b), except the hcp phase with frozen-core approximation, it never results in a visible change in the corresponding E-V curves.

Our methodology of the SFE evaluation requires the accurate values of the differ-

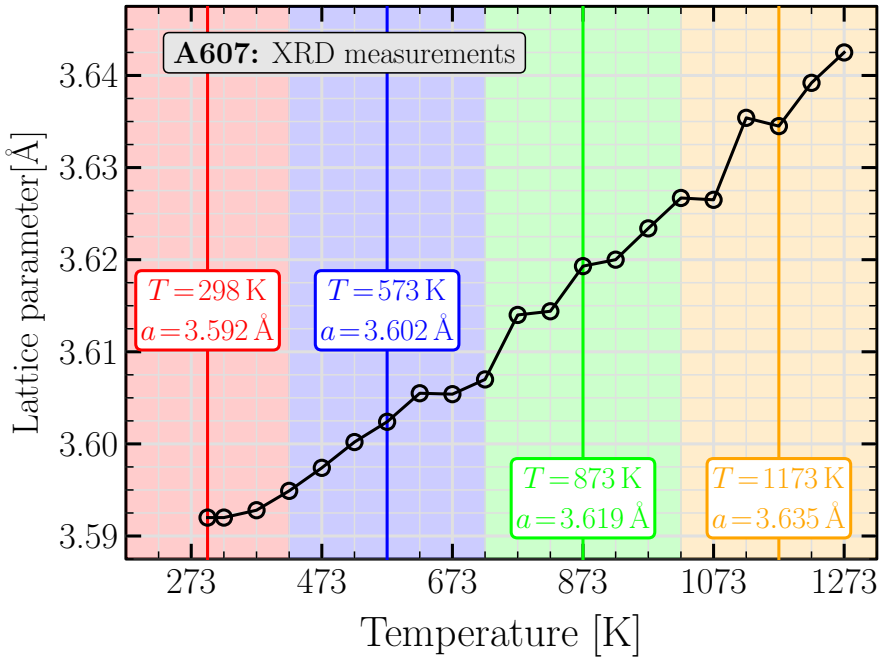

Figure 5.10: The thermal lattice expansion data for the A607 alloy, as measured using the XRD method during heating process. The temperature range is divided into four intervals, where the lattice parameter at the middle of every interval is used in the LSF calculations.

ences between free energies of the mentioned three phases, which depend highly on the correct values of the total energy as well as of the local magnetic moments. Both of these parameters are significantly affected by volume. When considering the temperature dependence of the SFE, the process becomes more challenging as all values are needed as a function of temperature. However, the temperature dependence of the lattice parameter can not be evaluated easily, as there is no available methodology to evaluate the vibrational free energies in paramagnetic random alloys. In order to surmount this difficulty, we have measured the thermal lattice expansion of Böhler A607 to provide the temperature dependence of the lattice parameter of A607 alloy. The XRD experimental lattice parameters are presented in Fig. 5.10.

5.4.2 Longitudinal Spin-Fluctuations

In order to describe the thermal excitation of the local magnetic moments in the paramagnetic DLM state, we use a simple model based on the unified itinerant magnetism theory [125]. While the theory includes both transverse and longitudinal spin-fluctuations on equal footing, we assume in our simplified model that the transverse spin-fluctuations, *i.e.*, the fluctuation in the orientations of the magnetic moments, always follows the completely disordered configuration, as described in the DLM state. For evaluating the longitudinal spin-fluctuations (LSF), *i.e.*, the fluctuation in the size of the magnetic moments, a classic Monte-Carlo simulation is performed over a mapping

of the system energetics, calculated using the EMTO method for relevant configurations.

Ruban *et al.* [126] have introduced a magnetic Hamiltonian which, taking into account the LSF, can give a quite accurate representation of the energy of the classical magnetic state, as well as the values of the magnetic moments in the state. Their Hamiltonian for a system consist of identical atoms is defined as

$$H_{\text{mag.}} = \sum_i J^{(0)}(\bar{M}) + \sum_i J^{(1)}(\bar{M}, M_i) + \sum_{ij} J_{ij}^{(2)}(\bar{M}, M_i, M_j)\vec{M}_i \cdot \vec{M}_j, \tag{5.14}$$

where the vector quantity $\vec{M}_i$ is the local spin moment of an atom in position i, whose length M_i can have any positive value. $\bar{M} = \langle M_i \rangle = \frac{1}{N}\sum_i M_i$ denotes the average value of the local magnetic moments in the system. $J^{(0)}(\bar{M})$ is the zeroth-order term defined as the energy of a homogeneous DLM state representing a system of randomly oriented spins with a fixed value of the magnetic moments $\bar{M}$. $J^{(1)}(\bar{M}, M_i)$ is the on-site term, the LSF energy, which is the energy required to change the size of the magnetic moment of the atom in position i, from the corresponding DLM value $\bar{M}$ to M_i. Finally, $J_{ij}^{(2)}(\bar{M}, M_i, M_j)$ is the pair exchange interaction parameter, which describes the magnetic interaction between atoms in positions i and j, with local magnetic moments M_i and M_j embedded in the DLM effective medium.

Using a similar approach, Reyes-Huamantinco *et al.* have recently calculated the single-site LSF for the paramagnetic iron-manganese binary alloys [101]. However, they assume that the free energy is dominated by single-site magnetic fluctuations in the paramagnetic DLM state, thus they define a Hamiltonian which includes only the first term of Eq. 5.14. Following their approach, we can rewrite the Hamiltonian for an alloy as

$$H_{\text{mag.}} = \sum_s c_s J_s(m_s), \tag{5.15}$$

where s stands for the elements in the alloy (s = Fe, Cr, and Ni here), c_s is the concentration of element s, m_s is the *spatially-averaged* local magnetic moments of element s, and, finally, $J_s(m_s)$ is the energy required to excite these averaged moments from 0 to the value m_s in the DLM paramagnetic state. In fact, $J_s(m_s)$ in Eq. 5.15 corresponds to $J^{(0)}(\bar{M})$ in Eq. 5.14. Note that, while the Eq. 5.14 includes terms related to all individual atoms in the system (expressed by summation $\sum_i$), the Eq. 5.15 contains only the single-site terms, which might be considered as an average over all atoms. That is why the summation $\sum_i$ has disappeared in the Eq. 5.15.

5.4.2.1 DFT Calculations of the LSF Hamiltonian

Generally, by expressing the total energy of system as a function of magnetic moments, the magnetic Hamiltonian provides an insight into the magnetic characteristic of the system. In our simplified model, this Hamiltonian contains only those parameters which are related to the homogeneous DLM state, as presented in Eq. 5.15. In order to calculate these parameter for our ternary system, we start with the methodology

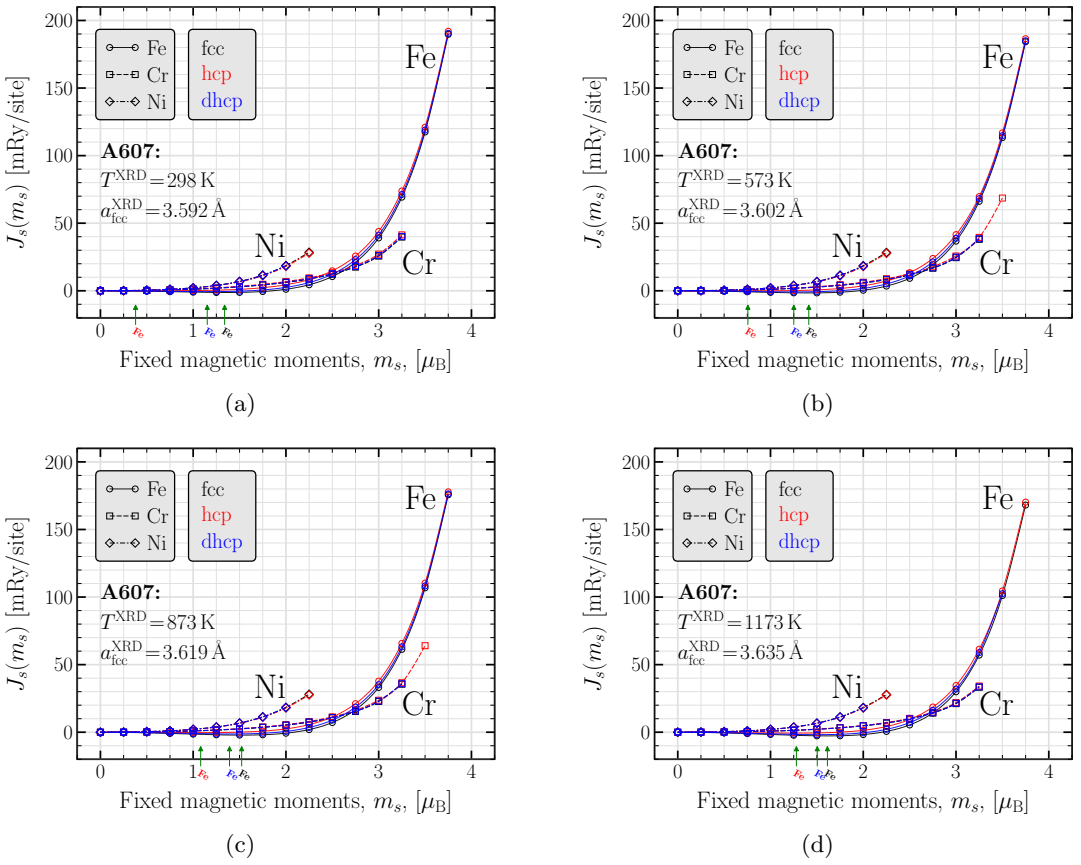

Figure 5.11: The overall behavior of the Hamiltonian parameters $J_s(m_s)$ versus the size of the magnetic moments m_s, as calculated using four experimental lattice parameters in the A607 alloy. For a closer view of the region around the horizontal axis, see Fig. 5.12.

developed by Reyes-Huamantinco *et al.* [101], and expand it to include the thermal lattice expansion of the alloy.

The parameters are calculated using the EMTO method, where the cell volume and consequently the atomic distances are adjusted based on the experimental lattice parameters measured for Böhler A607 alloy, as presented in Fig. 5.10 (see Sec. 5.4.1 for a discussion about the relevant choice of the lattice spacing). In order to do so, taking only the heating branch of the lattice thermal expansion curve, the desired temperature range 273 K–1273 K (0 °C–1000 °C) is divided into four intervals, whose middle values are selected for our calculations (see Fig. 5.10). The total energy is evaluated via the self-consistent DFT calculations, where the magnetic moments of the element $s \in \{\mathrm{Fe}, \mathrm{Cr}, \mathrm{Ni}\}$ are fixed to the value $m_s \in \{0.00, 0.25, 0.50, \cdots, 4.00\ \mu_{\mathrm{B}}\}$ and the moments of the other elements, *i.e.*, $s' \neq s$, are allowed to relax. In this calculations, the exchange-correlation (XC) effects are approximated using the local spin density approximation (LSDA) [127], since it has been reported in the cases of bcc

Table 5.5: Comparison of the magnetic moments of iron, calculated in the DLM paramagnetic state of the A607 alloy using the LSDA and the GGA functionals. The LSDA magnetic moments have been obtained according to the minimum total energy of the system, normalized to the total energy of the corresponding nonmagnetic state, $\Delta E_{\mathrm{Fe}} = E_{\mathrm{Fe}}(m_{\mathrm{Fe}}) - E_{\mathrm{Fe}}(0)$(see Fig. 5.12).

T^{XRD} [K]	$a_{\mathrm{fcc}}^{\mathrm{XRD}}$ [Å]	phase	GGA m_{Fe} [μ_{B}]	LSDA m_{Fe} [μ_{B}]	LSDA ΔE_{Fe} [mRy]
298	3.592	fcc	1.805	1.339	−1.288
		hcp	1.512	0.379	−0.004
		dhcp	1.725	1.152	−0.616
573	3.602	fcc	1.863	1.413	−1.597
		hcp	1.610	0.756	−0.066
		dhcp	1.792	1.251	−0.855
873	3.619	fcc	1.951	1.523	−2.154
		hcp	1.748	1.081	−0.305
		dhcp	1.891	1.392	−1.316
1173	3.634	fcc	2.023	1.613	−2.724
		hcp	1.854	1.279	−0.647
		dhcp	1.972	1.504	−1.809

iron [128] and bcc chromium [129] to result in more realistic magnetic moments with respect to the generalized gradient approximation (GGA) [102]. This approach gives the total energy of system $E_s(m_s)$ as a function of the magnetic moments of element s. The Hamiltonian parameters are obtained by normalizing these energies to the energy of nonmagnetic state: $J_s(m_s) = E_s(m_s) - E_s(0)$.

For the A607 alloy, we present the overall behavior of $J_s(m_s)$ in Fig. 5.11, while a more detailed presentation with focus on a small region around the horizontal axis is available if Fig. 5.12. For any of the elements chromium and nickel, our results show almost the same behavior of the the total energy, where it monotonically increases with the magnetic moments. It suggest that chromium and nickel are nonmagnetic at the equilibrium DLM state, as it was also mentioned when discussing the volume effects in Sec. 5.4.1. On the other hand, it shows that when enough energy is provided, for instance in the form of thermal energy, these two elements can excite to magnetic states. This behavior demonstrates the itinerant nature of the electron magnetism in chromium and nickel. However, the steeper curve of nickel shows that there are more available states with larger variety of magnetic moments for chromium than for nickel.

In the case of iron, unlike chromium and nickel, the energy curve always passes a shallow minimum as the magnetic moments increase from zero. These minimums and their corresponding magnetic moments are presented in Tab. 5.5, also indicated on the horizontal axes in the figures. First of all, a minimum in the energy curve shows that iron is magnetic at the equilibrium DLM state, indicating the Heisenberg nature of

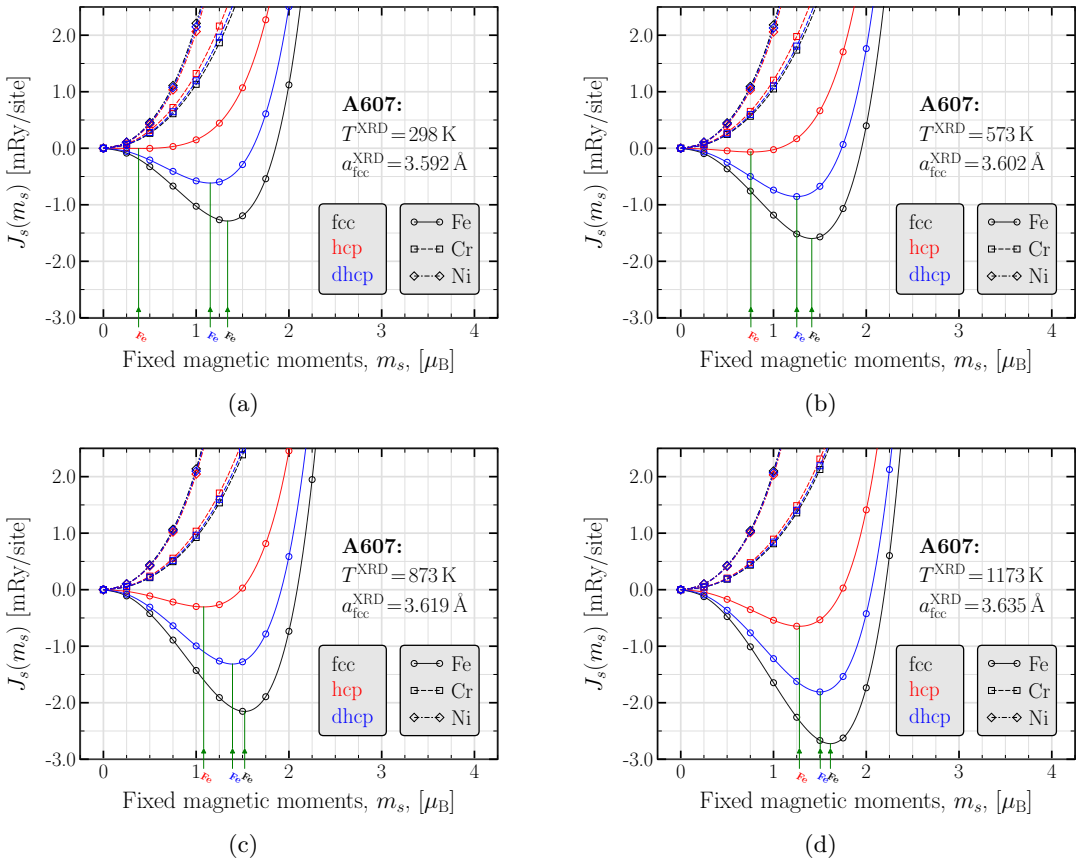

Figure 5.12: The dependence of the Hamiltonian parameters $J_s(m_s)$ on the size of the magnetic moments m_s, as calculated using four experimental lattice parameters in the A607 alloy. As the graph zooms in on a small region around the the horizontal axis, the minimum of curves $J_{\mathrm{Fe}}(m_{\mathrm{Fe}})$ are unveiled.

its electron magnetism. Secondly, the small depth of this minimum indicates the low-energetic accessibility of spin fluctuations with a large variety of the magnetic moments, which reflects the itinerant nature of the magnetism in this element. Although both Heisenberg and itinerant types of magnetism are present in iron, later we will see that the Heisenberg type is dominant.

We can also compare these curve with E-V curves, presented in Fig. 5.7. For an easier comparison, see the GGA and the LSDA magnetic moments in Tab. 5.5. We find that the energy minimums in the J_{Fe} occur at magnetic moments which are smaller then their corresponding values calculated in Sec. 5.4.1. These differences are partially due to the different exchange-correlation approximations applied in the two series of calculations, *i.e.*, the GGA-PBE functional used in the calculations of volume effects, while the LSDA functional was selected for the LSF calculations.

On the horizontal axes, as the volume increases (for instance, by moving from

Figs. 5.12(a) to Figs. 5.12(d)), the positions the these minimums get closer to each other, suggesting that the equilibrium states of three phases converge at larger volumes. Moreover, they are deeper when calculated with larger lattice spacing. Generally, a deeper minimum shows that the magnetic moments of the system are more localized, and hence it is more difficult for them to be excited to states with higher energy, indicating the weak itinerant nature of the system. Based on the same argument, in our Fe–Cr–Ni alloy, the fcc and the hcp phases demonstrate the weakest and the strongest itinerant magnetism, respectively. Finally, the relatively small slope of all energy curves around their minimum emphasizes the strong possibility of the spin fluctuations in this alloy, which are necessary to be taken into account in order to get an accurate physical description of the system.

We can also plot the related magnetic moments which evidence the correlations between the magnetic moments of different elements in the alloy (see Figs. 5.13 – 5.16). In all cases, the magnetic moments of chromium (red curves) and nickel (blue curves) remain unchanged as the moments of any other element increase. On the other hand, magnetic moments of iron (black curves) exhibit only a week correlation with moments of other elements, where they increase with chromium moments, but decrease as nickel moments increase. This indicates that the magnetic interactions among different species are generally weak.

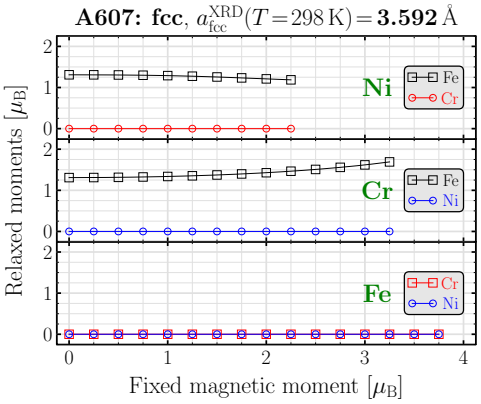

(a)

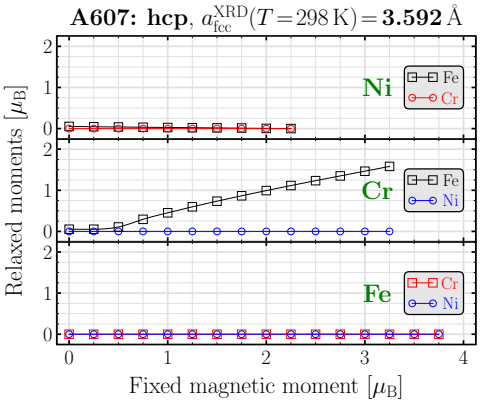

(b)

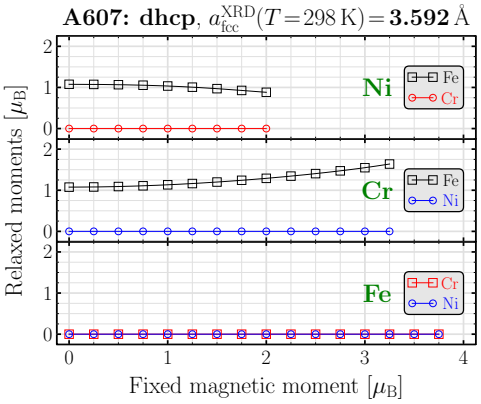

(c)

Figure 5.13: The correlation between magnetic moments in A607 alloy, using the lattice parameter at 298 K.

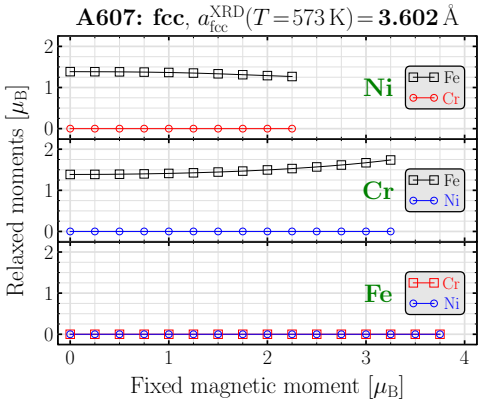

(a)

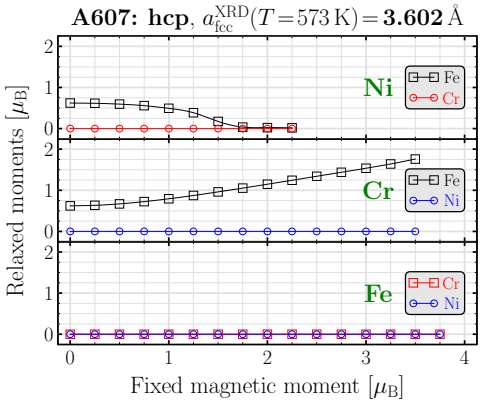

(b)

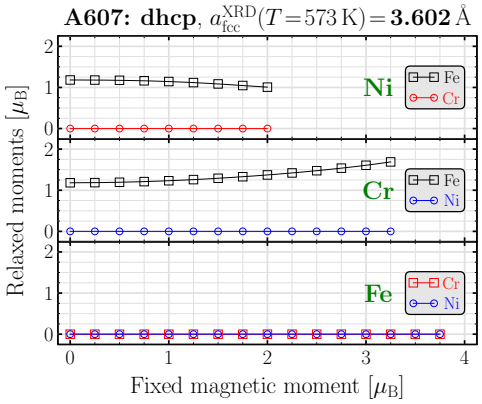

(c)

Figure 5.14: The correlation between magnetic moments in A607 alloy, using the lattice parameter at 573 K.

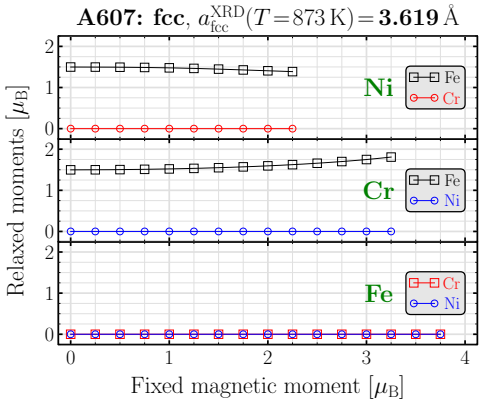

(a)

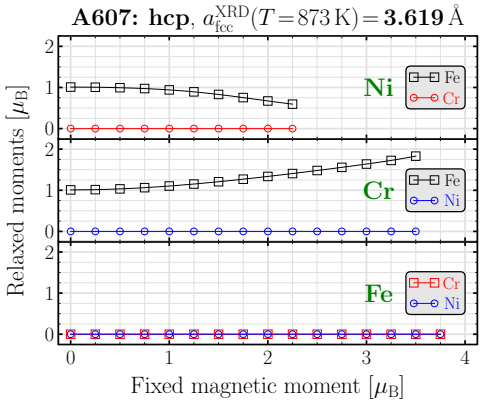

(b)

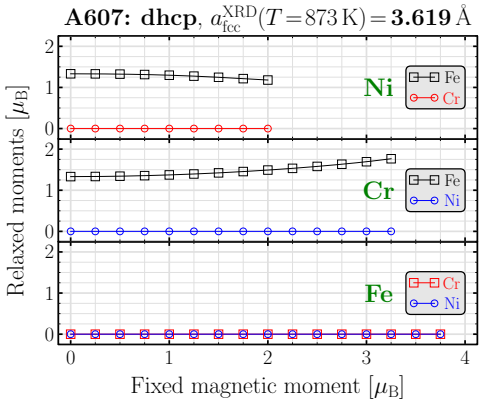

(c)

Figure 5.15: The correlation between magnetic moments in A607 alloy, using the lattice parameter at 873 K.

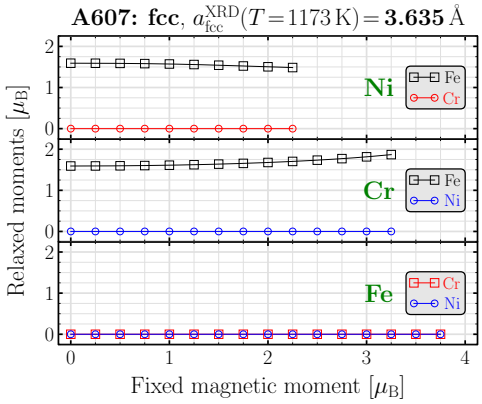

(a)

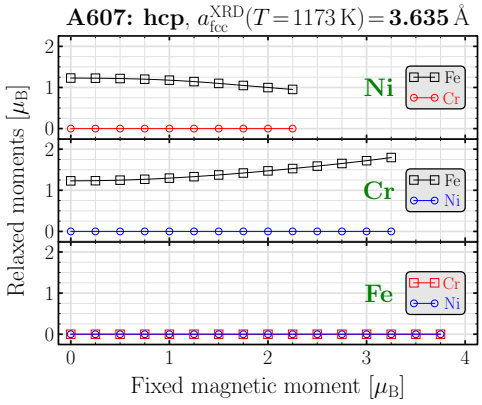

(b)

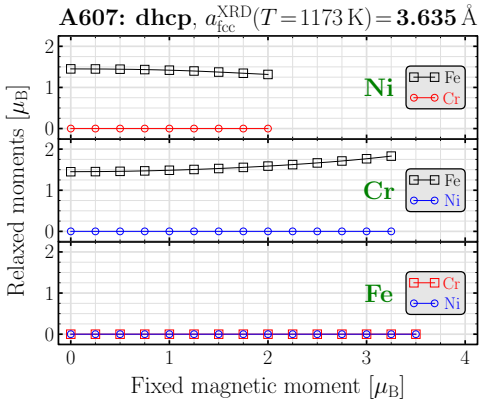

(c)

Figure 5.16: The correlation between magnetic moments in A607 alloy, using the lattice parameter at 1173 K.

5.4.2.2 Monte Carlo Calculations

As it was already mentioned, once the system energetics are known, a Metropolis Monte-Carlo technique can be used in order to obtain the temperature-dependence of the local magnetic moments. In this approach, a system of randomly oriented spins is considered whose configuration is progressively altered by changing the size of its individual spins in a random manner. After the change applied, the total energy is calculated using a classical magnetic Hamiltonian, where the dependence of the total energy on the size of the magnetic moments has been defined using the energetics of the paramagnetic random alloy, $J_s(m_s)$, calculated using the EMTO method (see the previous section). A change in the system configuration is always permitted, if it lowers the system total energy, *i.e.*, it results in a negative ΔE, defined as $\Delta E = E_{\text{after}} - E_{\text{before}} < 0$, where E_{after} and E_{before} are the system total energies after and before the change, respectively. Otherwise, when $\Delta E > 0$, the changed configuration might be accepted depend on the excitation probability, which is defined as $e^{-\Delta E/T}$. As it is obvious from this definition, when $\Delta E > 0$, a configuration with larger $\Delta E/T$ has lower chance to be accepted. The process is repeated for many times, so that the changes in total energy, ΔE, become very small, showing that the current configuration is already very close to the equilibrium configuration with the lowest energy. Once this conditions is satisfied, the *spatial average* of the magnetic moments is calculated.

The algorithm starts with the highest temperature in the desired range, and while decreasing the temperature step by step, tries to find the equilibrium configuration of the magnetic moments. The outputs related to the four selected experimental lattice parameters are presented in Fig. 5.17, where different phases are distinguished with their corresponding colors.

For the DLM paramagnetic state, our results predict that, in all three phases, iron holds significant magnetic moments at 0 K, evidencing the contribution of localized *d*-electrons to its magnetism. This behavior is a characteristic of systems which follow the Heisenberg model of magnetism. However, as temperature rises, the magnetic moments of iron grow, which is a characteristic of the itinerant magnetism [126]. So we can conclude that, the electron magnetism in iron forms as a mixture of both Heisenberg and itinerant types. The itinerant nature of magnetism is stronger in the hcp phase, followed by dhcp and fcc, as determined by the slope of their corresponding curves, particularly at lower temperatures. In the entire temperature range, the fcc phase has the largest magnetic moments of iron, followed by dhcp and hcp, same as for iron in Fe–Mn alloys [101]. Chromium and nickel, on the other hand, find significant magnetic moments only due to the thermal excitation of their spins, indicating the pure itinerant nature of their electron magnetism.

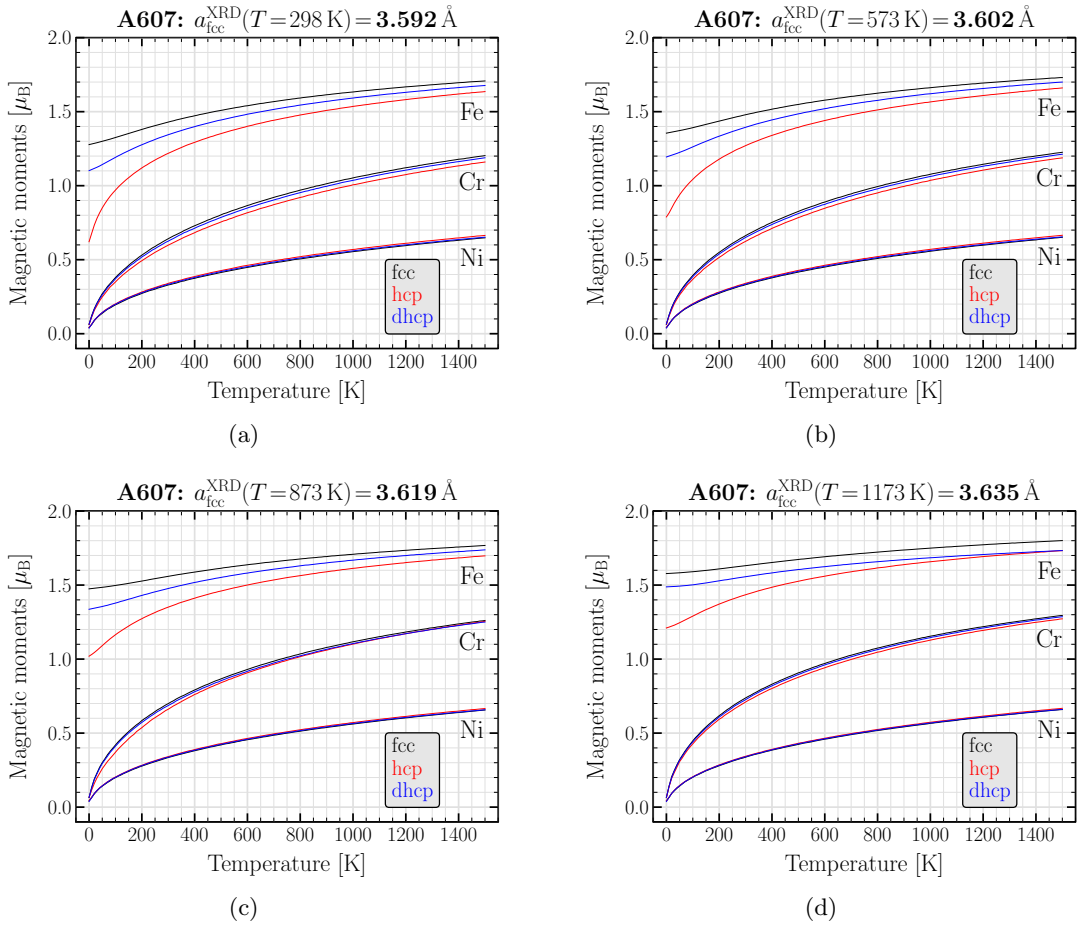

Figure 5.17: The dependence of the magnetic moments on the temperature, calculated for the A607 alloy, using four different experimental lattice parameters.

5.4.3 The SFE Calculations

Once the temperature dependence of the lattice parameter (through the XRD measurements) and of the local magnetic moments (through the Monte-Carlo step of the LSF calculations) are known, we can perform a set of constrained DFT calculations in order to find the free energy of every phase as a function of temperature. These calculations are called constrained because the magnetic moments of all atom types are fixed to their corresponding values evaluated using the Monte-Carlo method (see Subsec. 5.4.2.2). The SFE is then evaluated using these free energies, as expressed in the Eq. 5.5.

In Fig. 5.18(a), the SFE's are presented according to five sets of the LSF calculations. The first set uses the theoretical equilibrium volume, while the other four sets utilize the measured lattice parameters at 298, 573, 873, and 1173 K (25, 300, 600, and 900 ℃, respectively). For every set, in order to find the SFE at all temperatures in the range, a third order polynomial is fitted into the calculated points. All curves are ascending, which exhibit an increase in the SFE with temperature. Moreover, it is found that using a larger volume in the LSF calculations results in a larger SFE's. The colored curves are more reliable in a temperature range around the point at which their corresponding lattice parameters have been measured. These ranges and their corresponding data points are highlighted in Fig. 5.18(b). The overall temperature dependence of the SFE can be found by fitting a third order polynomial into these highlighted points. We find that, for the A607 alloy, the SFE almost linearly increases with the temperature:

$$\mathrm{SFE}^{\mathrm{A607}}(T) = 1.296\times10^{-8}\ T^3 - 3.924\times10^{-5}\ T^2 + 1.006\times10^{-1}\ T - 3.530\times10^{1} \quad (5.16)$$

where T and $\mathrm{SFE}^{\mathrm{A607}}$ are in Kelvin and $\mathrm{mJ/m^2}$, respectively.

Generally, finding a trusted experimental value for the SFE is quite challenging. As presented in Tab. 1.1, uncertainties up to 30% have been reported in the case of pure metals, making it difficult to fully rely on an individual experimental value. One must also take into account that, when measuring the SFE in alloys, the problem becomes even more elaborate due to complexities which are a part of the nature of the composition compared to a pure material. Particularly for steels, comparing the calculated SFE's with experimental values is not a straightforward task, since experimental samples always contain small fractions of other elements, making them different from the simulated systems. Moreover, the process of sample preparation alters its final microstructure, a property which highly governs the SFE measurements, and hence significantly changes the measured results, even for samples with equal chemical compositions. For instance, for plain carbon steels in the γ-phase at high temperature, the SFE has been measured between 70 $\mathrm{mJ/m^2}$ and 100 $\mathrm{mJ/m^2}$ (almost 50% deviation), based on the material grain size [130]. Specially when the temperature dependence of the SFE is intended, some irreversible changes may be introduced in samples as they are heated up or cooled down again (see the references of the reported experimental results).

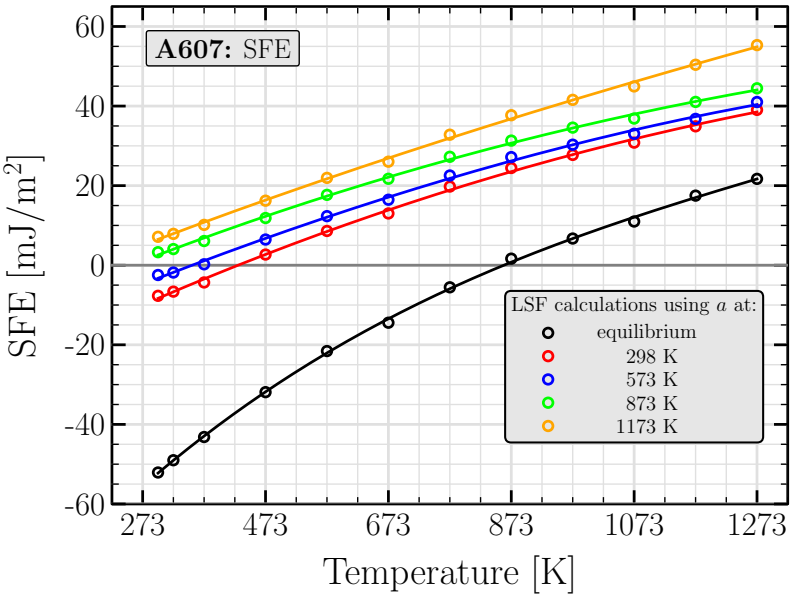

(a)

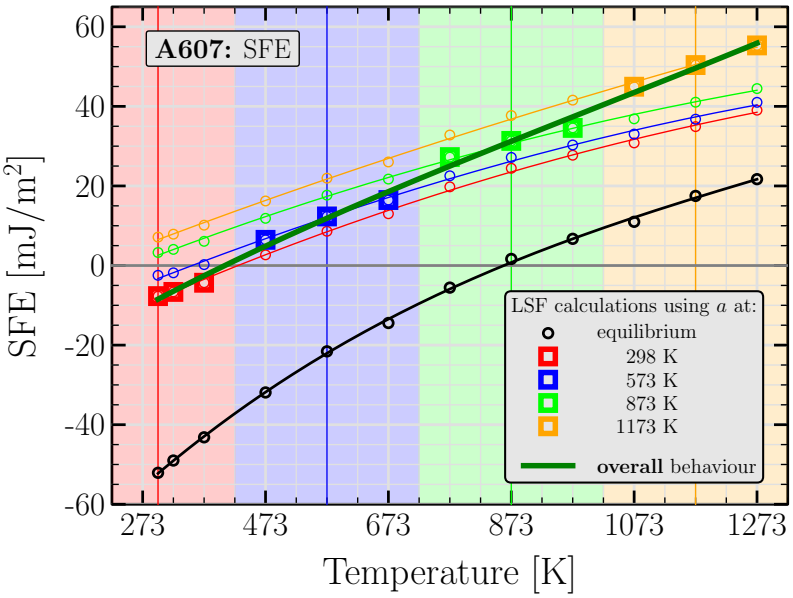

(b)

Figure 5.18: (a) The temperature dependence of the SFE, evaluated for A607 alloy. Different curves correspond to different volumes used in the LSF calculations. Using the experimental lattice parameter (colored curves) instead of the equilibrium value (black curve) increases the SFE significantly. (b) The temperature interval is divided into 4 regions (see Fig. 5.10), where the most relevant points of every curve is selected. The overall behavior of the SFE is found by fitting a third order polynomial to the selected points.

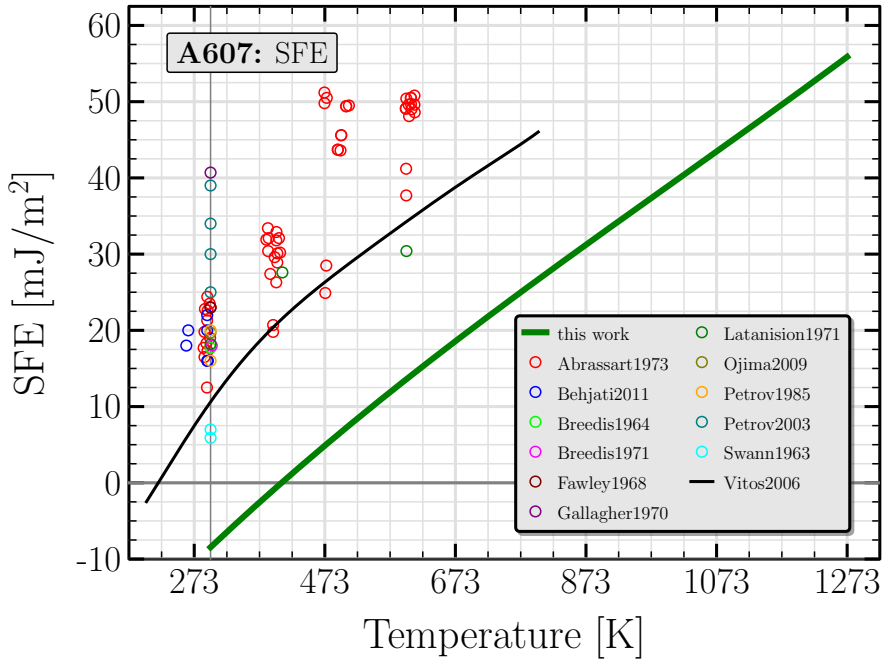

Figure 5.19: Comparison between our results and available experimental and theoretical SFE's for A607 alloy. Experimental data are presented for alloys where the deviation of the chemical composition from our A607 is in the range of ±4 at.%, ±2 at.%, and ±2 at.%, respectively for iron, chromium, and nickel. However, the accurate composition of these alloys are presented in Appendix B. The black curve presents the temperature dependence of the SFE, calculated for $Fe_{74}Cr_{18}Ni_8$ [8]. Room temperature has been indicated by a vertical line at 298 K (25 °C).

Experimental values for the SFE can be found in Appendix B, where a summary of a review on relevant publications is presented. In order to compare our results with available experimental values, we select only those alloys where the deviation of the chemical composition from our A607 is in the range of ±4 at.% for iron and ±2 at.% for chromium and nickel. Although we ignore the presence of any other elements, we omit alloys where the summation of all ignored concentrations exceeds the limit of ±2 at.%. Our calculated SFE and the measured values for these selected alloys are presented in Fig. 5.19. The black curve in the figure demonstrates the theoretical results published by Vitos *et al.* [8], where they have calculated the temperature and composition dependence of the SFE using an approach very similar to ours. However, their applied approximations and some computational details are different than ours, as they have applied the frozen-core approximation and the SC-LSF scheme. These differences will later be discussed in this section. Our results and Vitos's results agree in the prediction of the direct temperature dependence of the SFE, specially at higher temperatures where both curves increase with almost the same slope. At lower temperatures, including room temperature, the curve calculated by Vitos has greater slope. However, the main difference between these two theoretical results comes from their different SFE-intercept, a constant which shifts the entire curve along the vertical axis,

i.e., SFE-axis. While Vitos has found a positive SFE at room temperature which successfully reproduces the existing experimental values, our calculations result in a negative SFE at room temperature, which is approximately 15 mJ/m^2 lower than the lowest measured value.

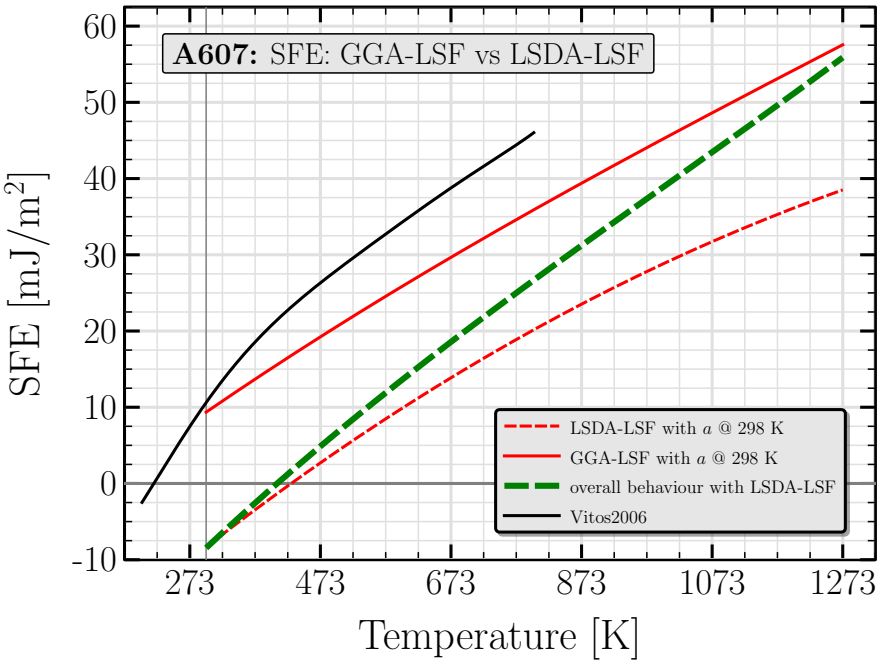

Figure 5.20: Comparison between the SFE results, as the LSF calculations are performed using the LSDA (dashed curves) or the GGA (solid curves) functional. Like in the Fig. 5.18(a), red curves correspond to a set of calculations where the lattice parameter measured at 298 K (25 °C) is utilized in the LSF evaluation.

Vitos *et al.* have applied the GGA functional in order to approximate the exchange-correlation effects in the free energy calculations, as well as in the evaluation of the thermal excitation of the magnetic moments. In fact, the applied self-consistent schema of the LSF calculations evaluates these thermal excitations and the free energy simultaneously, making it impossible to use different exchange-correlation terms in them. Dislike this approach, we calculate the LSF prior to the free-energy calculations, which allows us to chose different computational parameters for these separated tasks. As it was already mentioned in Sec. 5.4.2.1, we use the LSDA functional in the LSF calculations, while utilizing the GGA functional in the free-energy calculations.

In order to find the origin of the difference between our results and Vitos's report, we recalculate the thermal excitation of the magnetic moments using the GGA functional. Our SFE results for both functionals are presented in Fig. 5.20, where the dashed and solid curves indicate the usage of the LSDA and GGA functionals in the LSF calculations, respectively. Compared to graphs if Fig. 5.18(a), we have recalculated the LSF only for the lattice parameter measured at 298 K (25 °C). Using the GGA

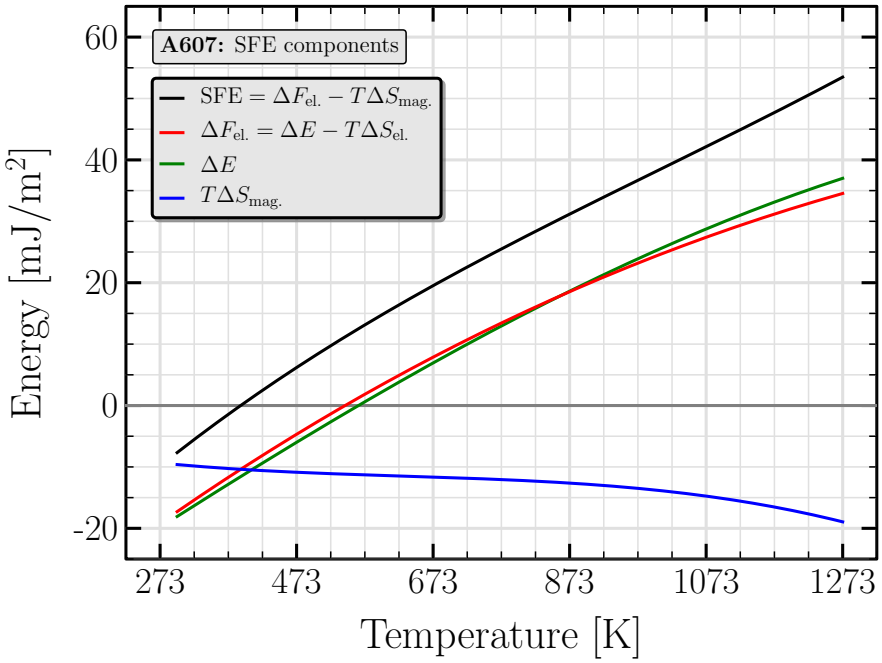

Figure 5.21: The main components of the SFE, calculated for A607. The thermal excitation of the magnetic moments are taken into account using the LSDA exchange-correlation functional in the LSF calculations.

functional in the LSF calculations introduces a significant shift to the entire curve, for almost 20 mJ/m^2 toward the higher values. At room temperature, this results in very good agreement with experimental data and Vitos's report. For higher temperatures, as presented in Fig. 5.18(b), further calculations using relevant lattice parameters in the LSF step are required. However, comparing the enhanced slope of the overall curve to the slope of the curve utilizing a @ 298 K (green dashed curve compared to the red dashed curve in Fig. 5.20), we expect that the same improvement will occur here.

5.4.4 The SFE Components

As a result of the ANNNI model, the SFE is affected by every contribution to the free energies, which are in turn derived by subtracting different entropy contributions from the total energy (see Eqs. 5.6 and 5.7). We already mentioned in Sec. 5.2 that, in our SFE calculations, we consider the magnetic and the electronic contributions to the entropy. In Fig. 5.21, we present three main components of the SFE, *i.e.*, the differences in the total energies

$$\Delta E = E^{\text{hcp}} + 2E^{\text{dhcp}} - 3E^{\text{fcc}}, \tag{5.17}$$

the differences in the electronic free energies

$$\Delta F_{\text{el.}} = \Delta E - T\Delta S_{\text{el.}} = \Delta E - T(S_{\text{el.}}^{\text{hcp}} + 2S_{\text{el.}}^{\text{dhcp}} - 3S_{\text{el.}}^{\text{fcc}}), \tag{5.18}$$

and the differences in the magnetic entropies

$$T\Delta S_{\text{mag.}} = T(S^{\text{hcp}}_{\text{mag.}} + 2S^{\text{dhcp}}_{\text{mag.}} - 3S^{\text{fcc}}_{\text{mag.}}). \tag{5.19}$$

By increasing from -18 mJ/m^2 at 298 K (25 °C) to 37 mJ/m^2 at 1273 K (1000 °C), the total-energy contribution, ΔE plotted in green, governs both the value and the temperature dependence of the SFE. The effect of the electronic-entropy contribution can be estimated by comparing the electronic-free energy, $\Delta F_{\text{el.}}$ plotted in red, to the total energy. The small difference between these two curves indicates the tiny effect of the electronic-entropy contribution on the SFE, which might safely be ignored. The magnetic-entropy contribution, $T\Delta S_{\text{mag.}}$ plotted in blue, changes from -9.6 mJ/m^2 at 298 K (25 °C) to -18.9 mJ/m^2 at 1273 K (1000 °C). By changing less than 3 mJ/m^2 within a range of 600 K, it forms almost a plateau at the first half of the temperature range. Including this term in our calculations, shifts the entire SFE curve toward higher values. Although it slightly increases the slope of the SFE curve, the main influence of the magnetic-entropy contribution must be considered as an improvement in the SFE value rather than in the SFE temperature dependence.

However, the contribution of the magnetic entropy to the free energy is not the only way through which the local magnetic moments influence the final results. As the thermal expansion is taken into account, the local magnetic moments change due to the lattice expansion, resulting in further changes in the total energy. Such changes can appear even when the electronic structure is calculated for the ground state of the system according to 0 K, at which no thermal excitation exists.

In order to investigate this effect, we calculate the ΔE for A607 alloy in two different conditions: 1) in the DLM state at 0 K, where no thermal excitation of the magnetic moments exists, and 2) in the DLM state at finite temperatures, where the thermal excitations of the magnetic moments are taken into account by calculating the fluctuation of spins. The only difference between these two states is the different size of the local magnetic moments, coming from the itinerant nature of electronic magnetism in the Fe–Cr–Ni alloy. For the ground state at 0 K, as it was shown in Fig. 5.7(b), when the lattice parameter falls in the range of $a_{\text{fcc}} = 3.5920$ Å to $a_{\text{fcc}} = 3.6425$ Å, chromium and nickel preserve their nonmagnetic state, while the finite magnetic moments of iron grow with the lattice spacing. Considering the thermal expansion data presented in Fig. 5.10, the mentioned lattice parameter range corresponds to the temperature range of $T = 298$ K to $T = 1273$ K (25 °C to 1000 °C). The thermal excitations of the magnetic moments in this temperature range have been presented in Fig. 5.17. The magnetic moments of iron atoms in this figure are almost equal to their corresponding values calculated at 0 K (see Fig. 5.7(b)) which shows the dominance of the Heisenberg nature of its electron magnetism. However, despite to their nonmagnetic state at 0 K, chromium and nickel exhibit significant spin polarization in this temperature range ($m_{\text{Cr}} \sim 0.6 - 0.7\,\mu_{\text{B}}$ and $m_{\text{Ni}} \sim 0.3\,\mu_{\text{B}}$), showing the dominance of the itinerant nature of their electron magnetism. These excited magnetic moments are responsible for the difference between two curves in Fig. 5.22. Despite this difference, both curves show quite similar temperature dependence of ΔE, emphasizing the higher influence of the lattice expansion compared to the thermal excitations of the magnetic moments.

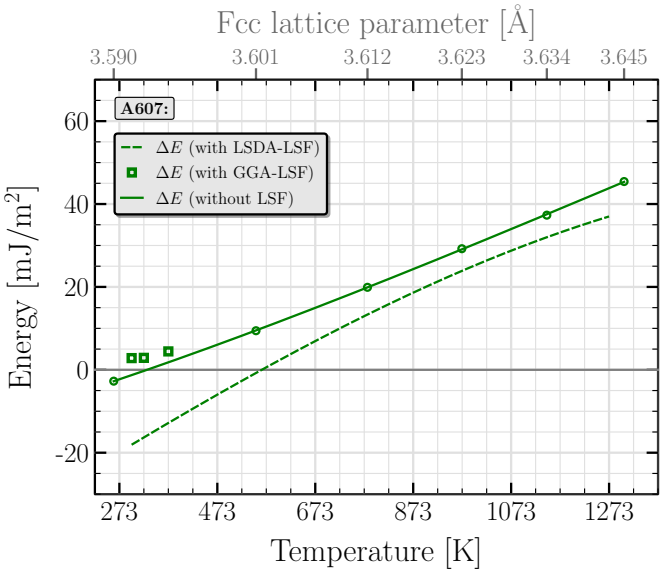

Figure 5.22: The main components of the SFE, calculated for A607. Dashed curve demonstrates our results where the thermal excitation of the magnetic moments are taken into account using the LSDA exchange-correlation functional in the LSF calculations. Square symbols represent the results of a similar approach, where the GGA functional is applied instead of the LSDA in the LSF calculations. Solid curve corresponds to the ground-state calculation at 0 K, using the GGA exchange-correlation functional.

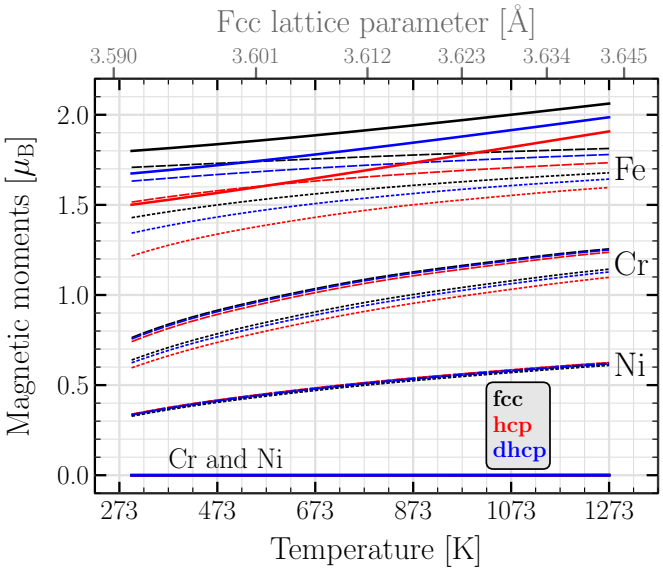

Figure 5.23: The temperature dependence of the magnetic moments, calculated for A607 using different approaches. Calculated using the lattice parameter measured at 298 K (25 °C), dotted and dashed curves demonstrate the thermal excitation of the magnetic moments evaluated using the LSDA and GGA functional in the LSF calculations, respectively. The solid curves, presents the ground-state magnetic moments at 0 K, calculated using the GGA functional for different lattice parameters, which are related to temperature using the thermal expansion date.

When calculating the ΔE, further investigations by looking at the magnetic moments presented in Fig. 5.23, show that the magnetic moments of iron have larger influence compared to those of chromium and nickel. Comparing the results coming from LSDA-LSF and GGA-LSF, respectively dotted and dashed curves in the figure, while nickel magnetic moments are not affected by the exchange-correlation functional, iron and chromium find larger moments as the LSDA functional is replaced by GGA. This increase is more pronounced at lower temperatures, resulting in a larger split between the room-temperature results (see Fig. 5.22). At 0 K, while nickel and chromium remain nonmagnetic regardless of the lattice parameter, the magnetic moments of iron are found larger then their corresponding values using the GGA-LSF. As the volume increases, they grow faster than the GGA-LSF moment grow with temperature, making the split between to class of results larger at higher temperature (volumes). The good agreement between the ΔE values resulted from the GGA-LSF or ground-state calculations (respectively square symbols or solid curve in Fig. 5.22), and the nonmagnetic state of chromium are nonmagnetic in ground-state, suggest that the behavior of the ΔE is mainly characterized by the magnetic moments of iron. On the other hand, concerning these results, we may conclude that, at least for Fe–Cr–Ni alloys, the evaluation of the thermal excitation of the magnetic moments is not the crucial part of the SFE calculation, as the temperature dependence of iron magnetic moments as the main contributers can simply be calculated using the lattice thermal expansion data. This results can provide a solution for applications where an approximation of the SFE is sufficient.

As a summary of the discussion, we present the two main components of the SFE, *i.e.* ΔE, $T\Delta S_{\text{mag.}}$, in Fig. 5.24, where the dashed curves and square symbols indicate the implementation of the LSDA and GGA in the LSF calculations, respectively, and the solid curves correspond to the 0 K ground state calculations. First of all, comparing the SFE's calculated using the LSDA-LSF and the GGA-LSF, we found that the latter results in very good agreement with the experimental results, which is due to the larger magnetic moments resulted from the GGA. All the three classes of results mentioned in the figure emphasize on the fact that, the SFE is dominantly governed by the total energy difference, ΔE, which is in turn highly dependent on the lattice parameter. Moreover, comparing the two magnetic phenomena, the change in the magnetic moments due to a pure lattice expansion, and the change in the magnetic moments due to thermal excitation (magnetic-entropy contribution), we found that they are almost equally importance in the SFE calculations (in the figure, look at the differences of the ΔE curves which are coming from the first phenomenon, and the $T\Delta S_{\text{mag.}}$ curves which are resulted from the second). Considering the significant effort required for evaluation of these thermal excitations, it might be omitted when an approximation of the SFE is sufficient.

These findings about the magnetic effects are clearly contrasting with earlier results published by Vitos *et al.*, where the temperature dependence of the SFE in Fe–Cr–Ni alloys is solely determined by the magnetic-entropy contribution [8]. They have not mentioned whether have included the thermal expansion in their calculations or just

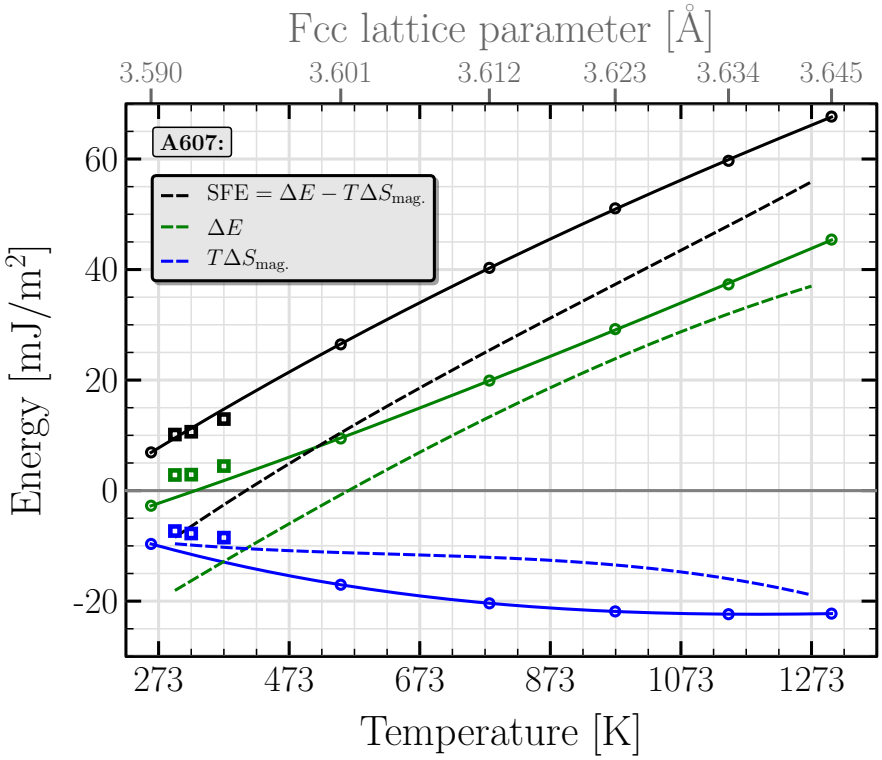

Figure 5.24: The main components of the SFE, calculated for A607. Dashed curves demonstrate our results where the thermal excitation of the magnetic moments are taken into account using the LSDA exchange-correlation functional in the LSF calculations. Square symbols represent the same approach, except the implementation of the GGA functional instead of the LSDA in the LSF calculations. Solid curves correspond to the ground-state calculation at 0 K, using the GGA exchange-correlation functional.

have omitted. However, using the same approach as ours, Reyes-Huamantinco *et al.* have recently calculated the influence of different contributions on the temperature dependence of the SFE for Fe–Mn alloys, where their results are fairly similar to our findings [101]. Our results, together with the publication by Reyes-Huamantinco *et al.*, suggest that in order to find the correct behavior of the SFE versus temperature, the thermal expansion must be taken into account as the crucial effect. Of second order of importance, is the contribution of the magnetic moments in the total energy and also the magnetic-entropy contribution if the free energy. Finally, the electronic entropy may be safely omitted.

5.4.5 The hcp→fcc Driving Force

Now that the free energies are available for both fcc and hcp phases, we can calculate the driving forces for the hcp↔fcc transformations, a pair of parameters demonstrating the tendency of the system to form one phase over the other one. Generally, these

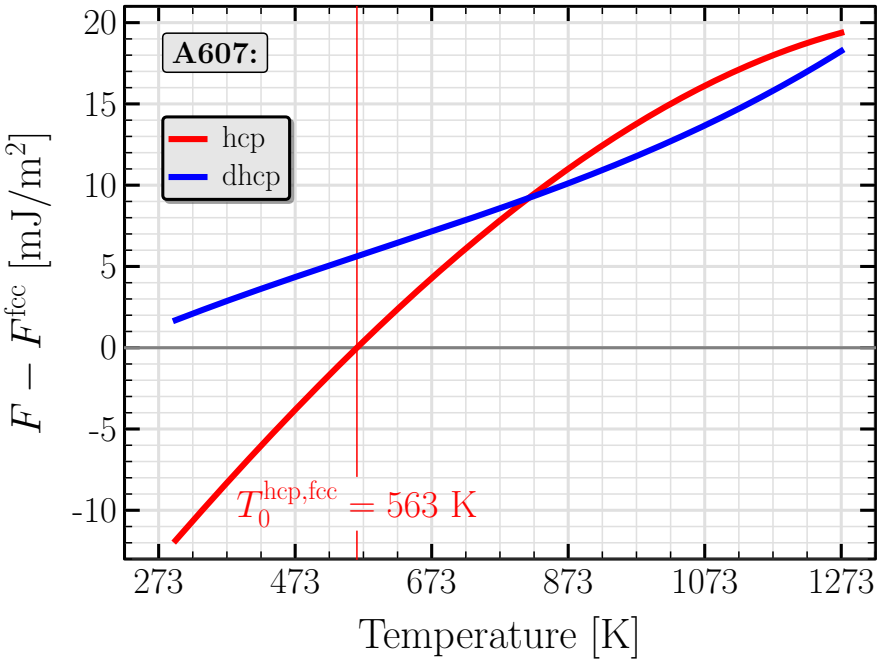

Figure 5.25: The differences between the free energies of the hcp and dhcp phases with respect to the free energy of the fcc phase, calculated for A607 alloy.

parameters are defined as the difference between the free energies of the two phases, with the expression of

$$\Delta F^{\mathrm{fcc}\to\mathrm{hcp}} = F^{\mathrm{fcc}} - F^{\mathrm{hcp}} \tag{5.20}$$

for the forward fcc→hcp transformation, and similarly, with the expression of

$$\Delta F^{\mathrm{hcp}\to\mathrm{fcc}} = F^{\mathrm{hcp}} - F^{\mathrm{fcc}} \tag{5.21}$$

for the reverse fcc→hcp transformation. In Fig. 5.25, we present these differences for both hcp and dhcp phases, *i.e.*, $\Delta F^{\mathrm{hcp}\to\mathrm{fcc}}$ (the red curve) and $\Delta F^{\mathrm{dhcp}\to\mathrm{fcc}} = F^{\mathrm{dhcp}} - F^{\mathrm{fcc}}$ (the blue curve). A positive $\Delta F^{\mathrm{hcp}\to\mathrm{fcc}}$ indicates that the system would prefer the fcc phase over the hcp, and vice versa.

As the temperature changes, the free energies change differently, causing the driving forces to find negative, zero, or positive values. Theoretically, the hcp↔fcc transformations may happen as two phases reach their thermodynamical equilibrium. This equilibrium occurs at a temperature indicated by $T_0^{\mathrm{fcc,hcp}}$, where the free energies of the two phases become equal, and consequently $\Delta F^{\mathrm{hcp}\to\mathrm{fcc}} = \Delta F^{\mathrm{fcc}\to\mathrm{hcp}} = 0$. However, in the real world, due to the existence of non-chemical energy barriers such as interfacial and elastic energy, these transformations occur when their corresponding driving forces find certain positive values [30]. That is why a significant temperature gap is observed between the starting points of the austenite-to-martensite transformation during cooling, and its reversed form, *i.e.*, the martensite-to-austenite transformation during heating.

Table 5.6: Experimental values of $M_s^{\gamma\to\alpha'}$ and $A_s^{\alpha'\to\gamma}$, measured for alloys with chemical composition similar to A607. For accurate composition of other elements, see Appendix B.

Cr	Ni	$M_s^{\gamma\to\alpha'}$		$A_s^{\alpha'\to\gamma}$		notes and reference
[wt%]	[wt%]	[K]	[°C]	[K]	[°C]	
18.00	7.00	193	−80	—	—	Abrassart1973 [11]
20.00	8.00	294	21	—	—	Behjati2011 [13]
18.00	10.00	264	−9	—	—	Behjati2011 [13]
20.00	10.00	261	−12	—	—	Behjati2011 [13]
17.30	11.00	223	−50	—	—	Breedis1964 [14]
18.03	7.94	—	—	813	540	Guy1983 [18]
17.55	7.67	—	—	723	450	Knutsson2008 [19]
18.34	8.53	—	—	710	437	average over five measurements, Tavares2000 [34]
Average:		**247**	**−26**	**727**	**454**	

The experimental measurements for the α'-martensite start temperature, $M_s^{\gamma\to\alpha'}$, and the austenite start temperature, $A_s^{\alpha'\to\gamma}$, are presented in Tab. 5.6 for alloys with chemical composition close to that of A607. The average of values in the table is in good agreement with the empirical formula presented in Eq. 5.12, which estimates the $M_s^{\gamma\to\alpha'}$ temperature about 250 K (−23 °C) for A607. For Fe–18.8wt.%Cr–11.5wt.%Ni, which has slightly higher amount of nickel, Singh has observed that the ϵ and α'-martensites are stable up to 473 K (200 °C) and 673 K (400 °C), respectively [32]. Summarizing these data, and keeping in mind that the hcp ϵ-phase is an intermediate phase in $\gamma \leftrightarrow \alpha'$ transformations, one can conclude that the temperature at which the free energies of ϵ and γ phases become equal, $T_0^{\gamma,\epsilon}$, is somewhere between $M_s^{\gamma\to\alpha'}$ and $A_s^{\alpha'\to\gamma}$. Using the average values in Tab. 5.6, the middle point of the $[M_s^{\gamma\to\alpha'}, A_s^{\alpha'\to\gamma}]$ temperature interval is 487 K (214 °C). Based on our calculations, the free energies of the fcc and hcp phases become equal at $T_0^{\mathrm{fcc,hcp}} = 563$ K (290 °C) (see Fig. 5.25). This value is in adequate agreement with the discussed experimental values, and also with the γ–ϵ equilibrium temperature of 521 K (248 °C), calculated using Thermo-Calc.

5.4.6 Approximations and Approaches

Here we present a systematic study of the influence of different approximations and effects on the SFE results. For brevity and clarity, first we would prefer to explain all terms which appear in plot labels and legends:

- **Analytical LSF:** An approach for evaluating the magnetic free energy, where the magnetic fluctuations are accounted using the Monte-Carlo results (see Subsec. 5.4.2.2) through the Eq. 5.9. This is our default approach of LSF calculations, if nothing is mentioned explicitly.
- **Self-consistent LSF (SC-LSF):** Another approach for evaluating the magnetic free energy, where the magnetic fluctuations are calculated self-consistently, as implemented in the EMTO code.
- **Constant a:** If the label is used without SC-LSF, it means that the DFT calculations in the latest step have been performed with fixed lattice spacing for the entire temperature range, omitting the thermal expansion. However, it must be noted that the thermal expansion has been considered when evaluating the temperature dependence of magnetic moments using the analytical LSF. If the label is used in combination with SC-LSF, it means that the thermal expansion has been omitted completely. The constant lattice spacing is obtained using the experimental fcc lattice parameter measured at 298 K.
- **Variable a:** This label means that the thermal expansion has been taken into account every where in calculations. This is our default method, if nothing is mentioned explicitly.
- **Frozen core:** This label indicates the application of the frozen-core approximation, only in the DFT calculations in the latest step. In this approximation, the core states in a crystal are approximated with their atomic equivalents in an isolated atom, and remain unchanged while valence states are calculated through the self-consistent approach.
- **Soft core:** This label indicates that all electronic states, including core and valence states, have been calculated self-consistently. This is our default choice, if nothing is mentioned explicitly.
- **Electronic entropy ($S_{\text{el.}}$):** This label indicates that the contribution of the electronic entropy has been accounted when calculating the free energy. By default, this contribution is not taken into account, unless explicitly mentioned.

5.4.6.1 The Electronic Entropy

As it was mentioned in Sec. 5.2, the electronic entropy influences the SFE through its contribution to the free energy. In the EMTO code, for a certain temperature, the electronic entropy may be taken into account by implementing the Fermi-Dirac

distribution of electrons. In Fig. 5.26 we present the contribution of the electronic entropy to the temperature dependent SFE, where the dashed or solid lines respectively indicate our final results without or with accounting this effect. As shown in the figure, the electronic entropy has a very small effect, ~ 2 mJ/m^2, when the SFE is calculated using the analytical approach for the LSF. More accurately speaking, including the electronic entropy increases the SFE at the first half of the temperature range, while decreasing it at the other half. For this calculations, the electronic entropy might be safely omitted.

On the other hand, when the SC-LSF approach is applied for evaluating the magnetic excitations, the electronic entropy has more pronounced effect, ~ 5 mJ/m^2 at its maximum, on the final results and increases the SFE everywhere in the temperature range.

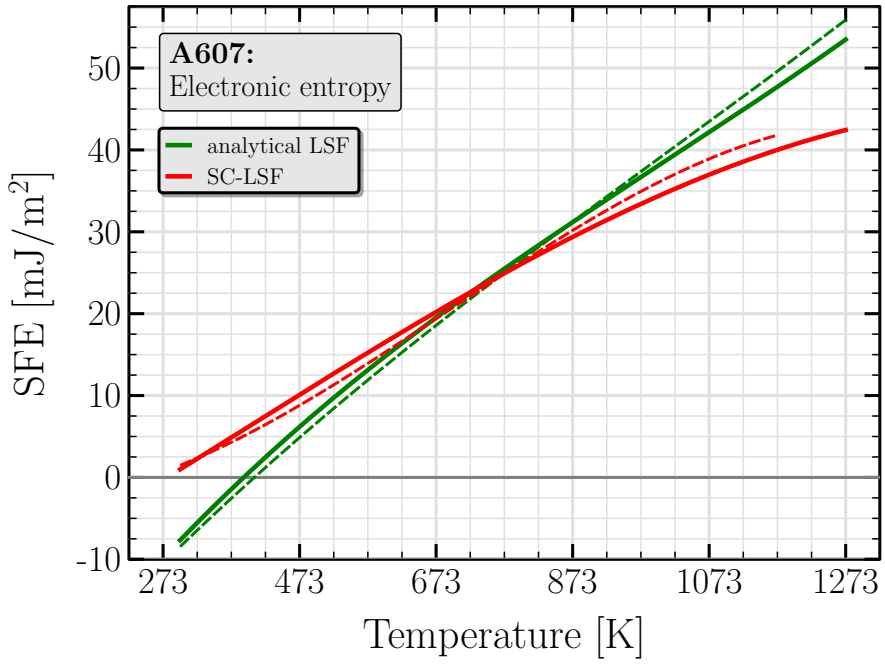

Figure 5.26: Changes introduced in the SFE, as the electronic entropy is taken into account in the free energy calculation. The curves show that the electronic entropy does not significantly affect the final results.

In a similar way, the contribution of the electronic entropy to the temperature dependent DF is presented for two cases: calculations with default settings (Fig. 5.27(a)), and with SC-LSF (Fig. 5.27(b)). Our results show that $T_0^{\text{fcc,hcp}}$ is shifted toward higher temperatures, as the electronic entropy is included in the free-energy calculations. Like the case of the SFE, the shift is larger when the SC-LSF approach is applied.

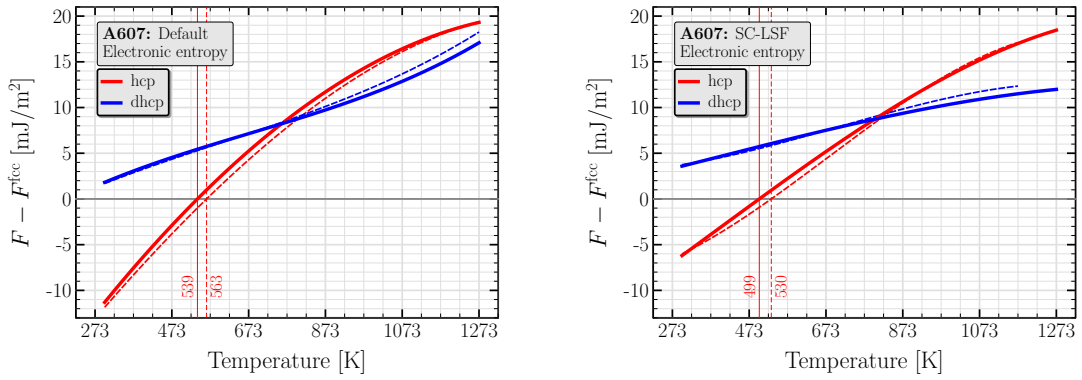

Figure 5.27: Changes introduced in the differences between free energies of hcp and dhcp phases with respect to the free energy of the fcc phase, as the electronic entropy is taken into account. In every plot, the dashed lines indicate the results without accounting the electronic entropy. (a) Calculations with default settings. (b) Calculations with SC-LSF approximation.

5.4.6.2 The Thermal Expansion

In a crystalline solid, lattice vibrations can be excited as a consequence of temperature rise. In most crystals, these excitations result in an increase in the lattice spacing, known as thermal expansion. While the evaluation of expansion coefficients is quite cumbersome, their measurement is rather easy. Thus we use the experimental data in order to include the thermal expansion in our calculations.

The correct physical description of a crystalline material is highly dependent on its lattice spacing. In the first-principle calculations, this fact can be observed by calculating the volume dependence of the main physical properties, like total energy, phase stability, local magnetic moments, density of states, band structures, ... (see Sec. 5.4.1). Of special importance in our study, is the total energy, which is highly dependent on the lattice spacing in all systems, including nonmagnetic materials. Additional to this effect, in the case of magnetic materials, a change in the lattice spacing may alter the local magnetic moments (see Sec. 5.4.1), resulting into further changes in the total energy. Moreover, when the free energies are interested, these changes in the local magnetic moments affect the magnetic entropy (see Eq. 5.9), which in turn influences the free energy (see Eqs. 5.6 and 5.7). These effects emphasizes the importance of the lattice spacing in our SFE evaluations, since the applied ANNNI model is based on the differences of free energies. In our calculations, the thermal expansion is included by providing the relevant lattice parameter according to the temperature at which the SFE is calculated.

In Fig. 5.28, we present the influence of the thermal expansion on the temperature dependence of the SFE in A607 alloy. Moreover, the influence of the thermal expansion on differences between the free energies of three phases is presented in Fig. 5.29. When calculating the LSF using the self-consistent approach, all one needs to enter in the

input file of the EMTO code is the relevant lattice parameter and the temperature. The local magnetic moments, and consequently, the magnetic entropy and the free energy are calculated self-consistently. In this case, if the lattice expansion is omitted, the only difference which remains between a systems configurations at two different temperatures would be its magnetic state. Since the effect of magnetic excitations on the temperature dependence of the SFE is relatively small, it results in a very week temperature dependence of the SFE, which is presented by the small slope of corresponding curves in Figs. 5.28 and 5.29(c).

When calculating the LSF using the analytical approach (see Sec. 5.4.2), the thermal expansion must be considered in two steps, first when calculating the LSF, and second when calculating the total energy (see Sec.5.4.3). However, here we present the influence of the thermal expansion on the second step only, as it has already been taken into account when evaluating the fluctuation of magnetic moments. We found that the thermal expansion is equally important for both soft-care and frozen-core treatments, as it leads to significant increase in the slope of the SFE curve (see Fig. 5.28), or results in big shifts in the fcc–hcp equilibrium temperature, $T_0^{\mathrm{fcc,hcp}}$ (see Figs. 5.29(a) and 5.29(b)). Thus we conclude that the thermal expansion is a crucial effect which must be taken into account in order to understand the correct electronic structure and physical properties of an alloy at finite temperatures, particularly the phase stability, transformation temperatures, and the temperature dependence of the SFE.

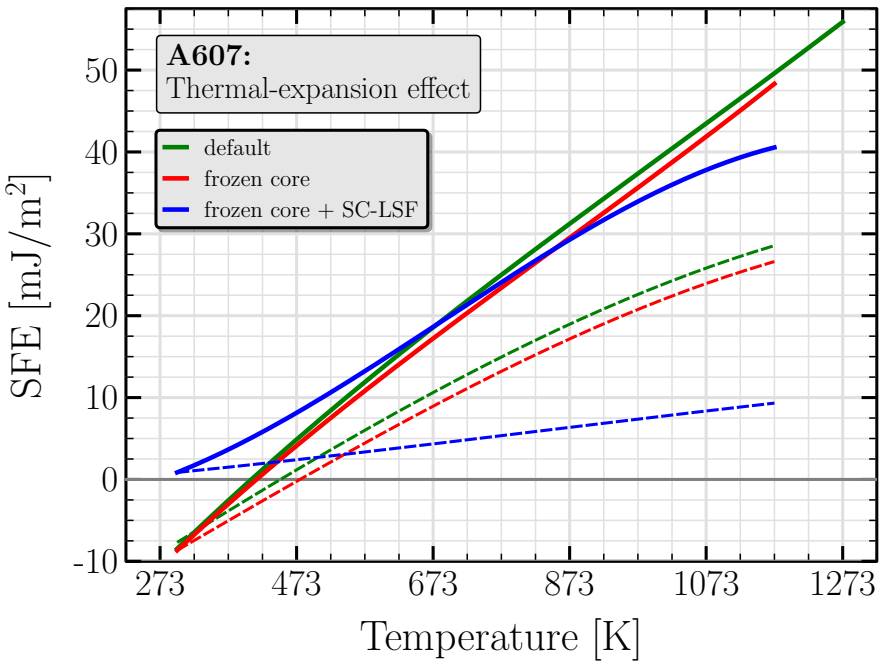

Figure 5.28: Changes introduced in the SFE, as the thermal expansion is taken into account in the free energy calculation. The curves show that the thermal expansion is an essential effect which must be considered in order to find the correct temperature dependence of the SFE.

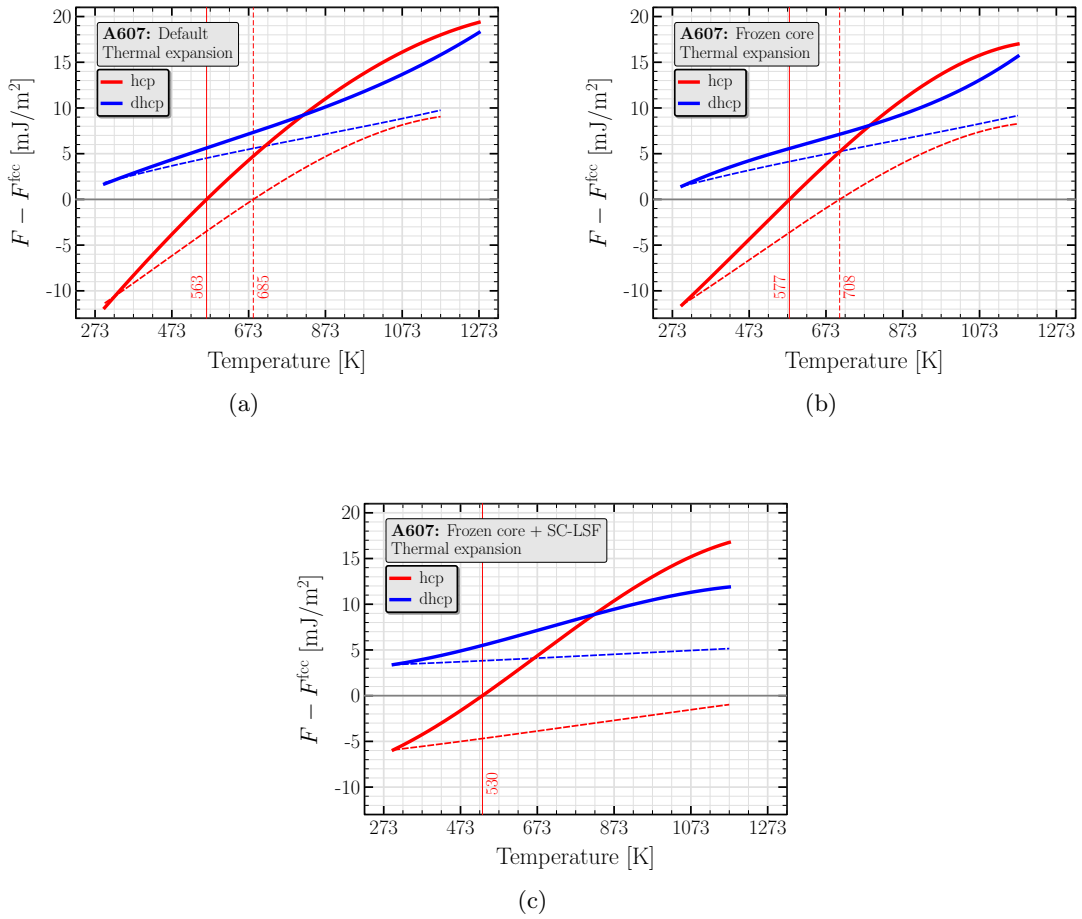

Figure 5.29: Changes introduced in the differences between free energies of hcp and dhcp phases with respect to the free energy of the fcc phase, as the thermal expansion is taken into account. In every plot, the dashed lines indicate the results without accounting the thermal expansion. (a) Calculations with default settings. (b) Calculations with frozen-core approximation. (c) Calculations with frozen-core approximation and SC-LSF.

5.4.6.3 The Frozen-core Approximation

In order to investigate the influence of the frozen-core approximation, we recalculate our results by applying this approximation. The SFE and the free energies are presented in Figs. 5.30 and 5.31, respectively. In all figures, the dashed curves indicate the results of calculation with default settings (soft core, here), while the solid curves show the outputs of with the frozen-core approximation. In summary, these informations, together with the magnetic moments presented in Sec. 5.4.6.3, show that the frozen-core approximation has only a small influence on the final results. On the other hand, we found that the application of this approximation does not improve the performance. Thus, we did not find any motivation for using this approximation.

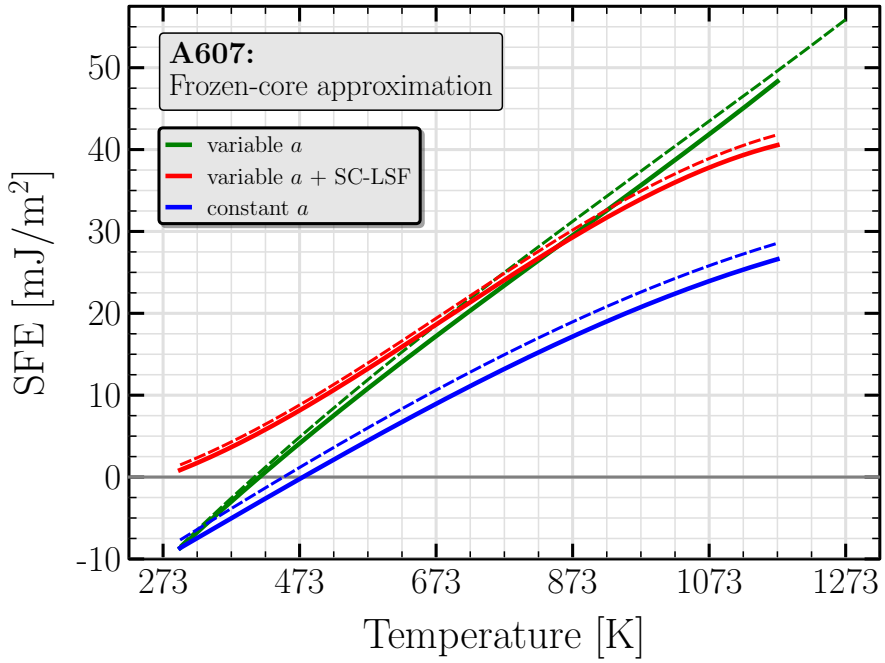

Figure 5.30: The influence of the frozen-core approximation on the SFE, calculated for two systems, including and excluding the thermal expansion (green and red curves, respectively). The curves show just a slight change in the SFE introduced by the approximation.

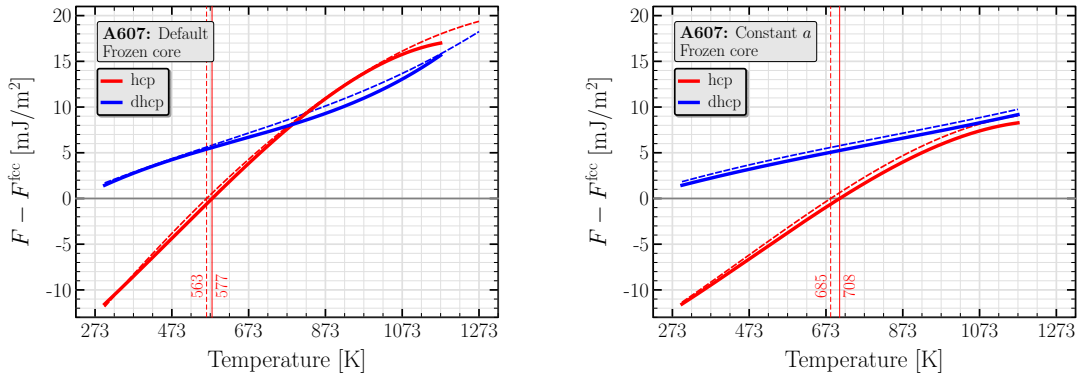

Figure 5.31: Changes introduced in the differences between free energies of hcp and dhcp phases with respect to the free energy of the fcc phase, as the frozen-core approximation is applied. In every plot, the dashed lines indicate the results without the approximation. (a) Calculations with default settings. (b) Calculations with constant spacing.

5.4.6.4 The Self-consistent LSF

As mentioned in Sec. 5.4.2, the thermal excitation of the local magnetic moments can be evaluated by running a Monte-Carlo simulation on a relevant energy map of system, calculated for all phases and elements using DFT techniques. As discussed there, this approach, so-called analytical approach, is able to simulate the itinerant nature of the chromium and nickel electronic magnetism, and hence can calculate the significant temperature-induced grow in the local magnetic moments of these two elements. These magnetic moments can later be used in order to calculate the contribution of the magnetic entropy to the free energy. The other method for accounting this entropy contribution is so-called the self-consistent LSF approach, where the magnetic entropy is obtained using the magnetic moments calculated through the ground-state DFT calculations. In Fig. 5.32, we present a comparison between the temperature dependence of the magnetic moments, calculated using the two mentioned methods.

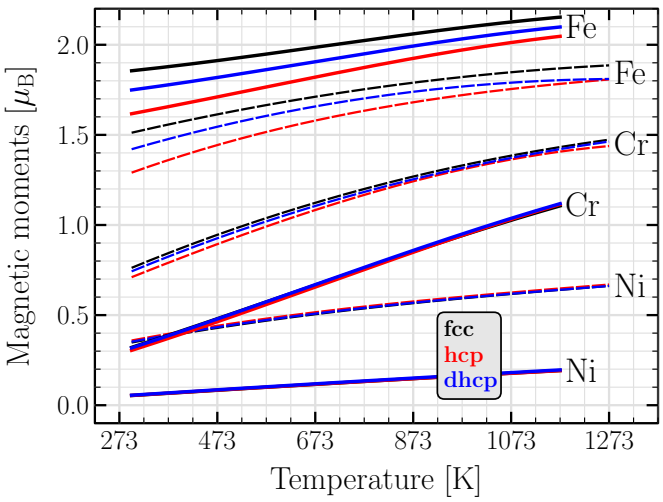

Figure 5.32: The temperature dependence of the magnetic moments, calculated for A607 using different approaches. The Dashed curves demonstrate the thermal excitation of the magnetic moments evaluated using the analytical approach, where the solid curves present the results of SC-LSF approach.

As it is clear in the figure, the SC-LSF approach does not really account the thermal excitation of the magnetic moments of chromium and nickel, so that they maintain their 0 K nonmagnetic state even at high temperatures, resulting to an underestimated magnetic entropy. This underestimation is observed in the temperature dependence of the SFE presented in Fig. 5.33, as the slope of a curve calculated using the SC-LSF (any of dashed curves) is smaller then that of the corresponding curve calculated using the analytical LSF (a solid curve of the same color).

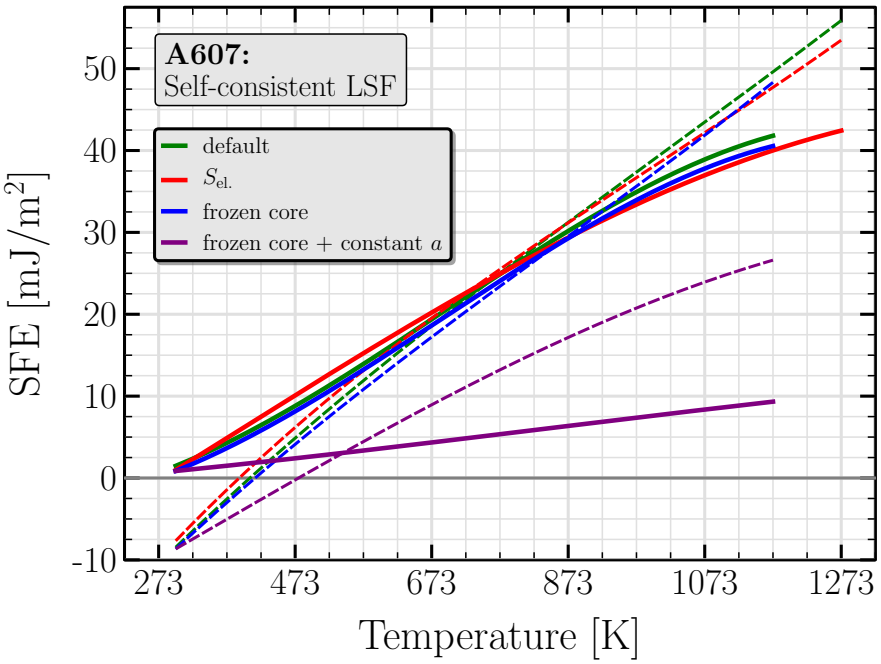

Figure 5.33: Comparison of the SFE's, as the LSF is considered using the analytical (dashed lines) or self-consistent (solid lines) approaches.

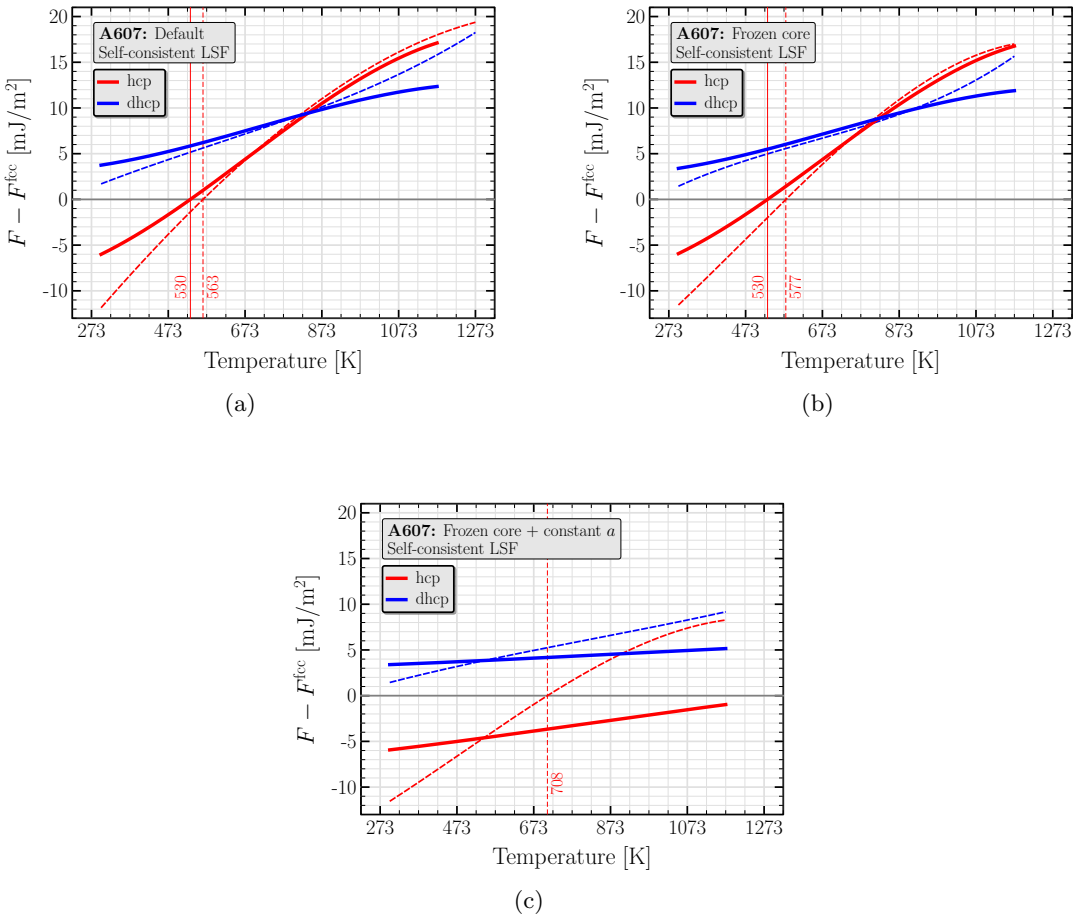

Figure 5.34: Changes introduced in the differences between free energies of hcp and dhcp phases with respect to the free energy of the fcc phase, as the magnetic fluctuations are accounted through the self-consistently. In every plot, the dashed lines indicate the results with analytical LSF evaluation. (a) Calculations with default settings. (b) Calculations with frozen-core approximation. (c) Calculations with frozen-core approximation and constant spacing.

5.4.6.5 The Exchange-correlation Functional

As mentioned before, we use the LSDA exchange-correlation functional when calculating the thermal excitation of magnetic moments (see 5.4.2.1). However, when evaluating the free energies through the constrained DFT calculations, we use the GGA functional (see 5.4.3). Beside this LSDA-LSF+GGA-FE combination, which is our default settings where nothing else mentioned, we have performed tests with other choices like LSDA-LSF+LSDA-FE and GGA-LSF+GGA-FE. The SFE and the driving forces are respectively presented in Fig. 5.35, where dashed and solid curves indicate the LSDA-LSF+GGA-FE and the LSDA-LSF+LSDA-FE combinations, respectively. The SFE curves show that a better agreement with experimental results is obtained when the GGA functional is used in the free energy calculations. This difference is also observed in the driving force curves, presented in Fig. 5.36, where using the LSDA functional underestimates the free energies of the hcp and the dhcp phases with respect to the fcc phase, resulting in wrong phase stabilities in a wide temperature range.

A further investigation on the main components of the SFE, *i.e.* ΔE and $T\Delta S_{\text{mag.}}$ can unveil the origin of the difference. As presented in Fig.5.37, the values of $T\Delta S_{\text{mag.}}$ are found very similar when calculated using the both XC functionals (compare blue curves with blue symbols in the figure). On the other hand, the differences between total energies, ΔE, are strongly dependent of the XC functional applied in the final DFT calculations. In summary, we can say that the best agreement with experimental results is obtained when the GGA functional is applied in both the LSF and the total-energy calculations.

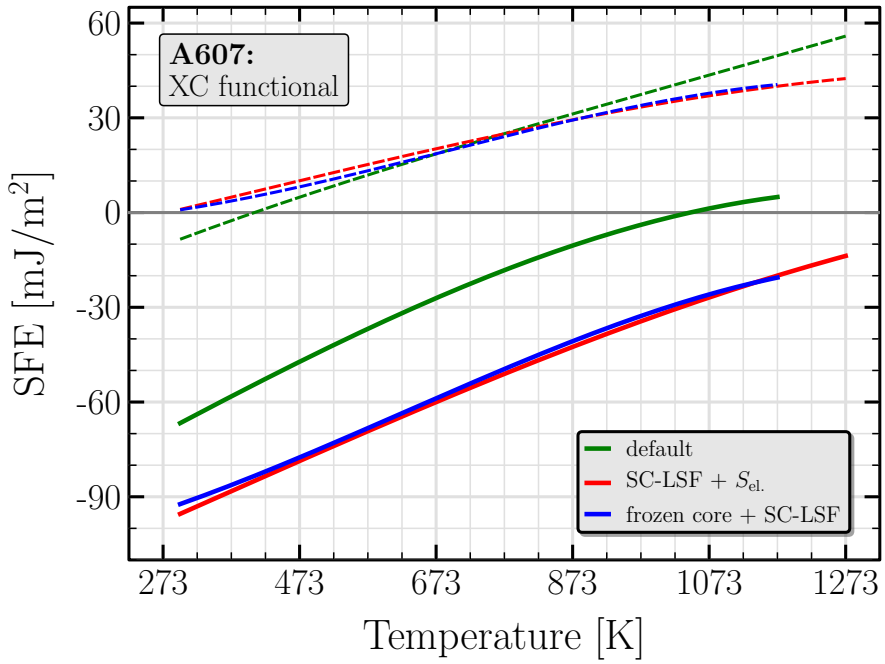

Figure 5.35: The dependence of the SFE on the exchange-correlation functional applied in the free energy calculations. The SFE's evaluated using the GGA (dashed curves) functional agree with experimental results better than those calculated using LSDA (solid curves).

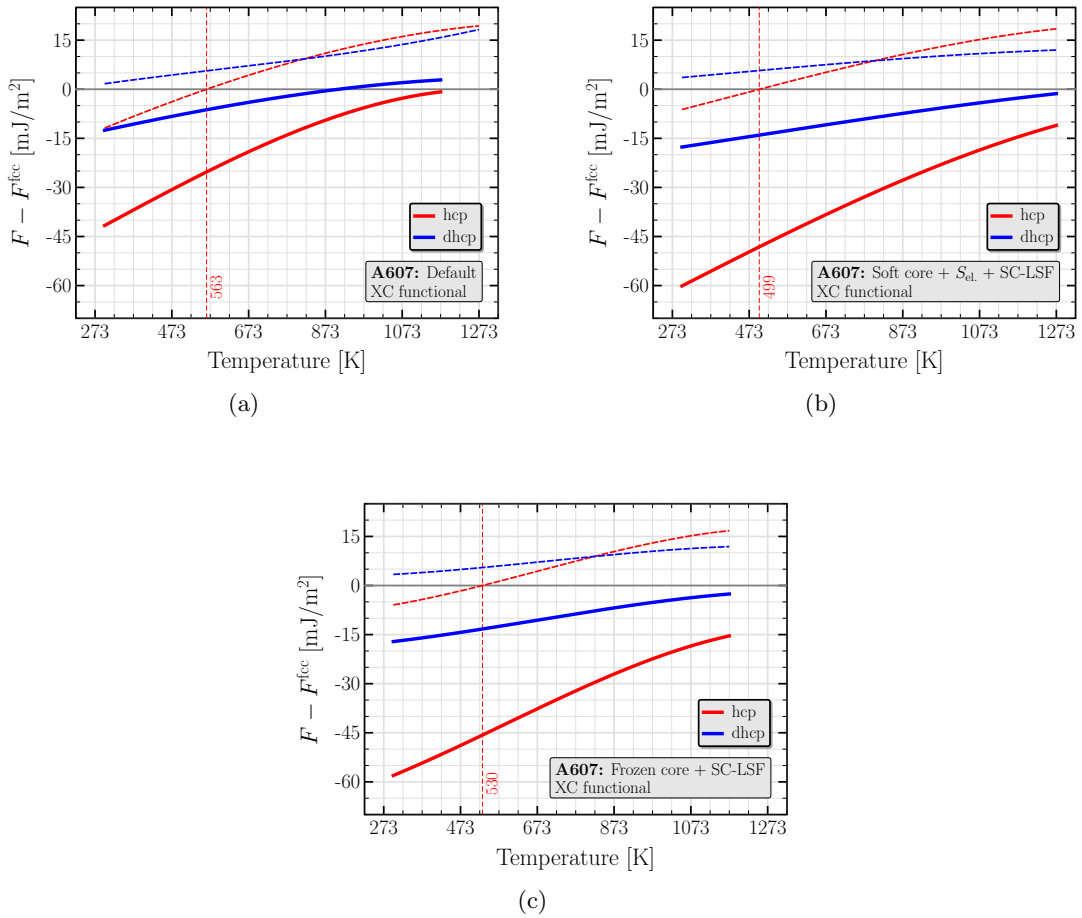

Figure 5.36: Changes introduced in the differences between free energies of hcp and dhcp phases with respect to the free energy of the fcc phase, as the exchange-correlation effects in the final DFT step are approximated using the LSDA functional, instead of the GGA. In every plot, the dashed lines indicate the results with the GGA functional. (a) Calculations with default settings. (b) Calculations including the electronic entropy, using the SC-LSF approach. (c) Calculations with frozen-core approximation and the SC-LSF approach.

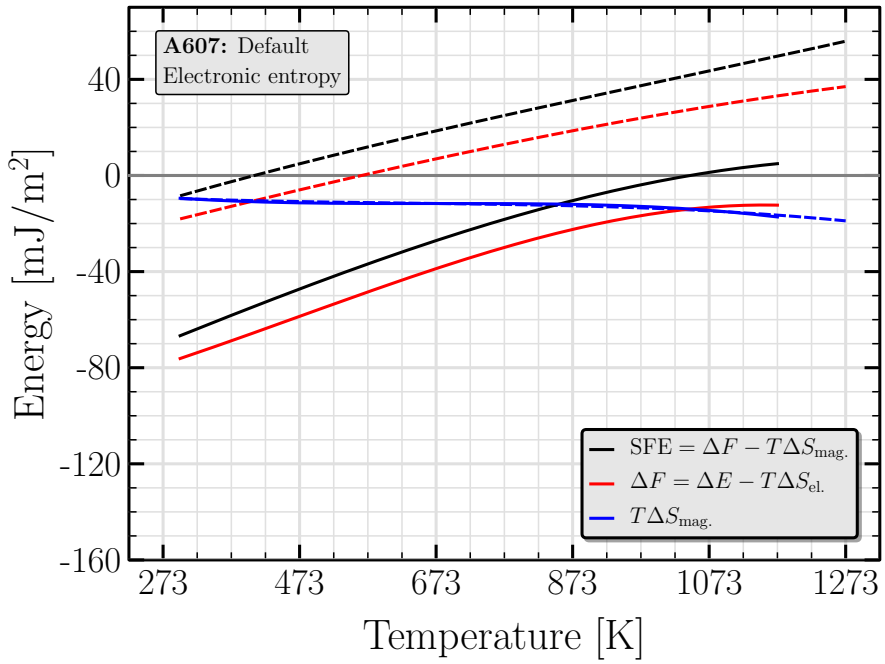

Figure 5.37: The dependence of the components of the SFE on the exchange-correlation functional applied in the calculations. Solid curves, dashed curves, and squared symbols indicate the LSDA-LSF+LSDA-FE, the LSDA-LSF+GGA-FE, and the GGA-LSF+GGA-FE combinations.

5.5 Conclusion

Finally, we would like to make a conclusion out of our results in this chapter. As the results were discussed in intensively, we just keep is as short as possible:

- When calculating the SFE using the ANNNI model, our results for the Fe–Cr–Ni alloy shows that a deviation of maximum ±10% in the value of the screening parameters can still results in accurate enough results.
- Our results show that the frozen-core approximation, compared to the soft-core approach, underestimate the strength of the atomic interactions in the metal, as it results in larger equilibrium volume and smaller bulk modulus. However, the magnetic moments are found very similar in both approaches.
- Our results on the thermal excitation of magnetic moments show that, at 0 K, iron holds significant magnetic moments, while chromium and nickel are nonmagnetic. As temperature rises, all three elements increase their moments. It shows the dominance of the itinerant nature of the electron magnetisms in chromium and nickel, and the dominance of the Heisenberg nature of the electron magnetisms in iron.
- We found that, for the A607 alloy in the range of 298 K–1273 K (25 °C–1000 °C), the SFE almost linearly increases with temperature with the slope of 0.1 $mJ/m^2/K$.
- Our SFE calculations show that, in order to get good agreement between DFT results and experimental data, the thermal excitation of magnetic moments must be calculated using the GGA functional.
- We also found that the thermal lattice expansion is by far the main parameter influencing the temperature dependence of the SFE. The electronic entropy is very small, and hence can be neglected. The main contribution of the magnetic entropy to the SFE is shifting the entire curve toward larger values.
- For the applications where an approximation of the SFE is sufficient, the thermal excitation of the magnetic moments can be skipped, by taking the magnetic moments calculated versus the volume.
- The SC-LSF approach might be used in order to include the thermal excitation of the magnetic moments. While its results are similar to analytical approach, it require less computational efforts.
- We found that the LSDA functional predicts the phase stability of the steel incorrectly, resulting in significantly underestimated SFE. In order to find better agreement with experimental results, we would recommend to use the GGA functional in the entire calculations.

Appendix A

Fourier Expansion in {111}-Plane of the FCC Structure

In this chapter we presents some analytical calculations to find a suitable Fourier expansion for SFE. This expansion will be used to fit the calculated points and find γ-curve.

A General Form of the 2-Dimensional Fourier Expansion with 3-fold Rotational Symmetry

The general form of the Fourier expansion in 2 dimensions is

$$f(x,y) = \sum_{m,n \in Z} C_{mn} e^{i\frac{2\pi x}{a}m} e^{i\frac{2\pi y}{b}n}, \tag{A.1}$$

which a and b are the lattice parameters in direction of x and y axes, respectively. The (111)-plane in the FCC structure has 3-fold rotational symmetry. It means if we rotate any point of this plane around the symmetry axes with an angel of an integer factor of 120°, the function $f(x,y)$ must remain without any change. Suppose a point of coordinates (x,y) in the plane, after rotation we have

$$R_z(\theta) = \begin{pmatrix} \cos(\theta) & -\sin(\theta) \\ \sin(\theta) & \cos(\theta) \end{pmatrix} \tag{A.2}$$

$$R_z(120°) = \begin{pmatrix} -\frac{1}{2} & -\frac{\sqrt{3}}{2} \\ \frac{\sqrt{3}}{2} & -\frac{1}{2} \end{pmatrix} \quad \& \quad R_z(-120°) = \begin{pmatrix} -\frac{1}{2} & \frac{\sqrt{3}}{2} \\ -\frac{\sqrt{3}}{2} & -\frac{1}{2} \end{pmatrix} \tag{A.3}$$

$$\begin{pmatrix} x' \\ y' \end{pmatrix} = R_z(120°) \begin{pmatrix} x \\ y \end{pmatrix} = \begin{pmatrix} -\frac{1}{2}x - \frac{\sqrt{3}}{2}y \\ \frac{\sqrt{3}}{2}x - \frac{1}{2}y \end{pmatrix}, \tag{A.4}$$

$$\begin{pmatrix} x'' \\ y'' \end{pmatrix} = R_z(-120°) \begin{pmatrix} x \\ y \end{pmatrix} = \begin{pmatrix} -\frac{1}{2}x + \frac{\sqrt{3}}{2}y \\ -\frac{\sqrt{3}}{2}x - \frac{1}{2}y \end{pmatrix}. \tag{A.5}$$

A. FOURIER EXPANSION IN {111}-PLANE OF THE FCC STRUCTURE

Now we can replace this values in eq. A.1. Replacing the values of eq. A.4 we will reach

$$\begin{aligned} f(x',y') &= \sum_{m',n'\in Z} C_{m'n'} e^{i\frac{2\pi x'}{a}m'} e^{i\frac{2\pi y'}{b}n'} \\ &= \sum_{m',n'\in Z} C_{m'n'} e^{i\frac{2\pi}{a}(-\frac{1}{2}x-\frac{\sqrt{3}}{2}y)m'} e^{i\frac{2\pi}{b}(\frac{\sqrt{3}}{2}x-\frac{1}{2}y)n'} \end{aligned} \tag{A.6}$$

In FCC plane, we know that $a=\sqrt{3}b$, so we can write

$$f(x',y') = \sum_{m',n'\in Z} C_{m'n'} e^{i\frac{2\pi x}{a}(-\frac{1}{2}m'+\frac{3}{2}n')} e^{i\frac{2\pi y}{b}(-\frac{1}{2}m'-\frac{1}{2}n')}. \tag{A.7}$$

In comparison with eq. A.1, we can find that the necessary condition for equivalence is

$$C_{m'n'} = C_{mn} \quad if \quad \begin{cases} m &= \frac{-m'+3n'}{2} \\ n &= \frac{-m'-n'}{2} \end{cases} \tag{A.8}$$

or in reverse direction

$$C_{m'n'} = C_{mn} \quad if \quad \begin{cases} m' &= -\frac{m+3n}{2} \\ n' &= \frac{m-n}{2} \end{cases} \tag{A.9}$$

Repeating this calculation with the values of eq. A.5, we will reach

$$C_{m''n''} = C_{mn} \quad if \quad \begin{cases} m'' &= -\frac{m-3n}{2} \\ n'' &= -\frac{m+n}{2} \end{cases} \tag{A.10}$$

This conditions necessitate that $m\pm 3n$ and $m\mp n$ be even, which is equal to $m+n=2l$ (l is an integer number). If we continue this series of indexes, we can write

$\theta = 120°$		$\theta = -120°$	
m	n	m	n
$-\frac{m+3n}{2}$	$\frac{m-n}{2}$	$-\frac{m-3n}{2}$	$-\frac{m+n}{2}$
$-\frac{m-3n}{2}$	$-\frac{m+n}{2}$	$-\frac{m+3n}{2}$	$\frac{m-n}{2}$
m	n	m	n

It shows several important facts:

1. These series are finite and after 3 sentence they will repeat. It cause to an ability to cut series in some points with exact symmetry.

2. These series are close. It means that different triplet groups of indexes don't have any common member; or in the other words, each index contributes only in one group.

3. The members of the series for $\theta = 120^\circ$ and $\theta = -120^\circ$ are completely same, only the order of members are different.

Now we have the most general form of a function with 3-fold symmetry in (111)-plane

$$f(x,y) = \sum_{\substack{m,n\in Z \\ m+n=2l}}{}' C_{mn}\Big\{ \quad e^{i\frac{2\pi x}{a}m}e^{i\frac{2\pi y}{b}n} \tag{A.11}$$
$$+ \quad e^{i\frac{2\pi x}{a}(-\frac{m+3n}{2})}e^{i\frac{2\pi y}{b}(\frac{m-n}{2})}$$
$$+ \quad e^{i\frac{2\pi x}{a}(-\frac{m-3n}{2})}e^{i\frac{2\pi y}{b}(-\frac{m+n}{2})}\Big\}$$

We have used the $\sum'$ instead of the $\sum$ in this formula. $\sum'$ means the summation will not do over the all of the integer numbers, but, summation will only do over the integer numbers which have not been manifested in the previous terms. We will use this sign in the same meaning in the following of this text.

B Additional Reflective Symmetry Respect to X-axes

Another restriction for the function $f(x,y)$ in the FCC structure (111)-plane is the reflective symmetry respect to x axes. In the other word, if we replace the y with $-y$, the function $f(x,y)$ must not senses any change. So we can write

$$f(x,y) = f(x,-y) \tag{A.12}$$

which cause to

$$C_{m,-n} = C_{m,n} \tag{A.13}$$

and leads to

$$f(x,y) = \sum_{\substack{m,n\in Z \\ n\geq 0 \\ m+n=2l}}{}' C_{mn}\Big\{ \quad e^{i\frac{2\pi x}{a}m}\cos(\frac{2\pi y}{b}n) \tag{A.14}$$
$$+ \quad e^{i\frac{2\pi x}{a}(-\frac{m+3n}{2})}\cos(\frac{2\pi y}{b}\frac{m-n}{2})$$
$$+ \quad e^{i\frac{2\pi x}{a}(-\frac{m-3n}{2})}\cos(\frac{2\pi y}{b}\frac{m+n}{2})\Big\}$$

C Additional Condition to Guarantee the Real Values for $f(x, y)$

Now there is only one restriction: "$f(x, y)$ must be real". C_{mn}'s are generally complex and we can write

$$C_{mn} = p - iq, \qquad p, q \in R \tag{A.15}$$

Replacing this form in eq. A.15, and using the Euler's formula we can find that the necessary condition for reality of $f(x, y)$ is

$$C_{-m,n} = C^*_{m,n}. \tag{A.16}$$

This relation gives $C_{0n} = C^*_{0n}$, and it means that C_{0n} is real, so we can derive that $q_{0n} = 0$.

Now we reach the form

$$\begin{aligned} f(x,y) \;=\; & \sum_{\substack{n\in Z\\ n\geq 0\\ n=2l}}{}' \Bigg\{ \\ & p_{0n}\cos(\frac{2\pi y}{b}n) \\ +\; & 2p_{0n}\cos(\frac{2\pi x}{a}\frac{3n}{2})\cos(\frac{2\pi y}{b}\frac{n}{2})\Bigg\} \\ +\; & \sum_{\substack{m,n\in Z\\ m>0\\ n\geq 0\\ m+n=2l}}{}' \Bigg\{ \\ & \Big(p_{mn}\cos(\frac{2\pi x}{a}m) + q_{mn}\sin(\frac{2\pi x}{a}m)\Big)\cos(\frac{2\pi y}{b}n) \\ +\; & \Big(p_{mn}\cos(\frac{2\pi x}{a}\frac{m+3n}{2}) + q_{mn}\sin(\frac{2\pi x}{a}\frac{m+3n}{2})\Big)\cos(\frac{2\pi y}{b}\frac{m-n}{2}) \\ +\; & \Big(p_{mn}\cos(\frac{2\pi x}{a}\frac{m-3n}{2}) + q_{mn}\sin(\frac{2\pi x}{a}\frac{m-3n}{2})\Big)\cos(\frac{2\pi y}{b}\frac{m+n}{2})\Bigg\} \end{aligned} \tag{A.17}$$

We can write above relation in the terms of constants p and q

$$
\begin{aligned}
f(x,y) = \sum_{\substack{n\in Z \\ n\geq 0 \\ n=2l}}{}' \Bigg\{ \quad & p_{0n} \quad \left[\cos(\frac{2\pi y}{b} n) + 2\cos(\frac{2\pi x}{a}\frac{3n}{2})\cos(\frac{2\pi y}{b}\frac{n}{2}) \right] \Bigg\} \\
& \sum_{\substack{m,n\in Z \\ m>0 \\ n\geq 0 \\ m+n=2l}}{}' \Bigg\{ \\
& \qquad p_{mn} \quad \Bigg[\cos(\frac{2\pi x}{a} m)\cos(\frac{2\pi y}{b} n) \\
& \qquad\qquad + \ \cos(\frac{2\pi x}{a}\frac{m+3n}{2})\cos(\frac{2\pi y}{b}\frac{m-n}{2}) \\
& \qquad\qquad + \ \cos(\frac{2\pi x}{a}\frac{m-3n}{2})\cos(\frac{2\pi y}{b}\frac{m+n}{2}) \Bigg] \\
& \quad + \quad q_{mn} \quad \Bigg[\sin(\frac{2\pi x}{a} m)\cos(\frac{2\pi y}{b} n) \\
& \qquad\qquad + \ \sin(\frac{2\pi x}{a}\frac{m+3n}{2})\cos(\frac{2\pi y}{b}\frac{m-n}{2}) \\
& \qquad\qquad + \ \sin(\frac{2\pi x}{a}\frac{m-3n}{2})\cos(\frac{2\pi y}{b}\frac{m+n}{2}) \Bigg] \Bigg\}
\end{aligned}
\tag{A.18}
$$

D Suitable Fourier Expansion of $f(x,y)$ for Our Works

Regarding to the best results of fitting of FP-LAPW data to the Fourier expansion, we have found that a suitable approximation with a small cutoff of 2 can be employed

instead of infinite expansion. We can write this series in the form

$$
\begin{aligned}
f(x,y) = \;& p_{00} \\
+ \;& p_{02} \quad \Big[+ \cos(\frac{4\pi y}{b}) + 2\cos(\frac{6\pi x}{a})\cos(\frac{2\pi y}{b}) \Big] \\
+ \;& p_{11} \quad \Big[+ \cos(\frac{4\pi x}{a}) + 2\cos(\frac{2\pi x}{a})\cos(\frac{2\pi y}{b}) \Big] \\
+ \;& p_{20} \quad \Big[+ \cos(\frac{4\pi x}{a}) + 2\cos(\frac{2\pi x}{a})\cos(\frac{2\pi y}{b}) \Big] \\
+ \;& p_{22} \quad \Big[+ \cos(\frac{8\pi x}{a}) + 2\cos(\frac{4\pi x}{a})\cos(\frac{4\pi y}{b}) \Big] \\
+ \;& q_{11} \quad \Big[- \sin(\frac{4\pi x}{a}) + 2\sin(\frac{2\pi x}{a})\cos(\frac{2\pi y}{b}) \Big] \\
+ \;& q_{20} \quad \Big[+ \sin(\frac{4\pi x}{a}) - 2\sin(\frac{2\pi x}{a})\cos(\frac{2\pi y}{b}) \Big] \\
+ \;& q_{22} \quad \Big[- \sin(\frac{8\pi x}{a}) + 2\sin(\frac{4\pi x}{a})\cos(\frac{4\pi y}{b}) \Big].
\end{aligned}
\tag{A.19}
$$

We can rewrite this relation in the term of the trigonometry parts

$$
\begin{aligned}
f(x,y) \;=\; & p_{00} + p_{02}\cos(\frac{4\pi y}{b}) + 2p_{02}\cos(\frac{6\pi x}{a})\cos(\frac{2\pi y}{b}) \\
+ \;& (p_{11}+p_{20})\cos(\frac{4\pi x}{a}) + p_{22}\cos(\frac{8\pi x}{a}) \\
+ \;& (q_{20}-q_{11})\sin(\frac{4\pi x}{a}) - q_{22}\sin(\frac{8\pi x}{a}) \\
+ \;& 2(p_{11}+p_{20})\cos(\frac{2\pi x}{a})\cos(\frac{2\pi y}{b}) \\
+ \;& 2(q_{11}-q_{20})\sin(\frac{2\pi x}{a})\cos(\frac{2\pi y}{b}) \\
+ \;& 2p_{22}\cos(\frac{4\pi x}{a})\cos(\frac{4\pi y}{b}) \\
+ \;& 2q_{22}\sin(\frac{4\pi x}{a})\cos(\frac{4\pi y}{b})
\end{aligned}
\tag{A.20}
$$

Appendix B

Experimental Data

Table B.1: Abrassart1973 [11]: Fe-Cr-Ni

name	method	Fe	Cr	Ni	C	Al	Si	Mn	Nb	Mo	M_s	T	SFE	M_d
Steel 1	exp	74.82	18	7	0.18	—	—	—	—	—	193.15 ± 5	287.55	17.7	$353.15 < x < 363.15$
Steel 1	exp	74.82	18	7	0.18	—	—	—	—	—	—	288.85	16.5	—
Steel 1	exp	74.82	18	7	0.18	—	—	—	—	—	—	288.85	19.8	—
Steel 1	exp	74.82	18	7	0.18	—	—	—	—	—	—	289.55	22.8	—
Steel 1	exp	74.82	18	7	0.18	—	—	—	—	—	—	291.75	18.3	—
Steel 1	exp	74.82	18	7	0.18	—	—	—	—	—	—	292.65	12.5	—
Steel 1	exp	74.82	18	7	0.18	—	—	—	—	—	—	292.95	21.3	—
Steel 1	exp	74.82	18	7	0.18	—	—	—	—	—	—	293.15	24.4	—
Steel 1	exp	74.82	18	7	0.18	—	—	—	—	—	—	293.45	17.3	—
Steel 1	exp	74.82	18	7	0.18	—	—	—	—	—	—	293.65	22.6	—
Steel 1	exp	74.82	18	7	0.18	—	—	—	—	—	—	296.75	23.5	—
Steel 1	exp	74.82	18	7	0.18	—	—	—	—	—	—	297.45	19	—
Steel 1	exp	74.82	18	7	0.18	—	—	—	—	—	—	383.55	31.9	—
Steel 1	exp	74.82	18	7	0.18	—	—	—	—	—	—	385.95	33.4	—
Steel 1	exp	74.82	18	7	0.18	—	—	—	—	—	—	386.35	30.4	—
Steel 1	exp	74.82	18	7	0.18	—	—	—	—	—	—	387.15	32.1	—
Steel 1	exp	74.82	18	7	0.18	—	—	—	—	—	—	389.65	27.4	—
Steel 1	exp	74.82	18	7	0.18	—	—	—	—	—	—	393.95	19.8	—
Steel 1	exp	74.82	18	7	0.18	—	—	—	—	—	—	393.95	20.7	—
Steel 1	exp	74.82	18	7	0.18	—	—	—	—	—	—	396.35	29.6	—
Steel 1	exp	74.82	18	7	0.18	—	—	—	—	—	—	398.75	26.3	—
Steel 1	exp	74.82	18	7	0.18	—	—	—	—	—	—	398.85	31.8	—
Steel 1	exp	74.82	18	7	0.18	—	—	—	—	—	—	399.05	32.9	—
Steel 1	exp	74.82	18	7	0.18	—	—	—	—	—	—	400.35	28.9	—

Continued on next page

Table B.1 – continued from previous page

name	method	Fe	Cr	Ni	C	Al	Si	Mn	Nb	Mo	M_s	T	SFE	M_d
Steel 1	exp	74.82	18	7	0.18	—	—	—	—	—	—	400.45	30.1	—
Steel 1	exp	74.82	18	7	0.18	—	—	—	—	—	—	402.95	32.1	—
Steel 1	exp	74.82	18	7	0.18	—	—	—	—	—	—	404.65	30.2	—
Steel 1	exp	74.82	18	7	0.18	—	—	—	—	—	—	472.55	51.2	—
Steel 1	exp	74.82	18	7	0.18	—	—	—	—	—	—	472.65	49.8	—
Steel 1	exp	74.82	18	7	0.18	—	—	—	—	—	—	473.85	24.9	—
Steel 1	exp	74.82	18	7	0.18	—	—	—	—	—	—	475.35	28.5	—
Steel 1	exp	74.82	18	7	0.18	—	—	—	—	—	—	476.15	50.5	—
Steel 1	exp	74.82	18	7	0.18	—	—	—	—	—	—	493.05	43.7	—
Steel 1	exp	74.82	18	7	0.18	—	—	—	—	—	—	493.05	43.7	—
Steel 1	exp	74.82	18	7	0.18	—	—	—	—	—	—	497.15	43.6	—
Steel 1	exp	74.82	18	7	0.18	—	—	—	—	—	—	498.25	45.6	—
Steel 1	exp	74.82	18	7	0.18	—	—	—	—	—	—	498.25	45.6	—
Steel 1	exp	74.82	18	7	0.18	—	—	—	—	—	—	505.85	49.4	—
Steel 1	exp	74.82	18	7	0.18	—	—	—	—	—	—	505.85	49.4	—
Steel 1	exp	74.82	18	7	0.18	—	—	—	—	—	—	510.05	49.5	—
Steel 1	exp	74.82	18	7	0.18	—	—	—	—	—	—	597.25	49.1	—
Steel 1	exp	74.82	18	7	0.18	—	—	—	—	—	—	597.25	49.1	—
Steel 1	exp	74.82	18	7	0.18	—	—	—	—	—	—	597.65	41.2	—
Steel 1	exp	74.82	18	7	0.18	—	—	—	—	—	—	597.85	37.7	—
Steel 1	exp	74.82	18	7	0.18	—	—	—	—	—	—	597.95	50.4	—
Steel 1	exp	74.82	18	7	0.18	—	—	—	—	—	—	601.55	49.6	—
Steel 1	exp	74.82	18	7	0.18	—	—	—	—	—	—	602.15	48.1	—
Steel 1	exp	74.82	18	7	0.18	—	—	—	—	—	—	604.95	50.5	—

Continued on next page

Table B.1 – continued from previous page

name	method	Fe	Cr	Ni	C	Al	Si	Mn	Nb	Mo	M_s	T	SFE	M_d
Steel 1	exp	74.82	18	7	0.18	—	—	—	—	—	—	604.95	50.5	—
Steel 1	exp	74.82	18	7	0.18	—	—	—	—	—	—	605.05	49.7	—
Steel 1	exp	74.82	18	7	0.18	—	—	—	—	—	—	605.85	49	—
Steel 1	exp	74.82	18	7	0.18	—	—	—	—	—	—	610.35	49.6	—
Steel 1	exp	74.82	18	7	0.18	—	—	—	—	—	—	610.45	50.8	—
Steel 1	exp	74.82	18	7	0.18	—	—	—	—	—	—	610.85	48.6	—
Steel 2	exp	75.84	15.5	4.2	0.13	0.17	0.16	1.2	0.1	2.7	$273.15 < x < 283.15 \pm 5$	—	—	393.15

Table B.2: Bampton1978 [12]: Fe-Cr-Ni

name	method	Fe	Cr	Ni	C	Si	Mn	Mo	T	SFE
16/14	exp	69.67	16.2	14	0.02	0.01	0.08	0.02	298.15	23 ± 5
16/22	exp	62.9	16.21	20.77	0.01	0.01	0.08	0.02	298.15	31 ± 5
21/14	exp	64.97	21.1	13.8	0.02	0.01	0.08	0.02	298.15	18 ± 4
21/22	exp	56.89	21	22	0.01	0.01	0.07	0.02	298.15	33 ± 5
26/22	exp	52.96	25.85	21.07	0.01	0.01	0.08	0.02	298.15	35 ± 5

Table B.3: Behjati2011 [13]: Fe-Cr-Ni

name	method	Fe	Cr	Ni	C	N	O	Si	P	S	Mn	Mo	M_s	T	$DF^{\epsilon\rightarrow\gamma}$	T	SFE	$T_0^{\gamma,\alpha'}$	T	$DF^{\alpha'\rightarrow\gamma}$
16/12	exp	71.9942	16	12	0.0004	0.001	0.001	0.002	0.0001	0.0001	0.001	0.0002	—	—	—	—	—	—	77.1	891.6
16/12	exp	71.9942	16	12	0.0004	0.001	0.001	0.002	0.0001	0.0001	0.001	0.0002	—	—	—	—	—	—	123.3	947.9
16/12	exp	71.9942	16	12	0.0004	0.001	0.001	0.002	0.0001	0.0001	0.001	0.0002	—	—	—	—	—	—	203.1	1029.1
16/12	exp	71.9942	16	12	0.0004	0.001	0.001	0.002	0.0001	0.0001	0.001	0.0002	—	—	—	—	—	—	213.2	1110
16/12	exp	71.9942	16	12	0.0004	0.001	0.001	0.002	0.0001	0.0001	0.001	0.0002	—	—	—	—	—	—	223.2	1155.9
16/12	exp	71.9942	16	12	0.0004	0.001	0.001	0.002	0.0001	0.0001	0.001	0.0002	—	—	—	—	—	—	232.9	1172
20/10	exp	69.9942	20	10	0.0004	0.001	0.001	0.002	0.0001	0.0001	0.001	0.0002	—	—	—	—	—	—	4.1	645.8
20/10	exp	69.9942	20	10	0.0004	0.001	0.001	0.002	0.0001	0.0001	0.001	0.0002	—	—	—	—	—	—	77.2	689.6
20/10	exp	69.9942	20	10	0.0004	0.001	0.001	0.002	0.0001	0.0001	0.001	0.0002	—	—	—	—	—	—	203.1	778.1
20/10	exp	69.9942	20	10	0.0004	0.001	0.001	0.002	0.0001	0.0001	0.001	0.0002	—	—	—	—	—	—	233.2	857.4
20/10	exp	69.9942	20	10	0.0004	0.001	0.001	0.002	0.0001	0.0001	0.001	0.0002	—	—	—	—	—	—	253	903.8
20/10	exp	69.9942	20	10	0.0004	0.001	0.001	0.002	0.0001	0.0001	0.001	0.0002	—	—	—	—	—	—	293.2	921
20/12	exp	67.9942	20	12	0.0004	0.001	0.001	0.002	0.0001	0.0001	0.001	0.0002	—	—	—	—	—	—	4.1	532.5
20/12	exp	67.9942	20	12	0.0004	0.001	0.001	0.002	0.0001	0.0001	0.001	0.0002	—	—	—	—	—	—	133	576.8
20/12	exp	67.9942	20	12	0.0004	0.001	0.001	0.002	0.0001	0.0001	0.001	0.0002	—	—	—	—	—	—	203.1	692
20/12	exp	67.9942	20	12	0.0004	0.001	0.001	0.002	0.0001	0.0001	0.001	0.0002	—	—	—	—	—	—	223.2	720
20/08	exp	71.9942	20	8	0.0004	0.001	0.001	0.002	0.0001	0.0001	0.001	0.0002	294	294	2346	293	16 ± 1.9	634	294	1130
20/08	exp	71.9942	20	8	0.0004	0.001	0.001	0.002	0.0001	0.0001	0.001	0.0002	—	—	—	294	16	—	—	—
18/10	exp	71.9942	18	10	0.0004	0.001	0.001	0.002	0.0001	0.0001	0.001	0.0002	264	294	2379	293	22 ± 2.3	587	294	1130
18/10	exp	71.9942	18	10	0.0004	0.001	0.001	0.002	0.0001	0.0001	0.001	0.0002	—	—	—	264	20	—	—	—
20/10	exp	69.9942	20	10	0.0004	0.001	0.001	0.002	0.0001	0.0001	0.001	0.0002	261	294	2426	293	20 ± 2.1	550	294	921
20/10	exp	69.9942	20	10	0.0004	0.001	0.001	0.002	0.0001	0.0001	0.001	0.0002	—	—	—	261	18	—	—	—
16/12	exp	71.9942	16	12	0.0004	0.001	0.001	0.002	0.0001	0.0001	0.001	0.0002	231	294	2432	293	28 ± 2.9	552	294	1172
16/12	exp	71.9942	16	12	0.0004	0.001	0.001	0.002	0.0001	0.0001	0.001	0.0002	—	—	—	231	24	—	—	—
18/12	exp	69.9942	18	12	0.0004	0.001	0.001	0.002	0.0001	0.0001	0.001	0.0002	220	294	2479	293	26 ± 2.9	510	294	950
18/12	exp	69.9942	18	12	0.0004	0.001	0.001	0.002	0.0001	0.0001	0.001	0.0002	—	—	—	220	21	—	—	—
20/12	exp	67.9942	20	12	0.0004	0.001	0.001	0.002	0.0001	0.0001	0.001	0.0002	216	294	2508	293	24 ± 2.7	464	294	720
20/12	exp	67.9942	20	12	0.0004	0.001	0.001	0.002	0.0001	0.0001	0.001	0.0002	—	—	—	216	19	—	—	—

Table B.4: Breedis1964 [14]: Fe-Cr-Ni

name	method	Fe	Cr	Ni	M_s	T	SFE
Fe-19Cr-11Ni	exp	69.5	19.3	11.2	225.15	298.15	12.7
Fe-17Cr-11Ni	exp	71.7	17.3	11	223.15	298.15	17.7
Fe-16Cr-12Ni	exp	71.9	16	12.1	214.15	298.15	22.2
Fe-13Cr-14Ni	exp	72.8	13	14.2	183.15	298.15	33.1
Fe-11.5Cr-15Ni	exp	73.4	11.5	15.1	173.15	—	—
Fe-11.5Cr-16Ni	exp	72.4	11.5	16.1	$77.15 < x < 143.15$	—	—
Fe-10Cr-16Ni	exp	73.4	10.4	16.2	208.15	298.15	42.6
Fe-10Cr-16Ni	exp	73.4	10.4	16.2	$77.15 < x < 143.15$	—	—
Fe-7.5Cr-19Ni	exp	73.2	7.5	19.3	238.15	—	—
Fe-5Cr-23Ni	exp	71.9	4.8	23.3	258.15	—	—
Fe-3Cr-27Ni	exp	70.2	2.8	27	$77.15 < x < 143.15$	—	—
Fe-2Cr-30Ni	exp	68	1.9	30.1	$77.15 < x < 143.15$	—	—
Fe-33Ni	exp	66.9	—	33.1	173.15	—	—

Table B.5: Breedis1971 [15]: Fe-Cr-Ni

name	method	Fe	Cr	Ni	T	SFE
1	exp	69.5063	19.2551	11.2387	300	13
Continued on next page						

Table B.5 – continued from previous page

name	method	Fe	Cr	Ni	T	SFE
2	exp	71.7291	17.2592	11.0117	300	18
3	exp	71.9295	16.0171	12.0534	300	22
4	exp	72.5882	12.9756	14.4362	300	33
5	exp	73.39	10.4267	16.1833	300	43

Table B.6: Fawley1968 [16]: Fe-Cr-Ni

name	method	Fe	Cr	Ni	C	N	T	SFE
1	exp	69.989	20	10	0.006	0.005	298.15	23 $\pm$ 4.025
2	exp	64.979	20	15	0.018	0.003	298.15	32 $\pm$ 5.6
3	exp	59.979	20	20	0.015	0.006	298.15	40 $\pm$ 7
4	exp	54.985	20	25	0.009	0.006	298.15	38 $\pm$ 6.65
5	exp	49.983	20	30	0.011	0.006	298.15	34 $\pm$ 5.95
6	exp	69.984	10	20	0.012	0.004	298.15	53 $\pm$ 9.275
7	exp	64.976	15	20	0.019	0.005	298.15	40 $\pm$ 7
8	exp	54.973	25	20	0.022	0.005	298.15	45 $\pm$ 7.875
9	exp	49.959	30	20	0.036	0.005	298.15	57 $\pm$ 9.975
10	exp	69.944	20	10	0.012	0.044	298.15	23 $\pm$ 4.025

Continued on next page

Table B.6 – continued from previous page

name	method	Fe	Cr	Ni	C	N	T	SFE
11	exp	64.955	20	15	0.01	0.035	298.15	34 $\pm$ 5.95
12	exp	59.931	20	20	0.018	0.051	298.15	38 $\pm$ 6.65
13	exp	54.958	20	25	0.009	0.033	298.15	38 $\pm$ 6.65
14	exp	49.961	20	30	0.01	0.029	298.15	34 $\pm$ 5.95
15	exp	69.975	10	20	0.012	0.013	298.15	48 $\pm$ 8.4
16	exp	64.977	15	20	0.012	0.011	298.15	44 $\pm$ 7.7
17	exp	54.936	25	20	0.017	0.047	298.15	47 $\pm$ 8.225
19	exp	59.97	20	20	0.027	0.003	298.15	43 $\pm$ 7.525
20	exp	49.94	20	30	0.05	0.01	298.15	47 $\pm$ 8.225

Table B.7: Gallagher1970 [17]: Fe-Cr-Ni

name	method	Fe	Cr	Ni	T	SFE
	exp	72.4	18	9.6	298.15	40.7
	exp	67.9	18	14.1	298.15	40.9
	exp	62.8	18	19.2	298.15	48.8

Table B.8: Guy1983 [18]: Fe-Cr-Ni

name	method	Fe	Cr	Ni	C	N	Si	P	S	Ti	V	Mn	Co	Mo	$A_s^{\alpha' \to \gamma}$	$A_f^{\alpha' \to \gamma}$
18/8	exp	72.524	18.03	7.94	0.039	0.011	0.2	0.01	0.006	0.1	0.04	1.08	0.01	0.01	813.15 $\pm$ 10	923.15 $\pm$ 10
18/12	exp	68.588	17.97	11.9	0.013	0.01	0.32	0.009	0.005	0.1	0.04	1.03	0.01	0.005	743.15 $\pm$ 10	883.15 $\pm$ 10

Table B.9: Knutsson2008 [19]: Fe-Cr-Ni

name	method	Fe	Cr	Ni	C	N	Si	Mn	Co	Cu	Nb	Mo	$A_s^{\alpha' \to \gamma}$	$A_f^{\alpha' \to \gamma}$
AISI 301	exp	72.215	17.55	7.67	0.095	0.022	0.55	1.23	0.1	0.25	0.008	0.31	723.15	873.15

Table B.10: Latanision1971 [20]: Fe-Cr-Ni

name	method	Fe	Cr	Ni	C	T	SFE
18.3Cr-10.7Ni	exp	70.995	18.3	10.7	0.005	298.15	18.2 $\pm$ 1
18.3Cr-10.7Ni	exp	70.995	18.3	10.7	0.005	408.15	27.6 $\pm$ 1.2
18.3Cr-10.7Ni	exp	70.995	18.3	10.7	0.005	598.15	30.4 $\pm$ 1.6
18.7Cr-15.9Ni	exp	65.395	18.7	15.9	0.005	298.15	24.9 $\pm$ 1
18.7Cr-15.9Ni	exp	65.395	18.7	15.9	0.005	408.15	28.8 $\pm$ 1.1
18.7Cr-15.9Ni	exp	65.395	18.7	15.9	0.005	598.15	31.8 $\pm$ 1.4

Table B.11: Lecroisey1970 [21]: Fe-Cr-Ni

name	method	Fe	Cr	Ni	C	M_s	T	SFE	M_d
1	exp	68.09	17.8	14.1	0.01	< 4.15	298.15	45	223.15
2	exp	71.59	15.9	12.5	0.01	< 178.15	298.15	24	273.15

Table B.12: Lecroisey1972 [22]: Fe-Cr-Ni

name	method	Fe	Cr	Ni	C	M_s	T	SFE	M_d
0-31	exp	69.18	—	30.8	0.02	248.15	—	—	278.15
0-31C	exp	69.06	—	30.8	0.14	228.15	—	—	273.15
0-25	exp	75	—	25	—	383.15	—	—	—
7-20	exp	73.296	6.7	20	0.004	$4.15 < x < 77.15$	—	—	> 298.15
7-19	exp	73.494	6.9	19.6	0.006	248.15	—	—	> 333.15
7-18C	exp	74.65	7.2	18	0.15	$77.15 < x < 183.15$	—	—	268.15
5-17C	exp	77.95	4.5	17.3	0.25	183.15	—	—	323.15
16-13	exp	71.59	15.9	12.5	0.01	178.15	298.15	22	353.15
16-11	exp	73.296	15.5	11.2	0.004	253.15	—	—	423.15
16-11B	exp	73.397	15.6	11	0.003	263.15	—	—	423.15
16-11C	exp	73	15.7	11.2	0.1	4.15	—	—	333.15
18-12	exp	70.192	17.8	12	0.008	208.15	298.15	30	323.15

Table B.13: Ledbetter1984 [23]: Fe-Cr-Ni

name	method	Fe	Cr	Ni	Mn	B_{fcc}
monocrystal	exp	71	19	10	—	160
polycrystal	exp	70.8	18.6	9.3	1.3	158.2

Table B.14: Li2000 [24]: Fe-Cr-Ni

name	method	Fe	Cr	Ni	C	M_s	$M_d^{\gamma\to\epsilon}$	$M_d^{\gamma\to\alpha'}$
	exp	74.82	18	7	0.18	356.15	420.15	360.15

Table B.15: Martinez1992 [25]: Fe-Cr-Ni

name	method	Fe	Cr	Ni	C	N	Al	Si	P	S	Mn	Cu	As	Nb	Mo	Sn	T	SFE
A	exp	69.2916	14.4	15.1	0.02	0.0084	0.005	0.59	0.006	0.013	0.53	0.02	0.002	0.002	0.01	0.002	298.15	45.5 $\pm$ 7.5
B	exp	68.7459	14.7	15.1	0.02	0.0081	0.005	0.48	0.006	0.012	0.43	0.04	0.001	0.44	0.01	0.002	298.15	27.5 $\pm$ 4.5
C	exp	68.7869	15.1	14.1	0.02	0.0071	0.005	0.53	0.006	0.012	0.52	0.01	0.002	0.89	0.01	0.001	298.15	23 $\pm$ 4
D	exp	67.7459	14.6	14.8	0.02	0.0081	0.005	0.57	0.006	0.012	0.47	0.01	0.002	1.74	0.01	0.001	298.15	21.5 $\pm$ 3.5

Table B.16: Ojima2009 [26]: Fe-Cr-Ni

name	method	Fe	Cr	Ni	C	N	Si	Mn	Mo	T	SFE
316L	exp	65.6457	17.35	12.95	0.015	0.0193	0.43	1.3	2.29	298.15	14.2
SUS310S	exp	53.899	25.1	19.8	0.048	0.023	0.33	0.8	—	298.15	30.9
SUS310S-N	exp	52.377	25	21.1	0.048	0.325	0.31	0.84	—	298.15	42.9
HNS	exp	69.731	23.09	4.16	0.019	1	—	—	2	298.15	22.3
10Cr-20Ni	exp	70.15	10	19.81	0.01	—	0.01	0.01	0.01	298.15	35.6
15Cr-10Ni	exp	75	14.98	9.98	0.01	—	0.01	0.01	0.01	298.15	15.2
15Cr-15Ni	exp	69.72	15.15	15.09	0.01	—	0.01	0.01	0.01	298.15	27.8
15Cr-20Ni	exp	65.05	15.06	19.85	0.01	—	0.01	0.01	0.01	298.15	31.4
15Cr-25Ni	exp	60.37	15.13	24.46	0.01	—	0.01	0.01	0.01	298.15	36.9
18Cr-12Ni	exp	70.65	18.13	11.18	0.01	—	0.01	0.01	0.01	298.15	19.3
20Cr-10Ni	exp	70.87	19.13	9.96	0.01	—	0.01	0.01	0.01	298.15	19.7
20Cr-15Ni	exp	64.81	20.06	15.09	0.01	—	0.01	0.01	0.01	298.15	21.8
20Cr-20Ni	exp	60.37	19.7	19.89	0.01	—	0.01	0.01	0.01	298.15	27.5
20Cr-25Ni	exp	55.45	20.09	24.42	0.01	—	0.01	0.01	0.01	298.15	36
25Cr-15Ni	exp	59.93	25.07	14.96	0.01	—	0.01	0.01	0.01	298.15	26
25Cr-19Ni	exp	56.62	24.56	18.78	0.01	—	0.01	0.01	0.01	298.15	28
25Cr-25Ni	exp	51.61	24.84	23.5	0.01	—	0.01	0.01	0.02	298.15	30.1

Table B.17: Olson1976 [27]: Fe-Cr-Ni

name	method	Fe	Cr	Ni	C	T	SFE
Fe16Cr13Ni	exp	71.59	15.9	12.5	0.01	158.6	13.7
Fe16Cr13Ni	exp	71.59	15.9	12.5	0.01	159.1	9.4
Fe16Cr13Ni	exp	71.59	15.9	12.5	0.01	166.2	9.6
Fe16Cr13Ni	exp	71.59	15.9	12.5	0.01	181.3	14.8
Fe16Cr13Ni	exp	71.59	15.9	12.5	0.01	183.6	10.8
Fe16Cr13Ni	exp	71.59	15.9	12.5	0.01	185.3	12.5
Fe16Cr13Ni	exp	71.59	15.9	12.5	0.01	215.9	18.3
Fe16Cr13Ni	exp	71.59	15.9	12.5	0.01	216.6	17.1
Fe16Cr13Ni	exp	71.59	15.9	12.5	0.01	225	18.2
Fe16Cr13Ni	exp	71.59	15.9	12.5	0.01	225.4	16.1
Fe16Cr13Ni	exp	71.59	15.9	12.5	0.01	264.9	20.3
Fe16Cr13Ni	exp	71.59	15.9	12.5	0.01	266	19.2
Fe16Cr13Ni	exp	71.59	15.9	12.5	0.01	266.2	20.8
Fe16Cr13Ni	exp	71.59	15.9	12.5	0.01	273.8	25.5
Fe16Cr13Ni	exp	71.59	15.9	12.5	0.01	297	19.6
Fe16Cr13Ni	exp	71.59	15.9	12.5	0.01	297.7	21.6
Fe16Cr13Ni	exp	71.59	15.9	12.5	0.01	297.9	20.7
Fe16Cr13Ni	exp	71.59	15.9	12.5	0.01	297.9	24.4

Continued on next page

Table B.17 – continued from previous page

name	method	Fe	Cr	Ni	C	T	SFE
Fe16Cr13Ni	exp	71.59	15.9	12.5	0.01	298	20.1
Fe16Cr13Ni	exp	71.59	15.9	12.5	0.01	298	26.1
Fe16Cr13Ni	exp	71.59	15.9	12.5	0.01	298.4	23.4
Fe16Cr13Ni	exp	71.59	15.9	12.5	0.01	329	31.1
Fe16Cr13Ni	exp	71.59	15.9	12.5	0.01	333.8	25
Fe16Cr13Ni	exp	71.59	15.9	12.5	0.01	334	24
Fe16Cr13Ni	exp	71.59	15.9	12.5	0.01	335.2	20.5
Fe16Cr13Ni	exp	71.59	15.9	12.5	0.01	373	25.2
Fe16Cr13Ni	exp	71.59	15.9	12.5	0.01	373.6	26.3
Fe18Cr12Ni	exp	70.192	17.8	12	0.008	94.3	10.8
Fe18Cr12Ni	exp	70.192	17.8	12	0.008	94.3	11.9
Fe18Cr12Ni	exp	70.192	17.8	12	0.008	181.3	16.1
Fe18Cr12Ni	exp	70.192	17.8	12	0.008	182.5	17.3
Fe18Cr12Ni	exp	70.192	17.8	12	0.008	220.5	20.6
Fe18Cr12Ni	exp	70.192	17.8	12	0.008	223.1	18.8
Fe18Cr12Ni	exp	70.192	17.8	12	0.008	235.2	23.4
Fe18Cr12Ni	exp	70.192	17.8	12	0.008	236.5	17.4
Fe18Cr12Ni	exp	70.192	17.8	12	0.008	275.1	20.5

Continued on next page

Table B.17 – continued from previous page

name	method	Fe	Cr	Ni	C	T	SFE
Fe18Cr12Ni	exp	70.192	17.8	12	0.008	275.3	25.3
Fe18Cr12Ni	exp	70.192	17.8	12	0.008	291.1	28.9
Fe18Cr12Ni	exp	70.192	17.8	12	0.008	291.1	30
Fe18Cr12Ni	exp	70.192	17.8	12	0.008	291.2	28.2
Fe18Cr12Ni	exp	70.192	17.8	12	0.008	292.4	19.5
Fe18Cr12Ni	exp	70.192	17.8	12	0.008	292.9	22.8
Fe18Cr12Ni	exp	70.192	17.8	12	0.008	293	24.5
Fe18Cr12Ni	exp	70.192	17.8	12	0.008	333.6	28.1
Fe18Cr12Ni	exp	70.192	17.8	12	0.008	334.2	33.2
Fe18Cr14Ni	exp	68	18	14	—	107.9	23.3
Fe18Cr14Ni	exp	68	18	14	—	118.6	23.3
Fe18Cr14Ni	exp	68	18	14	—	152.9	25.7
Fe18Cr14Ni	exp	68	18	14	—	157.7	27.8
Fe18Cr14Ni	exp	68	18	14	—	157.7	28.8
Fe18Cr14Ni	exp	68	18	14	—	184.2	26
Fe18Cr14Ni	exp	68	18	14	—	184.2	26.8
Fe18Cr14Ni	exp	68	18	14	—	216.1	29.7
Fe18Cr14Ni	exp	68	18	14	—	216.8	28.5

Continued on next page

Table B.17 – continued from previous page

name	method	Fe	Cr	Ni	C	T	SFE
Fe18Cr14Ni	exp	68	18	14	—	241.3	32.3
Fe18Cr14Ni	exp	68	18	14	—	261.2	35
Fe18Cr14Ni	exp	68	18	14	—	298.5	35.2
Fe18Cr14Ni	exp	68	18	14	—	298.7	42.1
Fe18Cr14Ni	exp	68	18	14	—	299.2	34

Table B.18: Petrov1985 [28]: Fe-Cr-Ni

name	method	Fe	Cr	Ni	T	SFE
	exp	72.5298	16.8828	10.5874	298.15	16
	exp	67.3201	16.8395	15.8404	298.15	28
	exp	62.137	16.7965	21.0666	298.15	35
	exp	75.3949	14.0397	10.5654	298.15	16
	exp	70.6132	18.7847	10.6021	298.15	20
	exp	65.7981	23.5628	10.6391	298.15	25
	exp	69.7691	9.28008	20.9508	298.15	60
	exp	65.0089	13.9681	21.023	298.15	40
	exp	60.2158	18.6885	21.0957	298.15	35
	exp	55.3893	23.4417	21.1689	298.15	45

Table B.19: Petrov1985 [28]: Fe-Mn

name	method	Fe	Mn	T	SFE
	exp	85.2076	14.7924	298.15	25
	exp	80.2607	19.7393	298.15	28
	exp	75.3058	24.6942	298.15	27
	exp	70.3427	29.6573	298.15	42

Table B.20: Petrov1993 [6]: Fe-Mn

name	method	Fe	Mn	C	T	SFE
	exp	77.78	22	0.22	298.15	32.4
	exp	77.17	22	0.83	298.15	22.6
	exp	76.28	22	1.72	298.15	32.8
	exp	74.79	22	3.21	298.15	33.6

Table B.21: Petrov2003 [29]: Fe-Cr-Mn

name	method	Fe	Cr	Mn	N	T	SFE
Fe-15Cr-17Mn	exp	67.94	15	17	0.06	298.15	24 $\pm$ 1.2
Fe-15Cr-17Mn-0.2N	exp	67.77	15	17	0.23	298.15	25.1 $\pm$ 1.2
Fe-15Cr-17Mn-0.5N	exp	67.52	15	17	0.48	298.15	21.1 $\pm$ 1.1
Fe-15Cr-17Mn-0.9N	exp	67.11	15	17	0.89	298.15	41.6 $\pm$ 2

Table B.22: Petrov2003 [29]: Fe-Cr-Ni

name	method	Fe	Cr	Ni	C	N	Mn	T	SFE
Fe-18Cr-10Ni	exp	70.4	17.8	10.6	—	—	1.2	298.15	25 $\pm$ 1.2
Fe-18Cr-10Ni-0.05C	exp	70.64	17.9	10.5	0.06	—	0.9	298.15	30 $\pm$ 1.4
Fe-18Cr-10Ni-0.1C	exp	71.11	18.1	10.1	0.09	—	0.6	298.15	34 $\pm$ 1.5
Fe-18Cr-10Ni-0.15C	exp	70.69	18.1	10.6	0.11	—	0.5	298.15	39 $\pm$ 1.8
Fe-18Cr-16Ni-10Mn	exp	55.79	18.5	16.1	—	0.01	9.6	298.15	44 $\pm$ 2
Fe-18Cr-16Ni-10Mn-0.1N	exp	55.73	18.5	16.1	—	0.07	9.6	298.15	47 $\pm$ 2.3
Fe-18Cr-16Ni-10Mn-0.2N	exp	55.59	18.5	16.1	—	0.21	9.6	298.15	55 $\pm$ 2.7
Fe-18Cr-16Ni-10Mn-0.3N	exp	55.49	18.5	16.1	—	0.31	9.6	298.15	62 $\pm$ 3
Fe-18Cr-16Ni-10Mn-0.4N	exp	55.4	18.5	16.1	—	0.4	9.6	298.15	65 $\pm$ 3.2
Fe-18Cr-16Ni-10Mn-0.5N	exp	55.26	18.5	16.1	—	0.54	9.6	298.15	53 $\pm$ 2.6

Table B.23: Petrov2003 [29]: Fe-Mn

name	method	Fe	Mn	C	T	SFE
Fe-22Mn	exp	77.97	22	0.03	298.15	29 $\pm$ 1.4
Fe-22Mn-0.1C	exp	77.87	22	0.13	298.15	23 $\pm$ 1.2
Fe-22Mn-0.3C	exp	77.67	22	0.33	298.15	26 $\pm$ 1.3
Fe-22Mn-0.7C	exp	77.31	22	0.69	298.15	29 $\pm$ 1.5

Table B.24: Shin2001 [30]: Fe-Cr-Ni

name	method	Fe	Cr	Ni	C	N	Si	P	S	Mn	Mo	M_d
304	exp	71.524	18.07	8.5	0.05	0.037	0.56	0.025	0.004	1.05	0.18	322

Table B.25: Silcock1966 [31]: Fe-Cr-Ni

name	method	Fe	Cr	Ni	C	N	O	Si	P	S	Mn	Co	T	SFE
A1	exp	68.674	15.3	15.9	0.02	—	0.03	—	0.004	0.012	0.06	—	298.15	23 $\pm$ 4.6
A2	exp	55.103	15.8	23	0.007	6	0.03	—	0.01	0.01	0.04	—	298.15	28 $\pm$ 5.6

Continued on next page

Table B.25 – continued from previous page

name	method	Fe	Cr	Ni	C	N	O	Si	P	S	Mn	Co	T	SFE
A10	exp	42.39	15.3	15	0.006	7	0.04	—	0.01	0.014	0.04	20.2	298.15	12 $\pm$ 2.4
A55	exp	64.228	15.9	15.8	0.017	4	0.01	0.04	0.002	0.002	0.001	—	298.15	21 $\pm$ 4.2
A57	exp	52.857	15.4	24.7	0.011	7	0.01	0.015	0.002	0.002	0.003	—	298.15	30.5 $\pm$ 6.1
A71	exp	65.272	15.5	15.8	0.004	2	0.013	1.4	0.008	0.003	—	—	298.15	11 $\pm$ 2.2
A203	exp	64.35	16	10.1	—	—	—	—	—	—	—	9.55	298.15	8 $\pm$ 1.6

Table B.26: Singh1985 [32]: Fe-Cr-Ni

name	method	Fe	Cr	Ni	C	Si	$A_s^{\alpha' \to \gamma}$	$A_s^{\epsilon \to \gamma}$
304	exp	68.63	18.8	11.5	0.07	1	673	473

Table B.27: Swann1963 [33]: Fe-Cr-Ni

name	method	Fe	Cr	Ni	C	N	T	SFE
Tab1:line1	exp	74.4	17.6	7.9	0.06	0.04	298.15	7 $(+1.6/-1.7)$
Tab1:line2	exp	69.676	17.6	12.7	0.02	0.004	298.15	15.1 $(+1.8/-1.6)$
Tab1:line3	exp	64.366	17.8	17.8	0.03	0.004	298.15	19.1 $(+1.6/-1.1)$

Continued on next page

Table B.27 – continued from previous page

name	method	Fe	Cr	Ni	C	N	T	SFE
Tab1:line9	exp	74.83	17.9	7.1	0.06	0.11	298.15	5.9 $(+1.2/-1.2)$
Tab1:line10	exp	68.96	18.1	12.8	0.02	0.12	298.15	12.6 $(+1.8/-1.5)$

Table B.28: Tavares2000 [34]: Fe-Cr-Ni

name	method	Fe	Cr	Ni	C	Si	S	$A_s^{\alpha'\to\gamma}$	$A_50^{\alpha'\to\gamma}$	$A_f^{\alpha'\to\gamma}$
	exp	72.946	18.34	8.53	0.066	0.1	0.018	718.15 ± 5	838.15 ± 5	997.15 ± 5
	exp	72.946	18.34	8.53	0.066	0.1	0.018	713.15 ± 5	832.15 ± 5	978.15 ± 5
	exp	72.946	18.34	8.53	0.066	0.1	0.018	706.15 ± 5	822.15 ± 5	967.15 ± 5
	exp	72.946	18.34	8.53	0.066	0.1	0.018	708.15 ± 5	828.15 ± 5	969.15 ± 5
	exp	72.946	18.34	8.53	0.066	0.1	0.018	706.15 ± 5	846.15 ± 5	983.15 ± 5

References

[1] T. B. Massalski, Hugh Baker, L. H. Bennett, and Joanne L. Murray. *Binary Alloy Phase Diagrams*, **2**. American Society for Metals (ASM International), 1 edition, 1986. ISBN-13: 9780871702616, ISBN-10: 0871702614. xii, xiii, 19, 24

[2] Herman W. Pollack. *Materials Science and Metallurgy (4th Edition)*. Prentice Hall, 4 edition, January 1988. ISBN-10: 0835942872, ISBN-13: 978-0835942874. xii, 19

[3] Michael F. McGuire. *Stainless Steels for Design Engineers*. ASM International, December 2008. ISBN-13: 978-0-87170-717-8, ISBN-10: 0-87170-717-9, SAN: 204-7586. xiii, 23, 24, 25, 27, 28

[4] R. E. Schramm and R. P. Reed. **Stacking fault energies of seven commercial austenitic stainless steels**. *Metall. Mater. Trans. A*, **6**(7):1345–1351, Jul 1975. xv, 39, 58, 59

[5] P. J. Brofman and G. S. Ansell. **On the Effect of Carbon on the Stacking Fault Energy of Austenitic Stainless Steels**. *Metall. Mater. Trans. A*, **9**(6):879–880, Jun 1978. xv, 39, 59

[6] Yu. N. Petrov. **On the carbon distribution at structural imperfections in manganese austenite**. *Scr. Metall. Mater.*, **29**(11):1471–1476, Dec 1993. xv, xxii, 40, 59, 137

[7] Afshin Abbasi, Alexey Dick, Tilmann Hickel, and Jörg Neugebauer. **First-principles investigation of the effect of carbon on the stacking fault energy of Fe–C alloys**. *Acta Mater.*, **59**(8):3041–3048, May 2011. xv, 40, 53, 55, 58, 59, 62

[8] L. Vitos, P. A. Korzhavyi, and B. Johansson. **Evidence of Large Magnetostructural Effects in Austenitic Stainless Steels**. *Phys. Rev. Lett.*, **96**(11):117210–117213, Mar 2006. xvi, 40, 61, 65, 91, 96

[9] R. P. Reed and R. E. Schramm. **Relationship between stacking-fault energy and x-ray measurements of stacking-fault probability and microstrain**. *J. Appl. Phys.*, **45**(11):4705–4711, November 1974. xxi, 14, 15

[10] D. Liberman, J. T. Waber, and Don T. Cromer. **Self-Consistent-Field Dirac-Slater Wave Functions for Atoms and Ions. I. Comparison with Previous Calculations**. *Phys. Rev.*, **137**(1A):A27–A34, January 1965. xxi, 69

[11] Francois Abrassart. **Stress-Induced $\gamma \rightarrow \alpha'$ Martensitic Transformation in Two Carbon Stainless Steels. Application to Trip Steels**. *Metall. Trans.*, **4**(9):2205–2216, September 1973. Print ISSN: 0360-2133 Online ISSN: 1543-1916 Publisher: Springer-Verlag. xxii, 74, 99, 122

[12] C. C. Bampton, I. P. Jones, and M. H. Loretto. **Stacking fault energy measurements in some austenitic stainless steels**. *Acta Metall.*, **26**(1):39–51, January 1978. xxii, 14, 124

[13] P. Behjati and A. Najafizadeh. **Role of Chemical Driving Force in Martensitic Transformations of High-Purity Fe-Cr-Ni Alloys**. *Metall. Mater. Trans. A*, **42**(12):3752–3760, December 2011. xxii, 74, 99, 125

[14] J. F. Breedis. **Martensitic Transformations in Iron-Chromium-Nickel Alloys**. *Transactions of the Metallurgical Society of AIME*, **230**:1583–1596, December 1964. xxii, 99, 126

[15] J. F. Breedis and L. Kaufman. **Formation of hcp and bcc Phases in Austenitic Iron Alloys**. *Metallurgical Transactions*, **2**(9):2359–2371, September 1971. xxii, 126

[16] R. Fawley, M. A. Quader, and R. A. Dodd. **Compositional Effects on Deformation Modes Annealing Twin Frequencies and Stacking Fault Energies of Austenitic Stainless Steels**. *Trans. TMS-AIME*, **242**(5):771–776, May 1968. ISSN: 0543-5722. xxii, 39, 127

[17] P. C. J. Gallagher. **The Influence of Alloying, Temperature, and Related Effects on the Stacking Fault Energy**. *Metallurgical Transactions*, **1**:2429–2461, September 1970. xxii, 128

[18] K. B. Guy, E. P. Butler, and D. R. F. West. **Reversion of bcc α' martensite in Fe–Cr–Ni austenitic stainless steels**. *Metal Science*, **17**(4):167–176, April 1983. xxii, 99, 129

[19] Axel Knutsson, Peter Hedström, and Magnus Odén. **Reverse martensitic transformation and resulting microstructure in a cold rolled metastable austenitic stainless steel**. *Steel Res. Int.*, **79**(6):433–439, 2008. ISSN: 1611-3683. xxii, 99, 129

[20] R. M. Latanision and A. W. Ruff. **The Temperature Dependence of Stacking Fault Energy in Fe-Cr-Ni Alloys**. *Metall. Trans.*, **2**:505–509, February 1971. xxii, 129

[21] F. Lecroisey and B. Thomas. **On the variation of the Intrinsic Stacking Fault Energy with Temperature in Fe-18 Cr-12 Ni Alloys**. *Phys. Stat. Sol. A*, **2**:K217–K220, 1970. xxii, 130

[22] F. Lecroisey and A. Pineau. . *Metall. Trans.*, **3**(2):391–400, February 1972. Print ISSN: 0360-2133, Online ISSN: 1543-1916, Publisher: Springer-Verlag. xxii, 130

[23] H. M. Ledbetter. **Monocrystal-Polycrystal Elastic Constants of a Stainless Steel**. *Phys. Stat. Sol. A*, **85**(1):89–96, 1984. xxii, 78, 131

[24] James Chen-Min Li, editor. *Microstructure and Properties of Materials*, **2**. World Scientific Pub Co Inc, September 2000. ISBN-10: 9810241801, ISBN-13: 978-9810241803. xxii, 131

[25] Luis G. Martinez, Kengo Imakuma, and Angelo F. Padilha. **Influence of niobium on stacking-fault energy of all-austenite stainless steels**. *Steel Res.*, **63**(5):221–223, May 1992. ISSN: 0177-4832. xxii, 131

[26] M. Ojima, Y. Adachi, Y. Tomota, Y. Katada, Y. Kaneko, K. Kuroda, and H. Saka. **Weak Beam TEM Study on Stacking Fault Energy of High Nitrogen Steels**. *Steel Res. Int.*, **80**(7):477–481, July 2009. xxii, 132

[27] G. B. Olson and Morris Cohen. **A general mechanism of martensitic nucleation: Part I. General concepts and the fcc→hcp transformation**. *Metall. Trans. A*, **7**(12):1897–1904, December 1976. Print ISSN: 0360-2133, Online ISSN: 1543-1940, Publisher: Springer-Verlag. xxii, 133

REFERENCES

[28] Yu. N. Petrov. **Effect of Alloying on the Stacking Fault Energy of Austenite in Steel**. *Phys. Met.*, **6**(4):735–741, 1985. ISSN: 0275-9144. xxii, 136, 137

[29] Yu. N. Petrov. **Effect of carbon and nitrogen on the stacking fault energy of high-alloyed iron-based austenite**. *Z. Metallkd.*, **94**(9):1012–1016, September 2003. ISSN: 0044-3093. xxii, 138, 139

[30] Hong Chul Shin, Tae Kwon Ha, and Young Won Chang. **Kinetics of deformation induced martensitic transformation in a 304 stainless steel**. *Scr. Mater.*, **45**(7):823–829, October 2001. xxii, 98, 139

[31] J. M. Silcock, R. W. Rookes, and J. Barford. **Twin frequency and stacking fault energy in austenite steels**. *J. Iron Steel Inst.*, **204**:623–627, 1966. xxii, 139

[32] Jogender Singh. **Influence of deformation on the transformation of austenitic stainless steels**. *J. Mater. Sci.*, **20**(9):3157–3166, September 1985. Print ISSN: 0022-2461 Online ISSN: 1573-4803 Publisher: Kluwer Academic Publishers. xxii, 99, 140

[33] P. R. Swann. **Dislocation Substructure vs Transgranular Stress Corrosion Susceptibility Of Single Phase Alloys**. *Corrosion*, **19**:102t–112t, March 1963. xxii, 140

[34] S. S. M. Tavares, D. Fruchart, and S. Miraglia. **A magnetic study of the reversion of martensite α' in a 304 stainless steel**. *J. Alloys Compd.*, **307**(1–2):311–317, July 2000. xxii, 99, 141

[35] John Price Hirth and Jens Lothe. *Theory of Dislocations*. John Wiley & Sons, 2 edition, 1982. ISBN: 0-471-09125-1. 10, 11, 53

[36] Georg Frommeyer, Udo Brüx, and Peter Neumann. **Supra-Ductile and High-Strength Manganese-TRIP/TWIP Steels for High Energy Absorption Purposes**. *ISIJ Int.*, **43**(3):438–446, May 2003. 14, 61

[37] O. Grässel, L. Krüger, G. Frommeyer, and L. W. Meyer. **High strength Fe–Mn–(Al, Si) TRIP/TWIP steels development—properties—application**. *Int. J. Plast.*, **16**(10–11):1391–1409, 2000. 14, 61

[38] S. Allain, J. P. Chateaua, O. Bouazizb, S. Migota, and N. Guelton. **Correlations between the calculated stacking fault energy and the plasticity mechanisms in Fe–Mn–C alloys**. *Mater. Sci. Eng., A*, **387-389**:158–162, Dec 2004. 14, 61

[39] **Classification of Carbon and Low-Alloy Steels**. [http://www.keytometals.com/Articles/Art63.htm] KEY to METALS: The World's Most Comprehensive METALS Database. 17, 18

[40] Peter R. Knowles. *Design of Structural Steelwork*. Taylor & Francis Group, 2 edition, 2005. ISBN (Adobe eReader Format): 0-203-26795-8, ISBN (Print Edition):0-903384-59-0. 18

[41] D. H. Jack and K. H. Jack. **Invited review: Carbides and nitrides in steel**. *Mater. Sci. Eng.*, **11**(1):1–27, January 1973. 20

[42] D. E. Jiang and Emily A. Carter. **Carbon dissolution and diffusion in ferrite and austenite from first principles**. *Phys. Rev. B*, **67**(21):214103–214113, Jun 2003. 20, 23, 39, 40

[43] webelements. *http : //www.webelements.com/*. [link]. 20

[44] William D. Callister. *Materials science and engineering : an introduction*. John Wiley & Sons, Inc., 7 edition, 2007. ISBN-13: 978-0-471-73696-7, ISBN-10: 0-471-73696-1. 20, 22

[45] I. G. Wood, L. Vocadlo, K. S. Knight, D.P. Dobson, W. G. Marshall, G. D. Pricea, and J. Brodholta. **Thermal expansion and crystal structure of cementite, Fe3C, between 4 and 600 K determined by time-of-flight neutron powder diffraction**. *J. Appl. Cryst.*, **37**:82, 2003. 22

[46] A. K. Arzhnikov, L. V. Dobysheva, and C. Demangeat. **Structural peculiarities of cementite and their influence on magnetic characteristics**. *J. Phys.: Condens. Matter*, **19**(19):196214–196222, April 2007. 22, 57

[47] B. D. Butler and J. B. Cohen. **The location of interstitial carbon in austenite**. *J. Phys. I*, **2**(6):1059–1065, June 1992. 23, 39

[48] V. Rosato. **Comparative behavior of carbon in b.c.c. and f.c.c. iron**. *Acta Metall.*, **37**(10):2759–2763, Oct 1989. 23, 39

[49] Pierre-Jean Cunat. *Alloying Elements in Stainless Steel and Other Chromium-Containing Alloys*. International Chromium Development Association, ICDA, 45 Rue de Lisbonne, F-75008 Paris, 2004. 23

[50] Peter Puschnig. *Excitonic Effects in Organic Semi-Conductors - An Ab-initio Study within the LAPW Method*. PhD thesis, Karl-Frazens-Universität Graz, January 2002. 29

[51] Oleg E. Peil. *Theory of Disordered Magnets*. PhD thesis, Uppsala University, 2009. ISSN: 1651-6214, ISBN:978-91-554-7391-4. 29, 36

[52] Tetyana Khmelevska. *Influence of magnetic and chemical disorder on physical properties of metallic alloys*. PhD thesis, Vienna University of Technology, February 2009. 29, 36, 37

[53] Philip Peter Rushton. *Towards a Non-Local Density Functional Description of Exchange and Correlation*. PhD thesis, University of Durham, November 2002. 29

[54] Erwin Schrödinger. **DUUTSCH: Quantisierung als Eigenwertproblem (Erste Mitteilung) / ENGLISH: Quantisation as a Problem of Proper Values (Part I)**. *Ann. Physik*, **79**:361–376, 1926. 29

[55] Erwin Schrödinger. **DUUTSCH: Quantisierung als Eigenwertproblem (Zweite Mitteilung) / ENGLISH: Quantisation as a Problem of Proper Values (Part II)**. *Ann. Physik*, **79**:489–527, 1926. 29

[56] M. Born and J. R. Oppenheimer. **DEUTSCH: Zur Quantentheorie der Molekeln / ENGLISH: On the Quantum Theory of Molecules**. *Ann. Physik*, **84**:457, 1927. 30

[57] Douglas Rayner Hartree. **The Wave Mechanics of an Atom with a Non-Coulomb Central Field. Part I. Theory and Methods**. *Math. Proc. Cambridge Philos. Soc.*, **24**(1):89–110, January 1928. 30

[58] Douglas Rayner Hartree. **The Wave Mechanics of an Atom with a Non-Coulomb Central Field. Part II. Some Results and Discussion**. *Math. Proc. Cambridge Philos. Soc.*, **24**(1):111–132, January 1928. 30

[59] Wolfgang Pauli. **DEUTSCH: Über den Zusammenhang des Abschlusses der Elektronengruppen im Atom mit der Komplexstruktur der Spektren / ENGLISH: On the connection of the arrangement of electron groups in atoms with the complex structure of spectra**. *Z. Phys.*, **31**(1):765–783, April 1925. Print ISSN: 0044-3328; Publisher: Springer-Verlag. 30

[60] Enrico Fermi. **ITALIAN: Sulla quantizzazione del gas perfetto monoatomico / ENGLISH: On the Quantization of the Monoatomic Ideal Gas**. *Rend. Lincei*, **3**:145–149, 1926. 30

[61] John C. Slater. **The Theory of Complex Spectra**. *Phys. Rev.*, **34**(10):1293–1322, November 1929. 30

[62] Vladimir Fock. **DEUTSCH: Näherungsmethode zur Lösung des quantenmechanischen Mehrkörperproblems / ENGLISH: Approximation method for the solution of the quantum mechanical multibody problems**. *Z. Phys.*, **61**(1–2):126–148, January 1930. Print ISSN: 0044-3328, Publisher: Springer-Verlag. 31

[63] L. H. Thomas. **The calculation of atomic fields**. *Math. Proc. Cambridge Philos. Soc.*, **23**(5):542–548, January 1927. 31

[64] Enrico Fermi. **A statistical method for the determination of some properties of atoms. II. Application to the periodic system of the elements**. *Z. Phys.*, **48**:73, 1928. 31

[65] P. Hohenberg and W. Kohn. **Inhomogeneous Electron Gas**. *Phys. Rev.*, **136**(3B):B864–B871, November 1964. 31, 40

[66] Richard M. Martin. *Electronic Structure: Basic Theory and Practical Methods*. Cambridge University Press, April 2004. ISBN-10: 0521782856, ISBN-13: 978-0521782852. 31, 33, 66

[67] W. Kohn and L. J. Sham. **Quantum Density Oscillations in an Inhomogeneous Electron Gas**. *Phys. Rev.*, **137**(6A):A1697–A1705, Mar 1965. 31, 32

[68] Robert G. Parr and Weitao Yang. *Density-Functional Theory of Atoms and Molecules*. Oxford University Press, Oxford, April 1989. ISBN: 0-19-504279-4. 32

[69] James C. Phillips. **Energy-Band Interpolation Scheme Based on a Pseudopotential**. *Phys. Rev.*, **112**(3):685–695, November 1958. 33

[70] James C. Phillips and Leonard Kleinman. **Crystal Potential and Energy Bands of Semiconductors. IV. Exchange and Correlation**. *Phys. Rev.*, **128**(5):2098–2102, December 1962. 33

[71] Marvin L. Cohen and Volker Heine. **The Fitting of Pseudopotentials to Experimental Data and Their Subsequent Application**. *Solid State Physics*, **24**:37–248, 1970. 33

[72] J. C. Slater. **Wave Functions in a Periodic Potential**. *Phys. Rev.*, **51**(10):846–851, May 1937. 33

[73] Terry L. Loucks. *Augmented Plane Wave Method: a guide to performing electronic structure calculations*. W.A. Benjamin, January 1967. 33

[74] Georg K. H. Madsen, Peter Blaha, Karlheinz Schwarz, Elisabeth Sjöstedt, and Lars Nordström. **Efficient linearization of the augmented plane-wave method**. *Phys. Rev. B*, **64**(19):195134–195142, October 2001. 33, 34, 35

[75] O. Krogh Andersen. **Linear methods in band theory**. *Phys. Rev. B*, **12**(8):3060–3083, October 1975. 34

[76] D. D. Koelling and G. O. Arbman. **Use of energy derivative of the radial solution in an augmented plane wave method: application to copper**. *J. Phys. F: Met. Phys.*, **5**(11):2041, 1975. 34, 35

[77] David Singh. **Ground-state properties of lanthanum: Treatment of extended-core states**. *Phys. Rev. B*, **43**(8):6388–6392, March 1991. 35

[78] E. Sjöstedt, L. Nordström, and D. J. Singh. **An alternative way of linearizing the augmented plane-wave method**. *Solid State Commun.*, **114**(1):15–20, March 2000. 35

[79] P. Blaha, K. Schwarz, G. Madsen, D. Kvasnicka, and J. Luitz. **WIEN2k**. http://www.wien2k.at. 35, 36

[80] K. Schwarz, P Blaha, and G. K. H. Madsen. **Electronic structure calculations of solids using the WIEN2k package for material sciences**. *Comput. Phys. Commun.*, **147**(1–2):71–76, August 2002. 36

[81] W. Kohn and N. Rostoker. **Solution of the Schrödinger Equation in Periodic Lattices with an Application to Metallic Lithium**. *Phys. Rev.*, **94**(5):1111–1120, June 1954. 36

[82] J. Korringa. **On the calculation of the energy of a Bloch wave in a metal**. *Physica*, **13**(6–7):392–400, August 1947. 36

[83] Jan Zabloudil, Robert Hammerling, László Szunyogh, and Peter Weinberger. *Electron Scattering in Solid Matter: A Theoretical and Computational Treatise (Springer Series in Solid-State Sciences)*. Springer, 2005 edition, November 2004. ISBN-10: 3540225242, ISBN-13: 978-3540225249. 36

[84] A. Gonis. **Multiple-scattering theory for clusters of nonoverlapping potentials of arbitrary shape**. *Phys. Rev. B*, **33**(8):5914–5916, April 1986. 37

[85] A. R. Williams and J. van W Morgan. **Multiple scattering by non-muffin-tin potentials**. *J. Phys. C: Solid State Phys.*, **5**(22):L293–L298, 1972. 37

[86] A. R. Williams and J. van W Morgan. **Multiple scattering by non-muffin-tin potentials: general formulation**. *J. Phys. C: Solid State Phys.*, **7**(1):37–60, 1974. 37

[87] R. Zeller. **Multiple-scattering solution of Schrodinger's equation for potentials of general shape**. *J. Phys. C: Solid State Phys.*, **20**(16):2347–2360, 1987. 37

[88] Levente Vitos. *Computational Quantum Mechanics for Materials Engineers: The EMTO Method and Applications*. Springer, 1 edition, August 2007. ISBN-10: 1846289505, ISBN-13: 978-1846289507. 37

[89] S.-H. Wei, L. G. Ferreira, James E. Bernard, and Alex Zunger. **Electronic properties of random alloys: Special quasirandom structures**. *Phys. Rev. B*, **42**(15):9622–9649, November 1990. 37

[90] Alex Zunger, S.-H. Wei, L. G. Ferreira, and James E. Bernard. **Special quasirandom structures**. *Phys. Rev. Lett.*, **65**(3):353–356, July 1990. 37

[91] Paul Soven. **Coherent-Potential Model of Substitutional Disordered Alloys**. *Phys. Rev.*, **156**(3):809–813, April 1967. 37

[92] D. W. Taylor. **Vibrational Properties of Imperfect Crystals with Large Defect Concentrations**. *Phys. Rev.*, **156**(3):1017–1029, April 1967. 37

[93] B. L. Gyorffy. **Coherent-Potential Approximation for a Nonoverlapping-Muffin-Tin-Potential Model of Random Substitutional Alloys**. *Phys. Rev. B*, **5**(6):2382–2384, March 1972. 37, 62

[94] B. L. Gyorffy, A. J. Pindor, J. Staunton, G. M. Stocks, and H. Winter. **A first-principles theory of ferromagnetic phase transitions in metals**. *J. Phys. F: Met. Phys.*, **15**(6):1337–1386, 1985. 37, 62

[95] S. Kibey, J. B. Liu, M. J. Curtis, D. D. Johnson, and H. Sehitoglu. **Effect of nitrogen on generalized stacking fault energy and stacking fault widths in high nitrogen steels**. *Acta Mater.*, **54**(11):2991–3001, Jun 2006. 40, 62

REFERENCES

[96] W. Kohn and L. J. Sham. **Self-Consistent Equations Including Exchange and Correlation Effects**. *Phys. Rev.*, **140**(4A):A1133–A1138, November 1965. 40

[97] P. Blaha, K. Schwarz, G. K. H. Madsen, D. Kvasnicka, and J. Luitz. **WIEN2k, An Augmented Plane Wave + Local Orbital Program for Calculating Crystal Properties**. Technical report, Vienna University of Technology, Vienna, 2001. 40, 48

[98] C. Cheng, R. J. Needs, V. Heine, and N. Churcher. **Confirmation of an ANNNI-Like Model for Polytypism in SiC**. *Europhys. Lett.*, **3**(4):475–479, Feb 1987. 40, 62, 63

[99] P. J. H. Denteneer and W. van Haeringen. **Stacking-Fault Energies in Semiconductors from First-Principles Calculations**. *J. Phys. C: Solid State Phys.*, **20**(32):L883–L887, 1987. 40, 62, 63, 64

[100] R. B. McLellan and C. Ko. **The C–C interaction energy in iron-carbon solid solutions**. *Acta Metall.*, **35**(8):2151–2156, Aug 1987. 40

[101] Andrei Reyes-Huamantinco, Peter Puschnig, Claudia Ambrosch-Draxl, Oleg E. Peil, and Andrei V. Ruban. **Stacking-fault energy and anti-Invar effect in Fe-Mn alloy from first principles**. *Phys. Rev. B*, **86**(6):060201, Aug 2012. 40, 80, 81, 87, 97

[102] John P. Perdew, Kieron Burke, and Matthias Ernzerhof. **Generalized Gradient Approximation Made Simple**. *Phys. Rev. Lett.*, **77**(18):3865–3868, October 1996. 48, 82

[103] P. Entel, H. C. Herper, E. Hoffmann, G. Nepecks, E. F. Wassermann, M. Acet, V. Crisan, and H. Akai. **Understanding iron and its alloys from first principles**. *Philos. Mag. B*, **80**(2):141–153, 2000. 51

[104] L. Vitos, J.-O. Nilsson, and B. Johansson. **Alloying effects on the stacking fault energy in austenitic stainless steels from first-principles theory**. *Acta Mater.*, **54**(14):3821–3826, Aug 2006. 61

[105] L Vitos, P. A. Korzhavyi, J-O Nilsson, and B Johansson. **Stacking fault energy and magnetism in austenitic stainless steels**. *Phys. Scr.*, **77**(6):065703–065705, June 2008. 61

[106] A. V. Ruban and H. L. Skriver. **Calculated surface segregation in transition metal alloys**. *Comput. Mater. Sci.*, **15**(2):119–143, June 1999. 62

[107] I. A. Abrikosov, S. I. Simak, B. Johansson, A. V. Ruban, and H. L. Skriver. **Locally self-consistent Green's function approach to the electronic structure problem**. *Phys. Rev. B*, **56**(15):9319–9334, Octuber 1997. 62

[108] Hojjat Gholizadeh, Claudia Draxl, and Peter Puschnig. **The influence of interstitial carbon on the γ-surface in austenite**. *Acta Mater.*, **61**(1):341–349, January 2013. 62

[109] A. van de Walle and G Ceder. **The effect of lattice vibrations on substitutional alloy thermodynamics**. *Rev. Mod. Phys.*, **74**(1):11–45, January 2002. 65

[110] Wolfgang Pfeiler, editor. *Alloy Physics: A Comprehensive Reference*. WILEY-VCH Verlag GmbH & Co. KGaA, 1st edition, September 2007. Print ISBN: 978-3-527-31321-1, Online ISBN: 978-3-527-61419-6. 65

[111] Göran Grimvall. **Spin disorder in paramagnetic fcc iron**. *Phys. Rev. B*, **39**(16):12300, June 1989. 66

[112] N. David Mermin. **Thermal Properties of the Inhomogeneous Electron Gas**. *Phys. Rev.*, **137**(5):A1441–A1443, March 1965. 66

[113] U. von Barth and C. D. Gelatt. **Validity of the frozen-core approximation and pseudopotential theory for cohesive energy calculations**. *Phys. Rev. B*, **21**(6):2222–2228, March 1980. 70

[114] F. D. Murnaghan. **The Compressibility of Media under Extreme Pressures**. *Proc. Nat. Acad. Sci. U.S.A.*, **30**(9):244–247, September 1944. PMCID: PMC1078704. 74

[115] George Krauss. *STEELS: Processing, Structure, and Performance*. ASM International, ASM International, Materials Park, Ohio 44073-0002, www.asminternational.org, third, 2005 edition, August 2005. ISBN-10: 0871708175, ISBN-13: 978-0871708175. 74

[116] Pat L. Mangonon and Gareth Thomas. **The martensite phases in 304 stainless steel**. *Metall. Trans.*, **1**(6):1577–1586, June 1970. 74

[117] M. Humbert, B. Petit, B. Bolle, and N. Gey. **Analysis of the $\gamma - \epsilon - \alpha'$ variant selection induced by 10% plastic deformation in 304 stainless steel at -60 °C**. *Mater. Sci. Eng., A*, **454–455**:508–517, April 2007. 74

[118] Cyril Cayron, Françoise Barcelo, and Yann de Carlan. **The mechanisms of the fccbcc martensitic transformation revealed by pole figures**. *Acta Mater.*, **58**(4):1395–1402, February 2010. 74

[119] Cyril Cayron, Françoise Barcelo, and Yann de Carlan. **Reply to Comments on The mechanisms of the fcc–bcc martensitic transformation revealed by pole figures**. *Scr. Mater.*, **64**(1):103–106, January 2011. 74

[120] A. H. Eichelman and F. C. Hull. **The Effect of Composition on the Temperature of Spontaneous Transformation of Austenite to Martensite in 18-8 Type Stainless Steel**. *Trans. Am. Soc. Met.*, **45**:77–104, 1953. 74

[121] John D. Verhoeven. *Steel Metallurgy for the Non-Metallurgist*. ASM International, 2007. 75

[122] L. Delczeg, B. Johansson, and L. Vitos. ***Ab initio* description of monovacancies in paramagnetic austenitic Fe-Cr-Ni alloys**. *Phys. Rev. B*, **85**(17):174101–174107, May 2012. 75

[123] H. L. Zhang, N. Al-Zoubi, B. Johansson, and L. Vitos. **Alloying effects on the elastic parameters of ferromagnetic and paramagnetic Fe from first-principles theory**. *J. Appl. Phys.*, **110**(7):073707–073718, October 2011. 75

[124] M. Ekholm and I. A. Abrikosov. **Structural and magnetic ground-state properties of γ-FeMn alloys from *ab initio* calculations**. *Phys. Rev. B*, **84**(10):104423–104438, Sep 2011. 75

[125] Tôru Moriya. *Spin fluctuations in itinerant electron magnetism*. Springer-Verlag Berlin, 1985. ISBN: 3-540-15422-1, ISBN: 3-387-15422-1. 79

[126] A. V. Ruban, S. Khmelevskyi, P. Mohn, and B. Johansson. **Temperature-induced longitudinal spin fluctuations in Fe and Ni**. *Phys. Rev. B*, **75**(5):054402–054408, Feb 2007. 80, 87

[127] John P. Perdew and Yue Wang. **Accurate and simple analytic representation of the electron-gas correlation energy**. *Phys. Rev. B*, **45**(23):13244–13249, June 1992. 81

[128] A. V. Ruban, S. Shallcross, S. I. Simak, and H. L. Skriver. **Atomic and magnetic configurational energetics by the generalized perturbation method**. *Phys. Rev. B*, **70**(12):125115–125133, September 2004. 82

[129] S. Cottenier, B. De Vries, J. Meersschaut, and Rots. M. **What density-functional theory can tell us about the spin-density wave in Cr**. *J. Phys.: Condens. Matter*, **14**(12):3275–3283, March 2002. 82

[130] V. M. Adeev and Yu. N. Petrov. **Influence of carbon on the stacking fault energy of austenite in plain carbon steel**. *Ukrayins'kyi Fizychnyi Zhurnal*, **20**(12):2004–2007, December 1975. 89

Declaration